




Universitat Autònoma de Barcelona

ADVERTIMENT. L'accés als continguts d'aquesta tesi queda condicionat a l'acceptació de les condicions d'ús establertes per la següent llicència Creative Commons:  http://cat.creativecommons.org/?page_id=184

ADVERTENCIA. El acceso a los contenidos de esta tesis queda condicionado a la aceptación de las condiciones de uso establecidas por la siguiente licencia Creative Commons:  <http://es.creativecommons.org/blog/licencias/>

WARNING. The access to the contents of this doctoral thesis it is limited to the acceptance of the use conditions set by the following Creative Commons license:  <https://creativecommons.org/licenses/?lang=en>

UNIVERSITAT AUTÒNOMA DE BARCELONA

Resistive Switching in Strontium Iridates

Author:
Víctor Fuentes
López-Doriga

Supervisors:
Dr. Lluís Balcells
Dr. Alberto Pomar

Tutor:
Prof. Jordi Sort

ACNM
Advanced Characterization
and Nanostructured Materials

MICMAB
INSTITUT DE CIÈNCIA DE MATERIALS DE BARCELONA
EXCELENCIA SEVERO OCHOA
CONSEJO SUPERIOR DE INVESTIGACIONES CIENTÍFICAS

UAB
Universitat Autònoma
de Barcelona

*A thesis submitted for the degree of
Doctor of Philosophy in Materials Science*

Advanced Characterization and Nanostructured Materials
Institut de Ciència de Materials de Barcelona

November 19, 2020

Abstract

The present thesis studies the Resistive Switching properties in Ruddlensen-Popper strontium iridates ($\text{Sr}_{n+1}\text{Ir}_n\text{O}_{3n+1}$) thin films, focusing on the effect of Metal-Insulator Transitions of these phases in the Resistive Switching features.

In order to achieve this purpose, the deposition of iridates by sputtering is studied. During the course of the research it was found that the sputtering technique, unlike the more studied PLD, presents a preferential growth for the perovskite member of the family (SrIrO_3) with deviations from the nominal stoichiometry. This growth is mainly controlled by kinetic processes with a large resputtering effect observed at high temperatures. A complete microstructural characterization has shown that the obtained films are flat, stable, homogeneous and possess a high level of crystallinity. Additionally, the conditions of deposition in these films were altered to tune the morphology of the film from flat to a nanostructured topography with holes that can be ordered according to the underlying substrate. For the sake of comparison, Sr_2IrO_4 films were grown by PLD.

After obtaining high quality films of the SrIrO_3 and Sr_2IrO_4 phases, their electrical properties are evaluated. While Sr_2IrO_4 films presented an insulating behavior, which reflects their Mott insulator nature, the thick perovskite SrIrO_3 films showed a semimetallic ground state. As the thickness of the SrIrO_3 film is reduced a Metal-Insulator Transition is triggered at low temperature. This regime, exhibiting negative magnetoresistance at low temperature, is in well agreement with the Weak localization mechanism in 2D indicating the disorder as the origin of the transition. Further lowering the thickness leads to an abrupt change of behavior to a fully insulating film that is accompanied by a significant increase of the negative magnetoresistance and a slight change in the balance between carriers as measured by Hall Effect. This behavior may be attributed to strong Anderson-like localization. The nanostructured films also presented the same transition but with a softer evolution of the properties.

Local electric measurements performed with Conductive Atomic Force Microscopy and Kelvin Probe Force Microscopy proved that both studied

phases possess robust bipolar Resistive Switching. Nevertheless, the electronic ground state of each film has a significant impact on the characteristics of this switching. While the thick semimetallic SrIrO_3 films showed a smooth transition between resistance states, the insulating thinnest films presented a clear threshold at 2 V. This more abrupt switching is also replicated by the insulating Sr_2IrO_4 film, which exhibited a 4.5 V threshold. A mechanism model based in the addition or subtraction of oxygen vacancies in the interface of the films is proposed to explain the observed results. The changes in the resistance state are attributed to shifts in the Fermi level of the materials. On one hand, the continuum of electronic states in the semimetallic films causes a soft switching. On the other hand, the presence of Anderson localized states or a Mott band gap create an energy barrier that forces the system into a more abrupt switching shaped by a threshold.

Resum

Aquesta Tesi estudia les propietats de Commutació Resistiva en capes primes de la sèrie de Ruddlensen-Popper d'Iridats d'Estronci ($\text{Sr}_{n+1}\text{Ir}_n\text{O}_{3n+1}$). En especial, s'estudien els efectes de les transicions metall-aïllant d'aquestes fases en les característiques de la commutació resistiva.

Amb l'objectiu d'assolir aquest propòsit, s'estudia la deposició d'iridats mitjançant polvorització catòdica. En el curs de la investigació s'estudia que la polvorització catòdica, a diferència de la deposició per polsos de làser, presenta un creixement preferencial a la perovskita SrIrO_3 amb desviacions de l'estequiometria nominal. Aquest creixement està controlat principalment per processos cinètics i posseeix un gran efecte de reemissió observada a altes temperatures. Una caracterització microestructural completa ens mostra que les capes obtingudes són planes, estables, homogènies i posseeixen un alt nivell de cristal·linitat. A més a més, s'ha examinat que les condicions de deposició d'aquestes capes poden ser alterades per ajustar la morfologia de les capes, des de topografies planes a nanoestructures amb forats, els quals poden ser ordenats d'acord amb el substrat. Amb l'objectiu de tenir un punt de comparació, capes de Sr_2IrO_4 són crescudes mitjançant deposició per polsos làser.

Després d'obtenir capes d'alta qualitat de les fases SrIrO_3 i Sr_2IrO_4 , les seves propietats elèctriques van ser avaluades. Per una banda, les capes de Sr_2IrO_4 presenten un comportament aïllant, el qual reflecteix la seva naturalesa d'aïllant de Mott, per l'altre, les capes gruixudes de SrIrO_3 mostren un estat base semimetàl·lic. Reduint el gruix en aquestes últimes, una transició Metall-Aïllant apareix a baixes temperatures. Aquest règim, el qual exhibeix magnetoresistència negativa a baixes temperatures, està en consonància amb el mecanisme de localització dèbil en 2 dimensions, indicant el desordre com l'origen de la transició. Una reducció a gruixos més baixos porta el sistema a un canvi abrupte cap a un comportament totalment aïllant acompanyat per un increment significatiu de la magnetoresistència negativa i un desplaçament lleu en el balanç de portadors, el qual és mesurat per efecte Hall. Aquest comportament pot ser atribuït a una localització forta d'Anderson. Les capes nanoestructurades també presenten

la mateixa transició però amb una evolució més suau de les seves propietats.

Les mesures elèctriques locals realitzades amb Microscòpia de Força Atòmica de Corrent i Microscòpia de Sonda Kelvin proven que ambdues fases posseeixen propietats robustes de commutació resistiva. Malgrat això, l'estat base electrònic de cada capa té un impacte en les característiques de la commutació. Mentre que les capes semimetàl·liques de SrIrO_3 van mostrar una transició suau entre estats de resistència, les capes ultraprimes aïllants van presentar un clar voltatge llindar de 2 V. Aquesta commutació més abrupta es replica també per les capes aïllants de Sr_2IrO_4 , que exhibeixen un llindar a 4,5 V. Es proposa un model basat en un mecanisme d'addició o subtracció de vacants d'oxigen en la superfície de les capes per explicar els resultats observats. Els canvis en l'estat de resistència són atribuïts a desplaçaments en el nivell de Fermi dels materials. Per una banda, la continuïtat d'estats electrònics en les capes semimetàl·liques causa una commutació suau. Per l'altre, la presència d'estats localitzats d'Anderson o una separació energètica de Mott crea una barrera energètica que força el sistema a una commutació més abrupta modelada per un voltatge llindar.

Acknowledgements

En primer lugar, me gustaría agradecer a los miembros del tribunal (Aitor Lopeandía, Mónica Burriel, Carmen Ocal, Sergi Valencia y José Santiso) por haber accedido a evaluar esta tesis.

Quiero dar también las gracias a Benjamín Martínez por haberme dado la oportunidad de hacer la tesis y toda ayuda prestada durante la misma, especialmente por colaboración en la elaboración de los artículos.

Me gustaría también tener unas palabras de agradecimiento a mis directores, Lluís Balcells y Alberto Pomar, por toda la ayuda prestada, desde explicaciones teóricas a ayuda práctica en el laboratorio, pasando por todas las horas dedicadas a revisar y discutir esta tesis. Al Lluís per la seva disponibilitat per baixar al sputtering a resoldre les múltiples incidències que anaven apareixent al llarg del centenar de deposicions fetes. També per la seva actitud positiva quan els experiments no rutllaven. A Alberto por ayudarme cuando lo he necesitado, teniendo siempre un rato para explicarme, con mucha paciencia, conceptos que no entendía una y otra vez.

Voldria agrair també a la resta del grup de recerca i col·laboradors la seva disponibilitat constant per discutir sobre els temes de la tesis i la seva ajuda en àrees específiques que tant ha afavorit a aquesta tesis. A Zorica por haber sido como una tercera directora participando constantemente en el proceso de corrección de la tesis. También por su inestimable ayuda en toda la parte referente al crecimiento y propiedades de transporte, sin olvidar la ayuda prestada durante las estancias en Belgrado. Al Felip per les mesures i l'anàlisi de les imatges de TEM i per la seva disponibilitat per resoldre els múltiples dubtes que m'han anat sorgint. Al Carlos per l'ajuda amb les interpretacions de les mesures de Raigs-X. A la Laura per ensenyar-me el funcionament del AFM i ajudar-me en tot el possible durant els primers anys de tesis en què tot és nou i estava més perdut.

A mis compañeros de trabajo, Sergi y Mónica, por todas las horas de comer pasadas juntos hablando y riéndonos de cualquier tema que me han permitido tener esos descansos tan necesarios durante los mediodías. También a los compañeros de despacho que he ido teniendo con los que siempre puedes compartir penas cuando las cosas no salen bien.

M'agradaria també fer un graïment a tots els tècnics (ja siguin del ICMAB, del ICN2 o del CCI TUB) que han ajudat a que aquesta tesis es

pogués realitzar, no només amb les mesures, sinó també contestant a totes les picades de porta i e-mails carregats de dubtes que han sabut resoldre.

Hvala Boris! For the constant help with the SPM techniques and the articles elaboration, but also for caring about my accommodation and the bus tickets during my stays in Belgrade.

También me gustaría agradecer a Carlos y al grupo de Chile por acogernos a mí y a Sergi en nuestra estancia, ayudándonos en todo lo posible mientras estuvimos allí.

En el pla personal, m'agradaria agrair a la Laia per fer-me oblidar de la tesis durant els passejos interminables per les fredes estepes manrussianes. També pel seu interminable somriure i les seves paraules d'ànims constants que m'han fet perseverar en la feina. También me gustaría agradecer a mi familia (mis padres y mi hermana) el constante apoyo, especialmente durante las épocas de confinamiento, que tan necesario ha sido para que siguiera escribiendo sin desfallecer.

Esta tesis se ha podido realizar gracias a la financiación del Ministerio de Ciencia, Innovación y Universidades a través de los proyectos Severo Ochoa (SEV-2015-04969) y MAT2015-71664-R. Las estancias en el extranjero realizadas durante el doctorado han sido financiadas por el programa Horizon 2020 de investigación e innovación de la Unión Europea bajo la beca Marie Skłodowska-Curie No. 645658 (DAFNEOX Project).

Contents

Abstract	iii
Resum	v
Acknowledgements	vii
1 Introduction	1
1.1 Motivation	1
1.2 Objectives	2
1.3 Outlook of the Thesis	2
2 Background	5
2.1 Resistive Switching	5
2.1.1 Resistive Switching in oxides	6
2.1.2 Technological applications	8
2.2 Metal Insulator Transitions	9
2.2.1 Mott Transition	10
2.2.2 Anderson Transition	10
2.2.3 Resistive Switching in Materials with Metal-Insulator Transitions	11
2.3 Strontium iridates	13
2.3.1 Perovskite SrIrO_3 ($n=\infty$)	16
2.3.2 Sr_2IrO_4 ($n=1$)	18
3 Iridates thin film growth	19
3.1 SrIrO_3 thin films growth	19
3.1.1 Target Fabrication	20
3.1.2 Influence of the thermodynamic deposition conditions	22
3.1.3 Stoichiometry Modulation	26
3.2 Microstructural Characterization of flat SrIrO_3 films	32
3.2.1 Topographic Characterization	32
3.2.2 Transmission Electron Microscopy	33
3.2.3 X-Ray Photoelectron Spectrometry	34

3.2.4	X-Ray Diffraction	37
3.2.5	Stability of the films	40
3.3	Kinetics driven surface nanostructures in SrIrO ₃ films	42
3.4	Deposition of Platinum Nanoparticles	48
3.5	Sr ₂ IrO ₄ thin film growth	50
4	Electric properties of Strontium Iridates	53
4.1	Transport properties of flat SrIrO ₃ films	53
4.1.1	Metal Insulator Transition in the SrIrO ₃ films	54
	Semimetallic region	58
	Insulating Region	61
4.1.2	Magnetotransport in SrIrO ₃ films	64
4.1.3	Hall Effect measurements	67
4.2	Transport properties of the nanostructured films	70
4.2.1	Metal-Insulator Transition in nanostructured films	70
	Semimetallic Region	73
	Insulating Region	74
4.2.2	Magnetotransport in nanostructured films	76
4.2.3	Conclusions of transport mechanisms for flat and nanostructured films	78
4.3	Transport properties of Sr ₂ IrO ₄ films	79
5	Resistive Switching in Strontium Iridates	81
5.1	Resistive Switching in SrIrO ₃ films	81
5.1.1	I-V curves in semimetallic flat SrIrO ₃ films	81
5.1.2	Resistive Switching in SrIrO ₃ films over large areas	84
5.2	Resistive Switching through Metal-Insulator Transition	88
5.2.1	Resistive Switching in films with different thickness	88
5.2.2	Resistive Switching in nanostructured films	90
5.3	Resistive Switching of Sr ₂ IrO ₄ films	91
5.3.1	I-V curves in Sr ₂ IrO ₄ films	92
5.3.2	Comparison with semimetallic and insulating SrIrO ₃ films	93
5.3.3	Resistive switching in Sr ₂ IrO ₄ over large areas	93
5.3.4	Resistive switching effect on the surface potential	95
5.4	Discussion on the Resistive Switching mechanisms	98
5.4.1	Filamentary vs Interfacial type	98
5.4.2	Mechanism of Switching in the n=∞ phase	99
5.4.3	Differences between the semimetallic and insulating SrIrO ₃ films	102
5.4.4	Mechanism of Switching in the n=1 phase	105

6	Conclusions	109
6.1	Further work	110
A	Experimental Techniques	113
A.1	Thin Film deposition techniques	113
A.1.1	Plasma Assisted Physical Vapor Deposition (Sputtering)	113
A.1.2	Pulsed Laser Deposition	116
A.2	X-Ray based Techniques	117
A.2.1	θ - 2θ Measurements	117
A.2.2	Reciprocal Space Mapping	118
A.2.3	Pole Figures	118
A.2.4	X-Ray Reflectometry	119
A.2.5	X-Ray Photoelectron Spectroscopy	121
A.3	Scanning Probe Microscopies	122
A.3.1	Intermittent contact mode (tapping)	125
A.3.2	Conductive Atomic Force Microscopy	126
A.3.3	Kelvin Probe Force Microscopy	128
A.4	Electron Based Techniques	130
A.4.1	Scanning Electron Microscopy	130
A.4.2	Electron probe microanalysis	130
A.4.3	Transmission Electron Microscopy	131
A.5	Lithography processes	132
A.5.1	Macroscopic masks	132
A.5.2	U-V lithography	132
A.6	Electric Measurements	134
A.6.1	Resistivity measurements	134
A.6.2	Magnetoresistance	135
A.6.3	Hall Effect Measurements	135
	Bibliography	137
	List of Publications	149

List of Abbreviations

AFM	Atomic Force Microscopy
C-AFM	Conductive-Atomic Force Microscopy
CPD	Contact Potential Difference
EPMA	Electron Probe Microanalysis
FFT	Fast Fourier Transform
FS	Feedback System
HRS	High Resistance State
I-V	Intensity-Voltage
KPFM	Kelvin Probe Force Microscopy
LAO	LaAlO ₃
LHB	Lower Hubbard Band
LRS	Low Resistance State
MIM	Metal-Insulator-Metal
MIT	Metal-Insulator Transition
MR	Magnetoresistance
n=∞	SrIrO ₃
n=1	Sr ₂ IrO ₄
n=2	Sr ₃ Ir ₂ O ₇
MIR	Mott-Ioffe-Regel
NGO	NdGaO ₃
NP	Nanoparticle
NS	Nanostructured
PLD	Pulsed Lased Deposition
PO₂	Oxygen Pressure
PPMS	Physical Properties Measurement System
PVD	Physical Vapor Deposition
RF	Radio Frequency
rms	Root Mean Square
RP	Ruddlesden-Popper
RS	Resistive Switching
RSM	Reciprocal Space Map
RT	Room Temperature
SEM	Scanning Electron Microscopy

SOC	Spin Orbit Coupling
SP	Set Point
SPM	Scanning Probe Microscopy
SQUID	Superconducting Quantum Interference Device
STO	SrTiO ₃
SV	Sample Voltage
TEM	Transmission Electron Microscopy
T_{MIT}	Temperature of the Metal-Insulator Transition
TMO	Transition Metal Oxide
U-V	Ultraviolet-Visible
UHB	Upper Hubbard Band
VCM	Valence Change Mechanism
VRH	Variable Range Hopping
V_{th}	Voltage threshold
XPS	X-Ray Photoelectron Spectroscopy
XRD	X-Ray Diffraction
XRR	X-Ray Reflectometry

Chapter 1

Introduction

1.1 Motivation

In the last 50 years information technologies have crossed the gap between research facilities to personal devices changing in many aspects everyone's lives. The utilities and usage of these technologies are in constant increase in well agreement with the increment of the processing capacity and the memory storage of the commercialized devices. This exponential increment in the computer's performance has been only possible due to the miniaturization of its basic components. Nevertheless, the traditional technologies are reaching relevant physical limits that are hindering their usual progress [1]. Moreover, the exponential increase in energy consumption produced by the miniaturization is also reaching unsustainable limits that must be addressed [2]. In order to keep reducing the size of the components and improve the energy efficiency of the devices new technologies are needed. In this context many new paradigms such as spintronics [3] or single molecule electronics [4] are currently under investigation to boost the industry in the short and mid terms.

One of the strongest candidates to substitute the traditional Random Access Memories (RAM) technologies, such as NAND or DRAM is the devices based on the Resistive Switching (RS) phenomena [5]. The materials possessing this type of properties are able to switch between different resistance states when certain voltages are applied, creating memories controlled by electric field [6]. Devices based in these principles have a large potential application (that will be explained in the next chapter) and, although they have already been commercialized [7], the basic research on this is still a hot topic nowadays with more than 1000 scientific articles per year according to Web of Science.

As in the case of the previous technologies, in the RS based devices there

is a constant pursuit for the performance improving which leads the research into new strategies. One of the variants that has dragged more attention in the past decade is the RS in materials with Metal-Insulator Transitions (MIT). The materials possessing such properties can transit from a metallic state to an insulating one (or viceversa) under the action of certain external stimulus. Therefore, specific changes induced by the application of voltage can trigger the transitions and enhance the switching properties, turning these materials in excellent candidates for RS applications [8] [9].

Among these materials one can found the Ruddlesden-Popper phases of the Strontium Iridates. These 5d Transition Metal Oxides have comparable contributions of electron correlation, crystal field and spin orbit coupling, which generate a band structure in these compounds that are close to several MITs [10]. The two extremes of the family are the perovskite-like SrIrO_3 and the Sr_2IrO_4 phases, being the former a correlated metal and the last a Mott Insulator. Nevertheless, in both cases it is well reported that small perturbations can reverse the phases into insulating or semimetallic states [11] [12]. Despite the interest for these phases has been increased in the last decade, their RS properties are still poorly studied.

1.2 Objectives

The main goal of the present thesis is to grow Strontium Iridates Ruddlesden-Popper thin films and to study their Resistive Switching phenomena. Moreover, the possible implications of the different Metal-Insulator Transitions in the Resistive Switching characteristics of the films will be also examined. In order to obtain and interpret precisely these results, high quality films of the different phases and states are necessary. Therefore, the growth conditions to obtain the films must be optimized and the resultant films have to be carefully characterized. Since the aim of this thesis is to use materials that possess Metal-Insulator Transitions, the electric properties of the film have also to be analyzed extensively. Once these two objectives are achieved, Resistive Switching phenomena will be studied by means of scanning probe microscopies.

1.3 Outlook of the Thesis

This work is thus divided in 1 introductory part and 3 parts of results and discussion, where the three aforementioned stages of the research will be exposed.

In the introductory chapter, named Background, the necessary general concepts to understand the thesis are briefly explained. This includes from the general types of RS, the different MITs present in this thesis and the iridate phases studied. Moreover, this part introduces the state of the art at the moment of the thesis of the studied topics.

The first part of the thesis results is dedicated to the study of the growth of the iridates thin films by sputtering and Pulsed Lased Deposition. In this part the conditions to obtain epitaxial flat SrIrO_3 films are explored by sputtering. The resultant films are characterized structural, stoichiometrical and morphologically with diverse techniques to ensure that they are suitable for the further studies. Moreover the conditions to obtain different nanostructured morphologies are examined. Additionally, Platinum Nanoparticles are grown on the top of the films and their disposition in both the flat and the patterned ones is analyzed. Finally, this chapter explains the growth and characterization of Sr_2IrO_4 films deposited by Pulsed Laser Deposition.

In the second part the electric properties of both the flat and the nanostructured films are analyzed. Moreover two series of SrIrO_3 films with different thicknesses are grown to study a MIT triggered by the reduction of thickness. The disorder driven nature of this transition is then studied by resistivity curves, magnetotransport and Hall Effect measurements. The resistivity curves of the Mott insulator Sr_2IrO_4 are also measured and analyzed.

Finally, in the third part of the results the resistive switching properties of the studied iridates are examined. These measurements are carried out in a Conductive Atomic Force Microscopy using I-V curves and current maps. Both the SrIrO_3 films above and below the MIT are evaluated in flat and nanostructured films. Additionally, films of the phase Sr_2IrO_4 are evaluated by the same procedures to compare their RS properties with the ones obtained for the SrIrO_3 phase. Once collected all the data, the mechanisms responsible for the results are discussed and the differences in the RS characteristics between the films are clarified.

At the end of the Thesis the Appendix A describes the experimental techniques employed in the three parts.

Chapter 2

Background

During the course of this thesis many concepts arise naturally from the focus of this particular research work or due to the explanation of the obtained results. This initial chapter pretends to introduce all these key concepts to understand the state of the art of the studied materials and phenomena at the time of the thesis. Moreover this chapter also intends to provide the reader from the basic knowledge regarding the topics being studied: from the most general aspects of the Resistive Switching phenomena to the specific materials used in this thesis.

2.1 Resistive Switching

Resistive Switching (RS) is defined as the reversible non-volatile change between two different resistance states in a given material due to the application of an external electric stimulus. In the most common case, a voltage pulse applied between two terminals can switch a material into a state with more resistivity, usually named the High Resistance State (HRS), or into a state of less resistivity, also known as the Low Resistance State (LRS). These states are named alternatively “OFF” (HRS) and “ON” (LRS) and the material can switch between them by the application of a voltage above a certain limit called Threshold Voltage (V_{th}). Due to the reversibility of the process one can “Set” a RS cell into a singular resistance state and “Reset” it to the other one by applying voltages above the V_{th} . Moreover, thanks to the non-volatile nature of this switching, the information of the current state can be read by applying voltages below the V_{th} and measuring the generated current. Therefore every single RS cell could be used as a memory for electrical devices with two possible states which provides the materials possessing these properties from an appealing technological potential [7].

Among the diversity of materials that exhibit RS behaviors we can found organic compounds [13], chalcogenides [14] or Transition Metal Oxides (TMOs) [15]. The RS research on this last group of materials has progressed

intensively since the middle of the 2000 decade [7] [16]. TMOs have become excellent candidates for RS applications due to their wide variability, their capability for acquiring defects and the presence of rich-physics scenarios [17].

2.1.1 Resistive Switching in oxides

The definition of RS encompasses a wide variety of phenomena with different mechanisms but comparable measurements and results. Due to this diversity, the RS phenomena can be classified according several systems in oxides. One of the most used ones is the operation mode of the switch that can be:

- Unipolar in the case that the voltages needed for switching the material into the HRS and the LRS have the same polarity (Figure 1.1 (a)).
- Bipolar in the case that the switching voltages have reverse polarities (Figure 1.1 (b)).

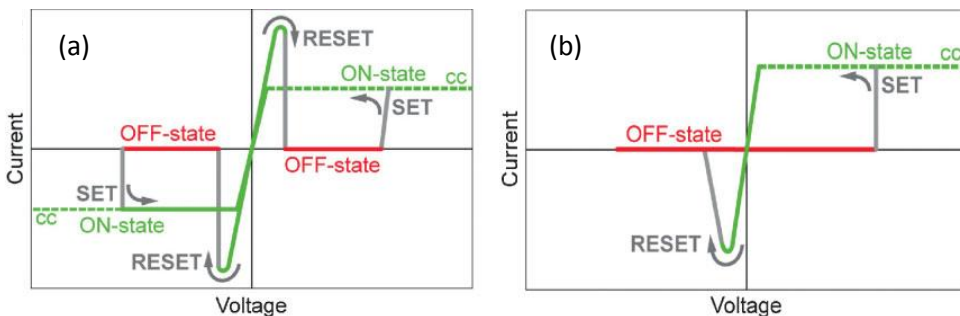


FIGURE 2.1: Characteristic Current vs Voltage RS curves depicting the different operation modes. (a) Unipolar (symmetric) RS where the processes of set and reset between the On and Off states can be performed in the same voltage polarity. (b) Bipolar RS where the Set and Reset processes are performed in the reverse polarity [6].

The RS behaviors can also be classified as a function of the part of the material switched. On one hand the interface switching takes place inside the vicinity of the switchable material with a terminal. On the other hand the filamentary RS can only appear in an insulating oxide where a conductive filament can grow, due to the voltage stimulus, between the two terminals in a Metal-Insulator-Metal (MIM) structure. The main measurable

difference between filamentary and interfacial RS relies on the area affected under the electric contact. While the intensity of the current increases with the section of the terminal in the case of the interface RS, it remains constant in the case of the filamentary RS since the current is only flowing through the filament independently of the area in contact [18].

Within each one of these major groups there are a range of mechanisms that induce the RS characteristics. Figure 2.2 provides a schematic sketch of the main mechanisms both for filamentary and interface-like RS. For example, in the case of the Thermochemical mechanism a controlled breakdown of the oxide (with a current compliance) forms a conductive filament that can be broken due to thermal diffusion obtained with enough current (Joule effect). Within the filamentary mechanisms one can also find the electrochemical metallization where the voltage pulses in a certain polarity induce the migration of metallic cations which form a LRS filament. Similarly to the Thermochemical one, the HRS can be obtained again by applying the reverse polarization and breaking the filament with thermal diffusion due to the Joule effect [7] [16].

Although they are not as technologically mature as their filamentary homologous, Interface-type RS has been observed in many systems with their own mechanisms. Among these mechanisms we can find electronic and electrostatic phenomena such as Schottky barriers, tunneling junctions or Metal Insulator Transitions (MIT) which can play a role in the switching as the primary source or assisting other mechanisms. This is the case of the ferroelectric polarization mechanism where a change in the polarity of a ferroelectric material can tune a Schottky barrier or a tunnel barrier [18].

There are also mechanisms that can belong to both the filamentary and the Interface-type RS as the case of the Valence Change Mechanism. In this mechanism the electric field can induce the creation of oxygen vacancies ($V_{\text{O}}^{\bullet\bullet}$) through a redox reaction or promote the migration of the existent ones in the switchable material. The presence of a vacancy in the nearby of a metallic cation can generate changes in its valence by the addition of electrons. The vacancies can be distributed in a column between the terminals forming an n-type doped oxide filament (filamentary RS) or homogeneously along the interface (interface RS) depending on the material [18].

It is worth noting that oxygen vacancies have the opposite effect in materials whose electric transport is dominated by electrons in comparison with materials that have holes as the major electric transport carrier. On one hand, in the electron-like materials the n-doping generated by the excess of vacancies increase the number of available carriers thus inducing the LRS. On the other hand, the extra electrons placed in the p materials cause the scavenging of the holes and thus inducing the HRS in the material [15].

Moreover, the addition or extraction of these extra electrons in the system can be the base for MITs or Schottky induced transitions [18].

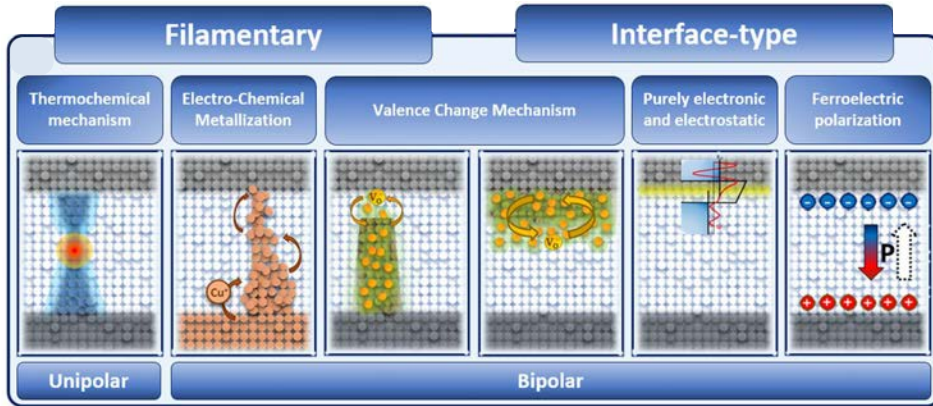


FIGURE 2.2: Sketch of the main mechanisms present in TMOs which can be classified in the two groups of Filamentary and Interface-type RS [18].

2.1.2 Technological applications

Memories based on the valence change mechanism (VCM) have been extensively investigated during the last two decades, especially those based on filamentary RS. The increment of interest shared both by industry and academia is the result of the great capabilities shown by this type of memories to replace the current Random Access Memories (RAM) technologies. Besides the intensive current basic research on the topic, RAM based on RS (ReRAM) have been commercialized since 2013 when Sandisk and Toshiba presented a 32 GB chip. Among the attractive characteristics of this type of memories one can find a good ratio between the resistance states (R_{HRS}/R_{LRS}) which typically ranges between 10 and 1000 ensuring an excellent sensing margin. Moreover the non destructive nature of the reading process, the fast writing speed (in the order of nanoseconds), their long endurance (10^6 - 10^8 cycles) and their compatibility with the extended CMOS allow these memory cells to compete with the current RAM technologies. Nevertheless, the key feature that is generating more interest is their good scalability that, due to the local character of the vacancies motion in the oxides, can reach areas smaller than $10 \times 10 \text{ nm}^2$, which clearly surpass the traditional technologies as DRAM, SRAM or NAND Flash. Moreover, unlike these technologies, which are reaching physical limits, the Redox based RS

cells are in constant improving and more recent studies have prove switching speeds of 85 ps, 10^{12} writing cycles and even dimensions of the cell up to 2 nm. Additionally to these main characteristics, desirables for any type of memories, some studies have shown that VCM could act in a multilevel operation process where more than two resistance states would be available. This would lead to an analog switching allowing the ReRAM memories to store more bits of information per cell [5] [7] [19].

Beyond of the usage of VCM as memories, these systems can be used for computational proposes. Among the possible applications in this field it should be pointed out the possible impact on the neuromorphic computation where the circuits are designed to emulate the biological neuron synapses. In living organisms the signals between connected neurons are called synapses and each of them has an intensity associated which "weights" the connection. While this is difficult to replicate from the point of view of the traditional computation technologies, it is more feasible in VCM cells due to the possibility to achieve the mentioned analog switching in multilevel devices [7] [19].

Nowadays, the commercialized ReRAMs are based on filamentary switching mechanisms in binary oxides that do not present any exotic properties. Nevertheless, the inclusion of materials that present additional phenomena such as MITs could lead RS cells to improve their performances [8] [18].

2.2 Metal Insulator Transitions

Currently most of the studied materials can be roughly classified into insulators and metals according to their resistivity dependence on the temperature. While metals have a dependence of $d\rho/dT > 0$ with temperature, insulators follow the inverse trend ($d\rho/dT < 0$) [20] [21].

In general these resistivity behaviors can be explained using quantum mechanics by the band theory. According to this theory if the highest occupied band is fully occupied and separated energetically (band gap) from the lowest unoccupied band, the material will be insulator. On the other hand, if the highest occupied band is only partially filled then the carriers could access to the conduction band and the material would behave as a metal [21].

Nevertheless some materials, mostly TMOs, cannot be fitted into these categories as they present an insulating behavior against the predictions of band theory. This disagreement is the product of considering the electrons individually and thus neglecting certain interactions such as disorder or

electron correlation. Moreover, variations in these interactions can lead the metal system into an insulating one, and vice versa, in what is known as Metal-Insulator Transitions (MITs) [20] [21].

Depending on the nature of the interactions that drive the change in the transport behavior several types of MITs can be distinguished. In the following subsections the ones with presence in this thesis are briefly explained.

2.2.1 Mott Transition

Mott transitions are based in the Coulomb repulsion between electrons (also known as electronic correlation). When a metal possesses a half filled band, an electron that wants to jump from an atom to another would experience a Coulomb electronic repulsion with the electron in the same state of the arrival atom. Then the conduction can be expressed as the capacity of the electrons to hop from one atom to its neighbors. Assuming this model, two factors influence the hopping events: the electronic repulsion between atoms represented by the Coulomb potential energy (U) and the distance of hopping which depends on the bandwidth of the atoms (W). Figure 2.3 (a) shows how if the quotient between U and W is increased from a metal without correlation ($U=0$) (1), the electron hopping is progressively hindered. These difficulties are translated into the continual opening of a band gap (2-3). Once U/W is high enough the band is split into an occupied Lower Hubbard Band (LHB) and an empty Upper Hubbard Band (UHB) (4) which have a band gap between them, turning the material into an insulator [20] [21].

There are two main mechanisms to control the transition between a correlated metal and a Mott insulator. In first place one can alter the carrier density by chemical doping, thus, deviating the band from the half filling. Alternatively, the transition can be achieved reducing U/W and closing the gap, for example by the application of pressure [8].

2.2.2 Anderson Transition

Anderson transitions occur due to the amount of disorder in a metallic system. It is widely accepted that impurities can act as scattering centers in a metal crystal. Considering conduction electrons as planar waves, they will scatter in all possible directions when find an impurity. If one considers the phases of the scattered waves as completely random, the interference terms between them can be neglected and the conventional diffusive model of conduction arises. Nevertheless, this simplification cannot be applied in all

the situations. There is a probability for an electron starting at point A (Figure 2.3 (b)) that, after a finite number of scattering events, it returns to the same initial position as a backscattered electron. Moreover, there is also a probability for an electron to follow the exactly reverse path of scattering events. These two electron waves can interfere coherently with each other which enhance the amplitude of the waves and, therefore, the probability for this backscattering event to happen. These enhancing of the backscattered electrons probability by the interferences raises the resistivity of a material, since the backscattered electrons cannot contribute to the conduction when an electric field is applied. This decrease of the conductivity due to a minor disorder is known as weak localization. It is worth noting that if the phase coherence of the waves is broken by the application of a magnetic field the interference is weakened and the enhancing of the backscattering is reduced which results into the apparition of a negative magnetoresistance [20] [22] [23].

Weak localization phenomenon is the precursor of the Anderson insulators which are characterized by a strong disorder. When the disorder is increased enough the randomness of the system generates a potential well scenario where the wavefunction of the electrons becomes localized. This localization takes place due to the lack of admixture between orbitals with similar energy which would produce an extended wave along the material. While the nearby orbitals are too different in energy to produce this admixture, the same energy orbitals are too far from one to another to ensure a overlapping. Figure 2.3 (c) depicts a sketch of the localized waves (left) in comparison with the extended waves (right) that could be found in a metal [23] [24].

The localized states can be depicted in a density of states diagram using the so called mobility Edge (E_c) as can be observed in Figure 2.3 (d). Below this edge the states are localized (red band) and cannot contribute to the electric conduction. On the other hand, above this limit the delocalized or extended states (green band) are able to contribute to the conduction. Therefore if the Fermi level lies below the mobility edge the system will sense the localization and will behave as an insulator, while systems with Fermi levels above will behave as metals [20].

2.2.3 Resistive Switching in Materials with Metal-Insulator Transitions

As it has been seen, the mechanisms that lead metallic systems into insulators are completely different for Mott and Anderson transitions. Nevertheless, it is worth noting that in both cases the initial insulating state can be

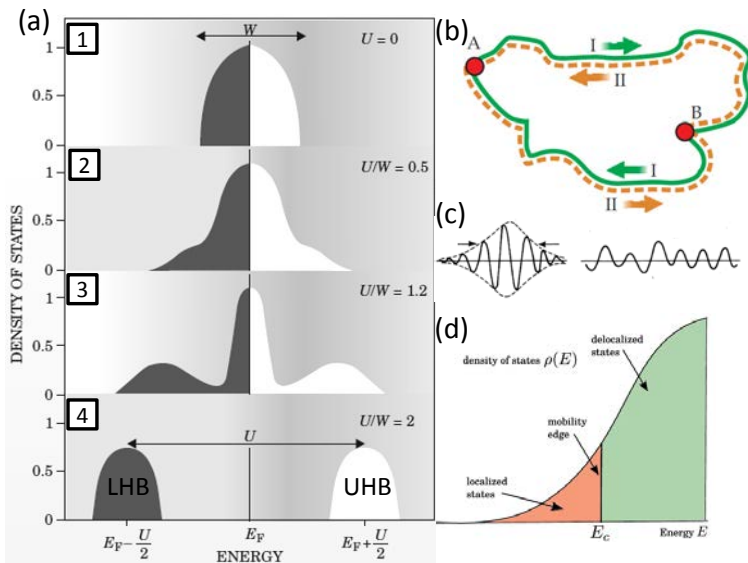


FIGURE 2.3: Sketch of the explained Metal Insulator Transitions. (a) Variations of the U/W parameter from a correlated metal (1) to a Mott Insulator (4) showing the progressive opening of the gap that leads to the LHB and the UHB [25]. (b) Sketch of the weak localization model, where a backscattered electron following a circular path (I) and a second electron following the reverse one (II) can interfere coherently enhancing the backscattering events [22]. (c) Localized electron waves in an Anderson insulator (left) and extended waves in a metal (right) [24]. (d) Density of states plot showing the separation between the extended states and the localized ones by the mobility edge (E_c) [26].

reversed due to the application of external stimuli leading the systems into a duality of resistance states that can be used in RS applications.

On one hand, Mott insulator systems and its influence on RS characteristics have been extensively investigated during the last decade. Mott Insulators (Figure 2.4 (a)) can be converted into correlated metals through controlling the bandwidth (Figure 2.4 (b)) or by filling the bands (Figure 2.4 (c) and (d)). In the first case the change in the resistivity is volatile and after the removal of the stimulus leading to the transition, such as pressure, electric field or temperature, the overlapping of the bands (Figure 2.4 (b)) ceases and the initial insulating state (Figure 2.4 (a)) is recovered. Contrarily to this, in the filled controlled mechanisms (Figure 2.4 (c) and (d)), which are triggered by doping with electrical transport carriers, the change is non-volatile due to the prevalence of the dopants even after the removal of the stimulus. This transition has been commonly achieved by the VCM, where

an increase (decrease) of the oxygen vacancies can lead to a system doped with electrons (holes). In the case of the electrons the LRS can be achieved if the Fermi level is increased until the UHB is reached, surpassing the band gap as depicted in the Figure 2.4 (c). Alternatively, if holes are considered the dopant carrier the Fermi level is decreased up to the LHB when the half filling is broken and the system switches into the LRS (Figure 2.4 (d)) [8] [9].

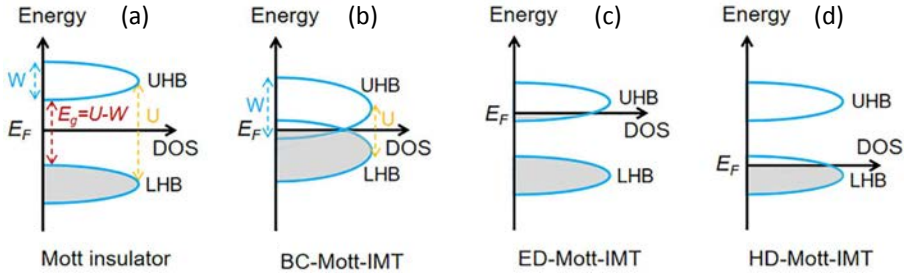


FIGURE 2.4: (a) Mott insulating state depicting the Energy gap generated by the electron correlation. (b) Bandwidth controlled transition where an increase of the bandwidth mixes the UHB and the LHB closing the gap. (c) Band filling controlled transition where the doping with electrons increases the Fermi level to the UHB. (d) Band Filling controlled transition where the doping with holes decreases the Fermi level below the limit of the LHB [9].

On the other hand, the reports of RS in Anderson insulators are still scarce [27] and there is not a solid understanding about the effect of oxygen vacancies on the RS in these materials. Nevertheless, one could argue theoretically that the migration or creation of oxygen vacancies could act as a carrier doping similarly to the Mott systems shifting the Fermi level to extended states and overcoming the insulating state. In this way the Anderson state (HRS) could be switched into the metallic behavior (LRS) assisted by the already explained VCM.

2.3 Strontium iridates

Since the first theoretical predictions of Mott [28] and Anderson [29] MITs, there has been a broad selection of materials that have proved experimentally these properties [30]. Some of these are TMOs materials that present a perovskite structure defined by the chemical general formula of ABO_3 . In this structure A and B are, in general, metallic cations placed at the corners and the center of the cubic crystal unit cell and B is coordinated by 6 shared Oxygen atoms which form an octahedron. On one hand, A cations have

usually closed-shell electronic configurations which makes them more stable and less responsive to perturbations and thus they play mainly a structural role in the perovskite. On the other hand, B partially filled orbitals provide a wider variability in the physical properties that can be even increased due to the structural modifications of the Oxygen octahedron. These distortions usually come from deviations in the relations of the radius of the A and B cations from the ideal ones. In order to evaluate these deviations, the so called tolerance factor can be used as in equation 2.1 :

$$t = \frac{r_A + r_X}{\sqrt{2} \cdot (r_B + r_X)} \quad (2.1)$$

Where r_A , r_B and r_X are the ionic radius of the A cation, the B cation and the Anion respectively. The ideal perovskite possesses a $t=1$ and any kind of deviation from this value could generate small distortions in the ideal cubic structure [31].

The ability of changing A and B cations within a wide selection of elements, along with the mentioned structural distortions, opens a scenario of multiple possibilities for tuning the physical properties of perovskites. This versatility makes perovskites useful not only to study new physical phenomena but also to implement technological devices [31]. These applications are based on properties such as multiferroicity [32], Colossal Magnetoresistance [33] or catalysis [34].

Among perovskite TMOs, those with the B position occupied by atoms with their 3d orbitals partially filled (commonly known as 3d TMOs) have been the ones more extensively studied, including some with the aforementioned MITs physics [35] [36]. Nevertheless, in the last years there has been an increasing interest for TMOs with partially filled 5d orbitals (5d TMOs). This group of oxides presents a larger spin orbit coupling (SOC) than its counterparts of 3d TMOs due to the strong dependence of SOC on the atomic number ($\text{SOC} \propto Z^4$). This phenomenon consists in the coupling between the atom's orbital and the electron's spin magnetic moments. Consequently, the two antiparallel spins in an orbital would act differently with the orbital moment changing their states energies and splitting the orbital [37]. The increment in the energy splitting due to the high SOC makes this contribution comparable to the other degeneracy breaking phenomena (the crystal field and the electron correlation) in 5d TMOs, which gives rise to novel properties and rich physics scenarios [38].

Among the 5d TMOs it can be found the strontium iridates Ruddlesden-Popper (RP) family with the general formula $\text{Sr}_{n+1}\text{Ir}_n\text{O}_{3n+1}$. The crystal structure of the members of this family can be described, in a similar way that other RP families (Figure 2.5), as n consecutive perovskite blocks

(SrIrO_3) separated between them by a rock salt (SrO). The principal members of this family, which are the most studied ones, are the $n=1$ (Sr_2IrO_4), the $n=2$ ($\text{Sr}_3\text{Ir}_2\text{O}_7$) and the $n=\infty$ (SrIrO_3) phases [38] [39].

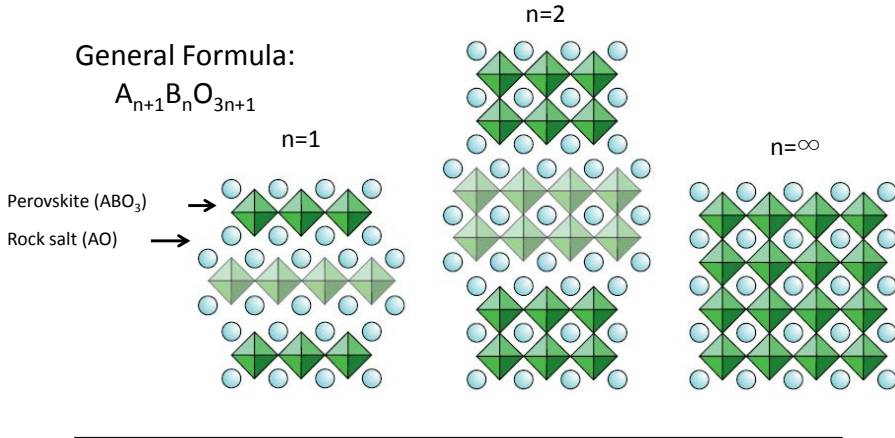


FIGURE 2.5: Examples of generic Ruddlesden-Popper phases, showing the repetition of n perovskite blocks (ABO_3) separated by a rock salt (AO) layer [39].

In all of these crystallographic structures, Ir^{4+} cations are placed inside an octahedron of Oxygen anions and, due to asymmetries with the crystal environment, the degeneracy of their 5d orbitals becomes split. Figure 2.6 (a) exemplifies the Crystal field splitting ($\Delta_{\text{oct}} \sim 2$ eV) on two groups of orbitals: the t_{2g} (lower in energy) which are composed by the d_{xy} , d_{xz} and d_{zy} atomic orbitals, and the e_g (higher in energy) which are composed by the atomic orbitals d_{z^2} and $d_{x^2-y^2}$. Moreover the t_{2g} group undergoes an additional splitting due to the SOC contribution ($\Lambda_{\text{SOC}} \sim 0.4$ eV) and breaks the lower energy levels into $J_{\text{eff}}=3/2$ and a $J_{\text{eff}}=1/2$ bands. Since the Ir^{4+} cation possess 5 electrons in their d orbitals, the $J_{\text{eff}}=3/2$ states are totally occupied while the $J_{\text{eff}}=1/2$ becomes half filled [20] [40].

According to band theory all the strontium iridates RP phases should present a metallic behavior, nevertheless, taking into account the electronic correlation contribution this prediction might not be accurate. In the case of the upper limit of the series, $n=\infty$ (SrIrO_3), this correlation is not strong enough ($U \sim 0.5$ eV) and the material presents a correlated metal band structure (figure 2.6 (b) left) with a metallic behavior, as expected. Nevertheless as the number of consecutive perovskite blocks becomes smaller (n decreases) the W becomes smaller, thus, increasing the U/W ratio. The decrease in the bandwidth opens progressively a gap in the middle of the $J_{\text{eff}}=1/2$ band driving the $n=2$ phase ($\text{Sr}_3\text{Ir}_2\text{O}_7$) into a barely insulator behavior (Figure 2.6 (b) center). Finally the gap is completely opened at the

Mott insulator $n=1$ phase (Sr_2IrO_4) separating the $J_{\text{eff}}=1/2$ band into the LHB and the UHB (Figure 2.6 (b) right) [10].

Without any further alterations $n=\infty$ will behave as a semimetal while $n=1$ phase will present insulator characteristics. However the proximity of these two compounds to the MIT makes them excellent candidates to test RS properties.

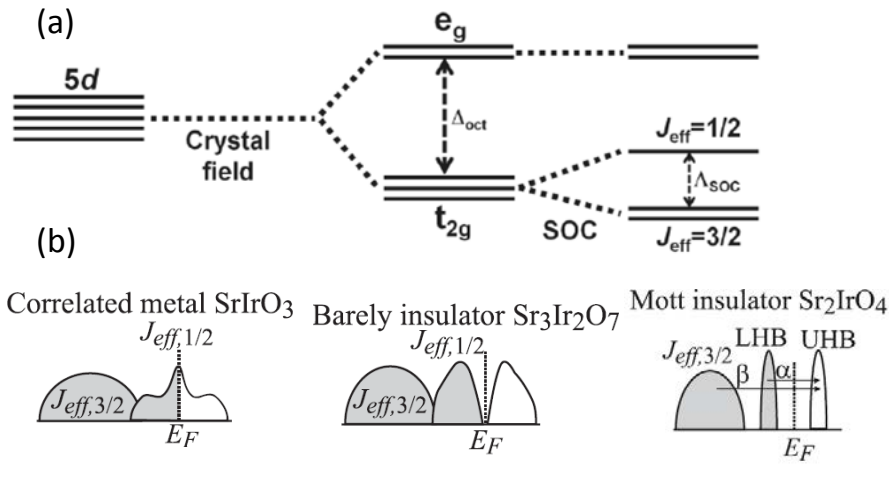


FIGURE 2.6: (a) Splitting of the 5d orbitals degeneracy in the cation Ir^{4+} due to the crystal field of the surrounding oxygen octahedral and the SOC contribution leaving a half filled $J_{\text{eff}}=1/2$ band [20]. (b) Progression in the splitting of the $J_{\text{eff}}=1/2$ band from a correlated metal (SrIrO_3) to a Mott insulator (Sr_2IrO_4) [10].

In the following subsections the members of this series that have been studied during this thesis are introduced in more detail.

2.3.1 Perovskite SrIrO_3 ($n=\infty$)

The semimetallic upper limit of the RP series is not the only phase with the chemical composition SrIrO_3 . Up to the moment there are two different reported structures in which SrIrO_3 can crystallize. On one hand, the hexagonal structure of SrIrO_3 (Figure 2.7 (a)) is the stable one at atmospheric conditions and can be obtained more easily at 900°C and ambient pressure. On the other hand, the orthorhombic structure (Figure 2.7 (b)) can only be achieved with synthesis at high pressures and temperatures of 1000°C [41]. As it can be appreciated in Figure 2.7 (b) this last structure can be visualized as two different distorted perovskites with 8 Ir-centered octahedra. These distortions from the ideal perovskite structure have their origin in

the deviation of the tolerance factor of the structure ($t=0.992$) from the ideal one ($t=1$) [42]. In order to simplify the epitaxial understanding and calculations, a pseudocubic approximation of this structure will be used in this thesis, as it is depicted in Figure 2.7 (c). Contrary to the hexagonal one, the orthorhombic structure is metastable in ambient conditions, which is the reason for the lack of reported single crystals in the literature. Nevertheless, it can be alternatively stabilized under the strain of an epitaxial growth in the thin film form using a variety of techniques [43] [44] [45] [46] [47].

The delicate interplay of the different energy contributions brings the band structure of the SrIrO_3 to a semimetallic ground state. Similarly to a metal, the Fermi level of a semimetal lays inside a partially filled band and its resistivity behavior follows $d\rho/dT > 0$. However, unlike a metal, the density of states of a semimetal is low near the Fermi level [48]. In the orthorhombic SrIrO_3 this ground semimetallic state is close to several MITs, which opens different scenarios where applying certain external perturbations the electrical transport of the phase can be tuned. It is worth noting also that the $n=\infty$ phase is also a very appealing candidate for spintronic devices that require a strong SOC and a high degree of conductivity [40].

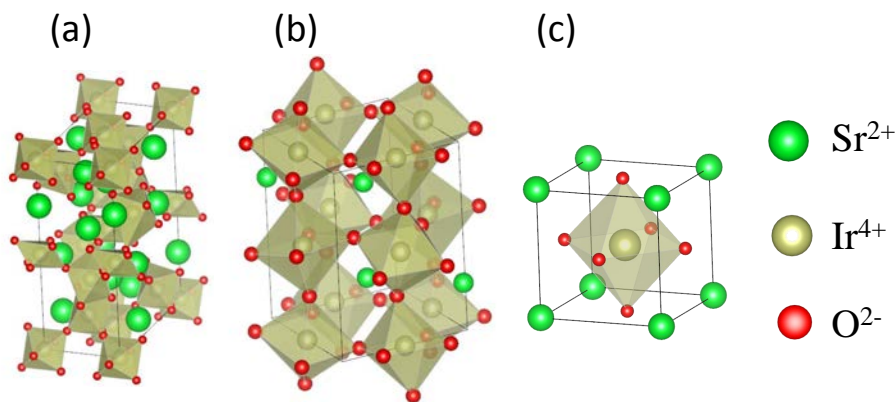


FIGURE 2.7: (a) Hexagonal structure of SrIrO_3 . (b) SrIrO_3 orthorhombic structure unit cell where two complete perovskites can be identified. (c) Pseudocubic structure of the orthorhombic phase centering the B position of the iridium (and its oxygen octahedron) in the middle of the unit cell.

2.3.2 Sr_2IrO_4 (n=1)

As explained above, the lower limit of the RP series, the n=1, consist in the alternation between perovskite and rock salt blocs in the c direction. This phase presents Mott insulator characteristics due to the shrinkage in the bandwidth. However, this state can be tuned and reversed using different strategies. Some studies have reported that the substitution of the cations can facilitate a carrier doping or a structural distortion system (alterations in the O-Ir-O angle). These effects can be then responsible for alterations in the band filling or the bandwidth modifications respectively, which could overcome or close the gap between the LHB and the UHB [49] [50] [51]. Moreover the O-Ir-O angle, and therefore the bandwidth, of the n=1 phase can be changed also by applying high electric fields [52] or by the local application of high pressures [12].

Chapter 3

Iridates thin film growth

The main concern of this thesis is to characterize both the macroscopic and local electrical properties of the strontium iridates. Nevertheless, high quality depositions of the specific phases need to be optimized first in order to study them. In this context, the literature shows that Ruddlesden-Popper (RP) strontium iridates thin films can be deposited using a variety of techniques as Molecular beam epitaxy [44], metal organic vapor deposition [47] or Pulsed Laser Deposition (PLD) [43]. In the case of Physical vapor deposition techniques, Strontium iridates have been mostly deposited by Pulsed Laser Deposition (PLD) [43] [53] [54] [55] while there are fewer reports using Sputtering technique [56]. Recent studies indicate that depositions carried out by PLD can be adjusted to grow the different RP phases from a single target of Sr_2IrO_4 ($n=1$) [53] [55] or SrIrO_3 ($n=\infty$) [54]. On the other hand, in the study where the films were deposited by Sputtering [56], a target of the non-RP phase Sr_4IrO_6 was employed to obtain the SrIrO_3 , reporting a loss of strontium in the deposition process. No other depositions carried out in a sputtering system have produce any other phase different from the $n=\infty$ one.

3.1 SrIrO_3 thin films growth

Due to the differences seen in the different deposition techniques and the scarcity of the studies using Sputtering to grow strontium iridates, the present chapter seeks not only to growth the different RP phases by but also to compare the different growth processes in the films grown by PLD and sputtering.

3.1.1 Target Fabrication

The first step to grow thin films of strontium iridates is to synthesize a target with the highest possible purity. Due to this a Sr_2IrO_4 target was manufactured, keeping a high Sr/Ir ratio (as in the case of the bibliographic sputtering studies) while giving the opportunity to compare the results with the more studied PLD depositions.

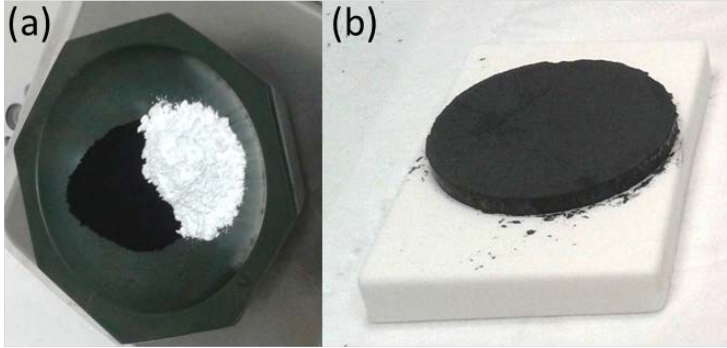
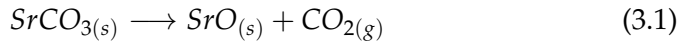
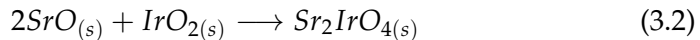


FIGURE 3.1: (a) Reactives used in the synthesis of the Sr_2IrO_4 target. The white powder corresponds to SrO and the black powder corresponds to IrO_2 . (b) Finished target of Sr_2IrO_4 .

Since $\text{SrO}_{(s)}$ is not stable during long periods of time, the reactive used as a source of strontium was $\text{SrCO}_{3(s)}$. First this reactive was calcined at 650°C at an oven in air atmosphere. The thermal energy causes the dehydration of $\text{SrCO}_{3(s)}$ and its further decomposition to $\text{SrO}_{(s)}$ (reaction 3.1), removing the carbon as $\text{CO}_{2(g)}$.



Once obtained, $\text{SrO}_{(s)}$ is mixed stoichiometrically with $\text{IrO}_{2(s)}$ (Figure 3.1 (a)) and heated to temperatures between 800°C - 980°C to induce the solid chemical reaction 3.2:



After every 12h in the oven at high temperature, the powder was mixed again and the process was repeated. The resultant powder was analyzed by means of powder X-Ray diffraction. In order to improve the purity of the target, heating and mixing cycles were repeated several times. Figure 3.2 depicts the θ - 2θ scans of the resultant powder after successive cycles of

heating and mixing and compares them to the theoretical calculated one [57]. In all the diffractograms the Sr_2IrO_4 phase was the dominant one, being the peak (103) the most intense one (as predicted in the theoretical diffractogram). In this Figure it can be observed how in the first cycles other phases of Strontium iridates are present as impurities.

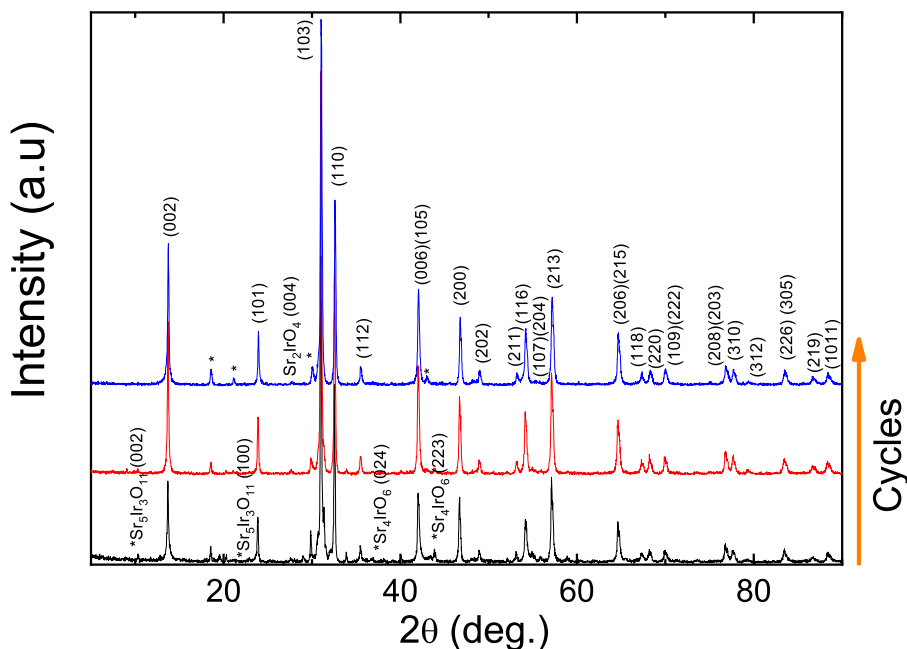


FIGURE 3.2: θ - 2θ scans of the target powder after the successive heating and mixing cycles (in order: black, red and blue) indexed with the theoretical diffractogram [57].

Nevertheless after several cycles these phases are progressively transformed into the $n=1$ phase and their peaks disappear. In the final diffractogram almost all peaks can be indexed as the Sr_2IrO_4 phase and only 4 peaks have remained unindexed and do not correspond to any usual RP phase nor any reactive. Moreover an Energy Dispersive X-ray Spectroscopy (EDX) performed in Scanning Electron microscopy (SEM) showed that no additional cations besides Sr and Ir are present in the target, discarding other types of impurities. Therefore, these peaks come probably from minor impurities of phases with Sr and Ir not yet identified. However, since

their composition is the same of the $n=1$ and their relative intensity is below 5 %, they are not expected to affect the posterior depositions. Once the powder had enough purity, it was compacted on a target by a hydraulic press and was hardened by a sintering process at 980°C during 48h (Figure 3.1 (b)).

3.1.2 Influence of the thermodynamic deposition conditions

As it has mentioned above, the studies regarding Strontium iridates thin films using Sputtering are very scarce [56]. Since Sputtering is considered one of the most used techniques to growth oxides [58] the study of the growth features of the strontium iridates RP family has a significant relevance. As it has been pointed above, in PLD more than one RP phase can be deposited from a single target only by adjusting the deposition conditions. In Reference [55], for example, the intensity of the plume is adjusted to selectively grow Sr_2IrO_4 or SrIrO_3 films. Other studies [53] [54] optimize the thermodynamic conditions of the deposition (oxygen pressure (PO_2) and Temperature (T)) to grow the different RP phases (SrIrO_3 , Sr_2IrO_4 and $\text{Sr}_3\text{Ir}_2\text{O}_7$). In Figure 3.3 are depicted the PLD reported phase diagrams. Although both of them do not fully coincide, it is clear that low PO_2 and high T displace the deposition toward lower n phases ($n=1$) while high PO_2 and lower T depositions tend to grow higher n phases ($n=\infty$). Moreover, both diagrams also coincide that between the extreme conditions a mixture of phases can be obtained.

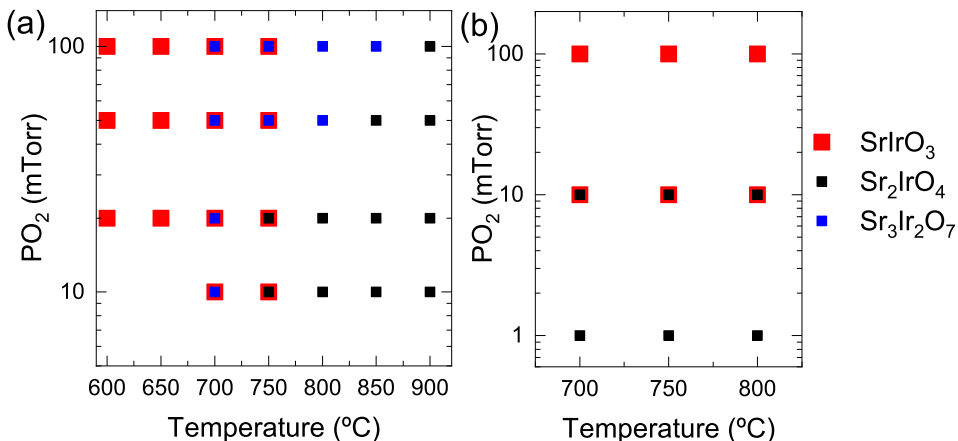


FIGURE 3.3: Phase diagrams of reported PLD growth studies. (a) Adapted from [54]. (b) Adapted from [53].

With the aim of evaluate how the PO₂ and the T influence the phase and morphology in sputtering deposition, a series of thin films were grown at different T and PO₂ on SrTiO₃ (STO) (001) substrates. The presence of the different RP phases in the depositions was evaluated by means of θ -2 θ scans while the topography of the films was measured by tapping AFM scans. The results of these depositions are depicted in Figures 3.4 and 3.5.

Figure 3.4 shows the impact of the temperature variations (from 500 °C to 900 °C) on the films while keeping the PO₂ at 140 mTorr. The AFM images expose a evolution from a flat film at 500°C to a film with holes at 700 °C and a progressive flattening of the surface to 900°C. These features can also be observed in the root mean square (rms) height distribution plot of the same Figure where the roughness of the film can be tracked at the different temperatures. The rms of a surface can be calculated as:

$$rms = \sqrt{\frac{1}{n} \cdot (z_1^2 + z_2^2 + \dots + z_n^2)} \quad (3.3)$$

Where n is the number of points and z is the height of each one of them.

The position of the film peak in the θ -2 θ scans coincide well with the (002) reflection of the SrIrO₃, which is indicative that the films that present a peak are composed by n=∞ phase. The structural features of the films will be discussed more deeply in the section 2 of this Chapter. It is clear also from this Figure that as the temperature decreases from 900°C the film loses crystallinity and finally no peak can be detected at 500°C.

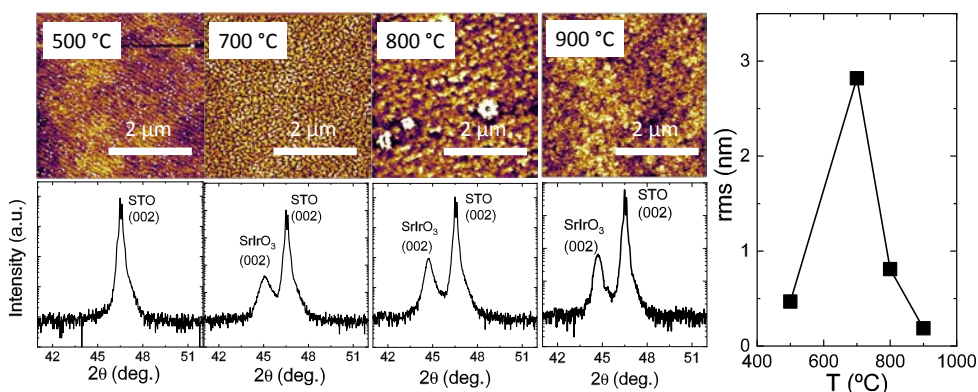


FIGURE 3.4: Evolution of the topography, the roughness and the crystallinity of the n=∞ films deposited at different temperatures with a constant pressure of 140 mTorr.

Figure 3.5 presents the evolution of the films as the PO_2 is shifted from 6 to 140 mTorr, in the depositions carried out at 900°C . The AFM images show a tendency for a 3D deposition at lower pressures, while higher pressures produce 2D growths. This variation in the morphology can also be observed in the rms plot which depicts a decrease of the roughness as the pressure is incremented. The differences in topography of these films will be explained in more detail in the section 3 of this Chapter. On the other hand no significant changes in the $n=\infty$ phase can be observed in the θ - 2θ scans and only a reduction in the intensity of the peak can be appreciated at low pressures.

In both Figures 3.4 and 3.5, only the (002) peaks of the $n=\infty$ phase were observed in all the measured X-Ray scans, even in the most favorable conditions for the $n=1$ deposition. Therefore, it can be deduced that there is a preferential growth of the $n=\infty$ phase in the films deposited by sputtering, in well accordance with ref [56]. As far as we know, no other phases have been obtained by sputtering, as it has been pointed in the introduction of this chapter.

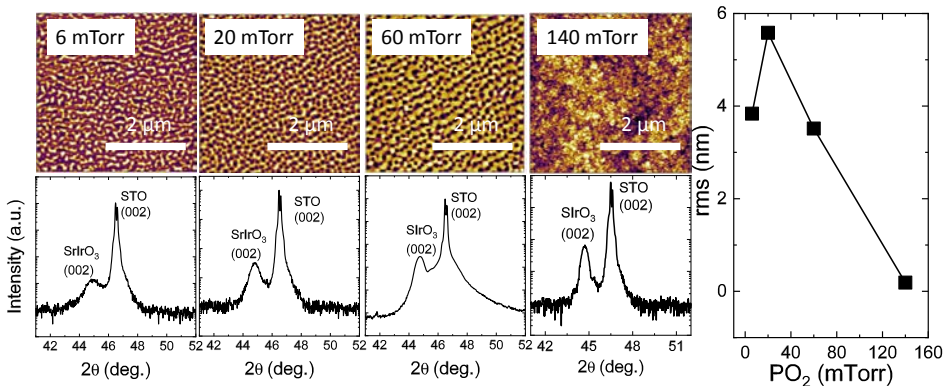


FIGURE 3.5: Characterization of the films deposited at 900°C and with different PO_2 .

The stoichiometry of the films can also play a relevant role in the physical properties of the system. Therefore its analysis can provide essential information about the system under study. To study the stoichiometry of the SrIrO_3 films, microprobe measurements were carried out. Since both the SrIrO_3 film and the STO substrate contain Oxygen and Strontium their signals could be mixed. Therefore the results obtained from a possible microprobe measurement would not be trustworthy. In order to solve this problem SrIrO_3 films were grown on LAO (LaAlO_3) and NGO (NdGaO_3)

substrates at the same conditions as the films on STO. Figure 3.6 depicts the θ - 2θ scans of the SrIrO₃ films deposited on the three different substrates. Both NGO (3.860 Å [59]) and LAO (3.791 Å [60]) substrates have lattice parameters smaller than the STO (3.905 Å) increasing, therefore, the mismatch between the substrate and the epitaxial film. In the (002) film reflection peak it can be observed that the crystallinity of the film decrease as the difference between the $n=\infty$ phase “bulk” lattice parameter and the lattice parameter of the substrate increases. Nevertheless only the (002) peak of the $n=\infty$ phase is present in the scans indicating the absence of other phases.

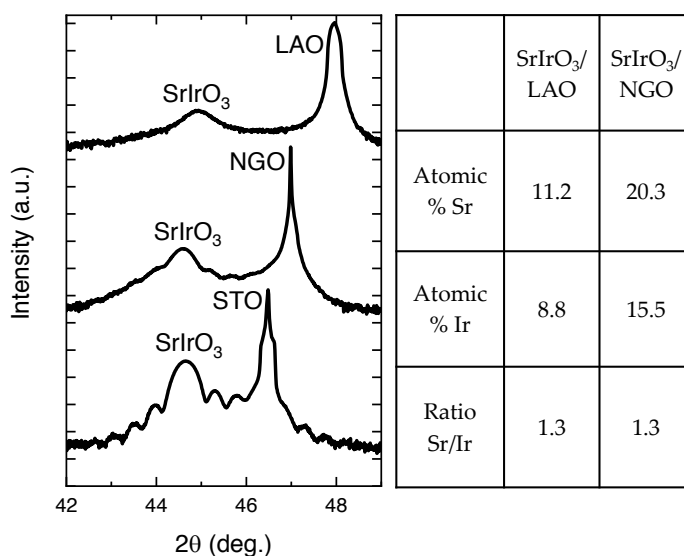


FIGURE 3.6: θ - 2θ scans of the SrIrO₃ films grown on STO, NGO and LAO substrates. It can be observed that the crystallinity of the film is reduced in substrates with a smaller lattice parameter. Table: results of the electron microprobe analysis where the predominance of Sr over Iridium can be visualized for both samples.

SrIrO₃/NGO and SrIrO₃/LAO films were characterized by electron microprobe. The results of these measurements are contained in the table of Figure 3.6. Since oxygen element is very light, its analysis could induce to errors and only the atomic percentage of Strontium and Iridium will be studied. From the results of the microprobe analysis it is clear that in both films Strontium predominates over Iridium while the nominal stoichiometric value of the SrIrO₃ predicts the same quantities. This can be clearly observed in the ratio between Sr/Ir, where in both samples there is 30% of additional Strontium. Although these results cannot be extrapolated directly

to the films grown on STO, their similarity indicates that can be treated as a good approximation. Moreover the X-Ray Photoelectron Spectroscopy (XPS) measurements on SrIrO₃ films on STO, which will be presented in section 2 of this Chapter, confirm these results.

3.1.3 Stoichiometry Modulation

As it has been commented above, Strontium Iridates have a very sensitive deposition process by PLD and even small changes in the plasma plume [55] [61] or the thermodynamic conditions [53] [54] can modify the deposited phase and the stoichiometry of the film. In the case of the Sputtering, both the present results and the bibliographic ones [56] suggest that the $n=\infty$ phase has a preferential growth, even coming from a non-stoichiometric target. It is also remarkable that this phase grows with an excellent crystallinity, as it will be studied in the section 2, in a non-nominal stoichiometry film. Regarding the mechanisms responsible for the Sputtering growth processes, two possible scenarios can be causing the present results:

- Although the target composition is rich in Strontium, not enough strontium arrives (or gets fixed) to the film allowing only the $n=\infty$ to growth and, therefore, preventing the formation of the other RP phases.
- The Sputtering depositions can only grow $n=\infty$ phase and, even in the case of the film receiving enough strontium, the structure prefers to accommodate non-nominal stoichiometry rather than grow in a different phase.

With the aim of elucidate this problem, the stoichiometry of the films has been studied changing the temperature of deposition and the position of the substrate from the target normal axis (Off axis growth). Moreover the obtained results were also compared with films grown by PLD to give insights on the differences observed in the bibliography and in the films grown in the present work.

On one hand, films grown by PLD were deposited at an oxygen atmosphere of 70mTorr with 1200 pulses of a KrF excimer laser at a laser fluence of 1.25 J/cm² (1Hz). On the other hand, the films grown by sputtering were deposited at 140 mTorr and 20W of RF power. The comparison between the two methodologies was carried out only with films grown at different temperatures since the different geometry in the deposition of PLD and sputtering complicates the contrast in films grown off-axis.

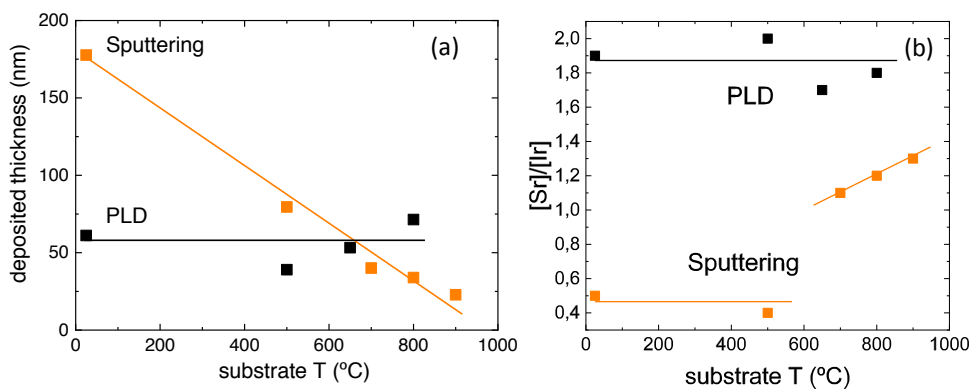


FIGURE 3.7: Variations of (a) thickness (measured by reflectometry) and (b) stoichiometry of the films (measured by electron microprobe) due to changes in the substrate temperature. The iridate films were grown by PLD and Sputtering.

Figure 3.7 depicts the changes in thickness and composition of the iridate films when deposited at different substrate temperatures by PLD and Sputtering. In this Figure it can be observed that PLD and Sputtering follow completely different trends when the temperature of the substrate is increased. On one hand, PLD films do not show any clear correlation between temperature and thickness (Figure 3.7 (a)) or with the stoichiometry of the film (Figure 3.7 (b)), the observed small fluctuations may be attributed to experimental variability. On the other hand, the depositions carried out by Sputtering show clear trends in both quantities. It can be clearly observed in Figure 3.7 (a) that the thickness of the resultant film follows a relation of proportionality with the temperature being its coefficient negative. It is worth to mention that the thickness of a film deposited at 900°C is an order of magnitude less than the thickness of the film when deposited at room temperature. Since the generated plasma in the Sputtering depositions should not be affected by the substrate temperature it is evident that the sputtering rate and the arrival of sputtered atoms to the substrate are not altered. Therefore the large variation of thickness with temperature can only be explained by the phenomena of resputtering, where the material of the forming layer is removed from the substrate after arrives to it.

In the resputtering processes, energetic particles, generated by the plasma, bombard the substrate where the film is growing. These particles cause the reemission of the film adatoms reducing therefore their sticking probabilities. The resputtering effects can be enhanced by increasing the

temperature of the substrate. An increment in the value of the temperature increases the mobility and decreases the binding energy of the adatoms reducing this way the threshold of energy necessary for their reemission [58].

The variation of the composition depicted on Figure 3.7 (b) for the Sputtering deposited films suggests that the observed resputtering evolves differently with temperature in each one of the elements that form the film. In this Figure it can be observed that at high temperatures the film is richer in strontium in comparison to low temperatures, which indicates an enhancement of the resputtering of iridium at high temperatures.

Nevertheless in the whole range of measured temperatures the $[Sr]/[Ir]$ ratio is lower than the one of the target ($[Sr]/[Ir]=2$). These results can be explained by an inhomogeneous plume composition if it is assumed that at other deposition angles the $[Sr]/[Ir]$ ratio would be higher.

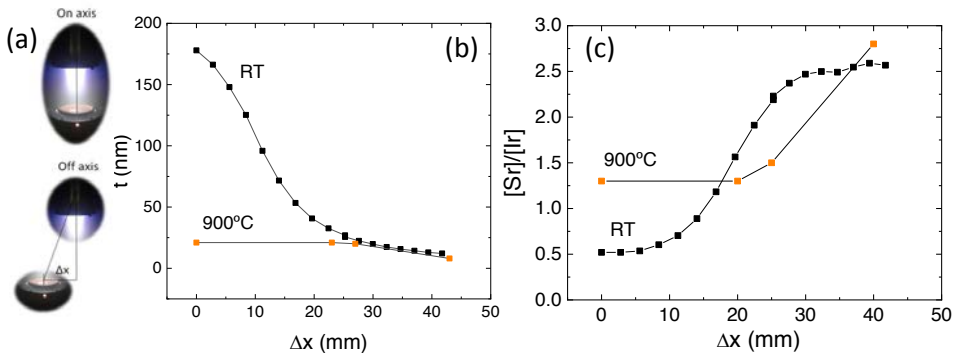


FIGURE 3.8: Off-axis growth in Sputtering. (a) Scheme comparing the usual growth (on axis, where the normal axis of the center of the target coincides with the normal axis of the substrate) and the off axis growth (where the normal axis of the substrate are parallel to the on axis configuration and separated by a distance Δx). (b) Thickness of the films after 1h of deposition at 20 W at different Δx (both at Room temperature and at 900°C). (c) $[Sr]/[Ir]$ rate at different Δx (both at 900°C and Room temperature).

With the goal of resolve this question the growth of the films was evaluated as a function of the distance between the normal axis of the substrate and the target (Δx) in what is called off-axis deposition (Figure 3.8 (a)). The results of the depositions at Room temperature (RT) and at 900°C at different positions of Δx are depicted in Figures 3.8 (b) and (c). In Figure 3.8 (b) it can be observed that when deposited at RT the thickness of the film decreases with Δx . The most relevant variation is comprised between 0 and 25 mm where the drop in thickness is almost an order of magnitude. After this, the thickness follows a smooth decrease tendency with Δx . At

high temperature (900°C) the behavior of this curve is significantly different. Between 0 and 25 mm the thickness of the film remains constant and only at higher Δx values a reduction in the thickness can be perceived. It is clear from this Figure that the differences in temperature already observed in Figure 3.7 (a) are extended from 0 up to 25 mm, where both curves converge at similar values and follow the same decrease pattern. However, it is worth noting that the thickness of the films at RT is always higher than the ones grown at 900°C. These differences support the previous mentioned resputtering evidences, since differences in the thickness of the deposition do not only arise from the temperature but also from the geometrical position of the growing film in respect to the target. That is, at a certain range of positions the film is more heavily affected by the energetic particles that cause the resputtering. When removed from this range, the differences between the depositions at RT and 900°C are decreased because even if the threshold to reemit adatoms is decreased (at 900°C), the large reduction of energetic particles prevents them from being resputtered. The constant decrease of the thickness followed by both temperature curves can be attributed to a decrease quantity of material that arrives to the substrate at higher Δx values.

Figure 3.8 (c) shows the differences of stoichiometry of the deposited films as a function of Δx . Again the RT depositions follow a different trend in front of the depositions carried out at 900°C. At RT the “on axis” deposition has a Sr/Ir ratio of 0.5 which is kept constant up to 10 mm. Then, the ratio rises smoothly between 10 and 30 mm where a new plateau is defined at a ratio of Sr/Ir=2.5. It is clear then that geometry of the deposition has a very significant impact on the stoichiometry of the film where the [Sr]/[Ir] can be increased up to 5 times changing the position of the substrate. At 900°C the “on axis” deposition resulted in a composition of Sr/Ir of 1.3 which is kept constant up to 20 mm where the Sr/Ir ratio starts to increase. In both Figures 3.8 (b) and (c), the 900°C and the RT curves start at different values and cross each other around 20 mm. Beyond that value the lines start to have the same tendency. However, in the case of the stoichiometry measurements the exact values do not correspond exactly confirming the presence of a small remaining resputtering even at high Δx values. On the other hand, the clear variation of composition between the strontium deficient “on axis” deposition ([Sr]/[Ir]=0.5) to the strontium surplus “off axis” deposition at 4 cm ([Sr]/[Ir]=2.5) at RT (where less resputtering occurs) confirms the proposed inhomogeneity of the plume.

As observed in the previous XRD measurements (Figure 3.4), only at high temperatures (700 - 900°C) the deposited layer can crystallize in an epitaxial film. Therefore the variations in the stoichiometry obtained with

changes in temperature do not imply the apparition of other phases. Moreover, the variation of composition with temperature only oscillates between ratios of 1.1 and 1.3 in the suitable range and therefore only the $n=\infty$ phase can be growth as can be observed in the θ - 2θ scans in Figure 3.4. On the other hand, the variations of stoichiometry generated by the displacements in Δx are larger even at 900°C (1.3-2.8). In order to further study if the variations of stoichiometry observed in Figure 3.8 (c) have induced the apparition of other phases, the deposited films were evaluated by θ - 2θ scans (Figure 3.9).

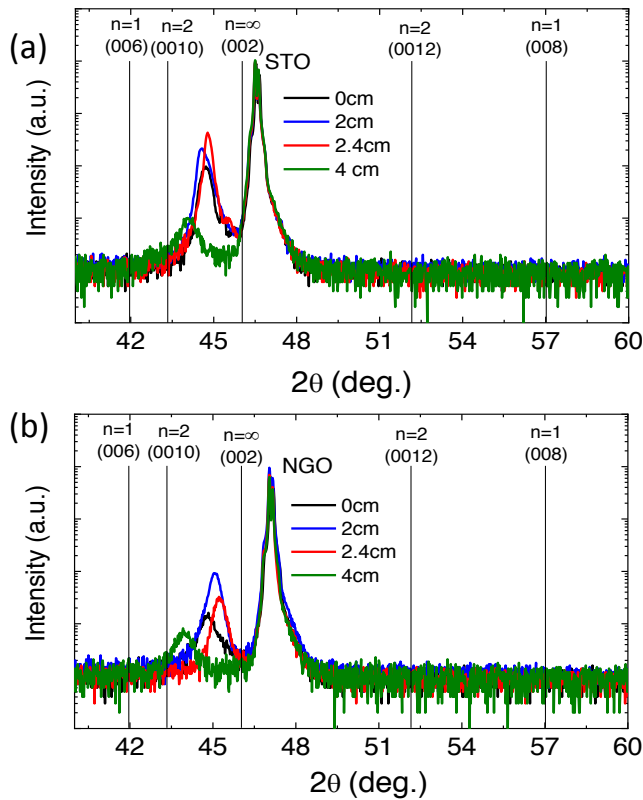


FIGURE 3.9: θ - 2θ measurements of the (a) SIO/STO and (b) SIO/NGO films deposited at 900°C at different Δx positions. The variations of intensity can be attributed to different thicknesses of the films.

Both sets of films deposited on STO (Figure 3.9 (a)) and on NGO (Figure 3.9 (b)) show a similar behavior where the position of the (002) peak of the film remains almost constant without a clear tendency from the “on axis” position to $\Delta x=2.4$ cm. Above this value the peak clearly shifts to

lower 2θ values. All the film peaks are located between the theoretical (002) reflection of the $n=\infty$ and the (0010) reflection of the $n=2$. However, in all 4 films only the family of peaks (001) of the $n=\infty$ phase can be observed, discarding therefore any possibility of the presence of other RP phases such as the $n=1$ or the $n=2$. This is especially relevant for the films grown at 2.4 cm and 4 cm which present a [Sr]/[Ir] ratio of 1.5 and 2.8 respectively. In the case of the films grown at 2.4 cm the stoichiometry is more similar to the $n=2$ RP phase ([Sr]/[Ir]=1.5) than to the $n=\infty$ ([Sr]/[Ir]=1) one, nevertheless the film grows with a good crystallinity into the perovskite like phase. In agreement with this case, the film grown at 4 cm presents similar peaks to the $n=\infty$ phase with an appreciable displacement of the peak that, due to the lack of the additional reflections, cannot be attributed to other phases. In this last case the [Sr]/[Ir] ratio is even higher than the most Strontium rich component of the series, the $n=1$ ([Sr]/[Ir]=2).

It can be concluded then that even if the film disposes of enough Strontium to grow into another RP phases it prefers to crystallize into the $n=\infty$ phase, accommodating, if necessary, large variations of stoichiometry. A possible explanation for the stoichiometry variation could be the presence of Sr segregations within the films. However, to fully understand the behavior of strongly "off axis" films, in particular stoichiometry accommodation, a deep microscopic study would be required, which it is beyond of the scope of the present work.

As it is explained above, it has been reported that by PLD one can grow the different RP phases from a single target. Although the ability to grow different iridate pure phases is relative recent, a wide range of research groups have achieved it. Moreover, the capacity to change the deposited phase by altering the conditions of the growth has been accomplished following different strategies. Some reports rely on the variation of thermodynamic conditions ($T_{substrate}$ and PO_2) of the phases (already reported in polycrystalline samples [62]) and the equilibrium processes between them to explain the origin of the resultant phases [53] [54]. On the other hand, other studies invoke the kinetic conditions, such as the plume dimensions [55], the plume composition distribution [61] or the epitaxial strain [63] to clarify it.

A global vision of all these studies suggests that this deposition system in PLD is in a very subtle equilibrium between thermodynamics and kinetics and the alteration of any of the deposition parameters can favor one phase or another one. This delicate equilibrium is completely collapsed in the case of Sputtering deposition. The present results point out that in Sputtering deposition, unlike PLD, most of the material is removed from the film after being deposited. This much more kinetic dependent scenario

is probably the main reason to explain the clear differences between the bibliographic reported depositions by PLD and the present studies carried out by Sputtering.

3.2 Microstructural Characterization of flat SrIrO_3 films

3.2.1 Topographic Characterization

Due to their flat morphology and good crystallinity, the SrIrO_3 films grown at 900°C and 140mTorr of PO_2 are then the optimal ones to perform further studies on macroscopic and local electric properties. Particularly, these conditions will be used to grow a series of flat films with different thicknesses, as it will be explained in Chapter 4. Therefore, a deeper characterization of their structural and stoichiometric properties was carried out.

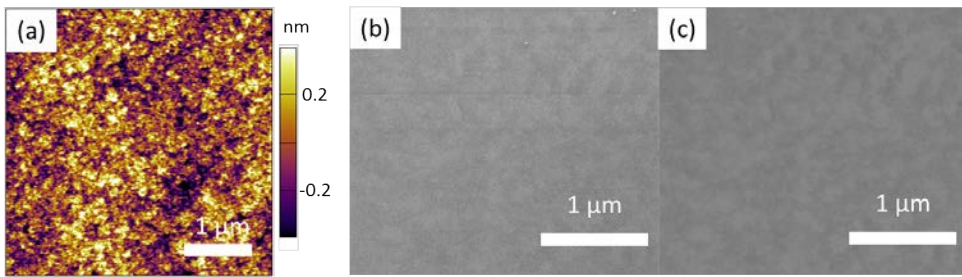


FIGURE 3.10: (a) AFM topography image of a SrIrO_3 film. The roughness of the films quantified as rms is below 0.2 nm (b) Secondary electrons SEM image. (c) Backscattered electrons SEM image. The absence of contrast is produced by a homogenous surface film composition.

Figure 3.10 depicts the images obtained by AFM and SEM on the optimized $n=\infty$ films. In both AFM and secondary electron SEM measurements (Figure 3.10 (a) and (b) respectively) the films show a flat surface. rms of the film calculated from the AFM data is below 0.2 nm which means that the surface roughness is at the same level than the one of the terraces of the underlying substrates. Figure 3.10 (c) shows the image formed by the backscattered electrons in the SEM measurement. The clear similitude between the secondary and backscattered electron images indicates that only the topography is influencing both images. Moreover, the lack of a clear contrast between different zones of the film indicates a homogeneous composition of the film without any clear segregation. Additionally, no clear local structure features such as twinning can be appreciated.

3.2.2 Transmission Electron Microscopy

With the aim of studying more deeply the structure of the film, cross-section Transmission Electron Microscopy (TEM) measurements were performed (Figure 3.11). In Figure 3.11 (a) the direct lattice of the SrIrO₃/STO heterostructure can be visualized with two differentiated regions. The inset adjacent to area 1 is a filtered image of this region to better visualize the atomic structure. Figures 3.11 (b) and (c) depict the Fast Fourier Transform (FFT) patterns corresponding to areas 1 and 2 respectively.

It can be observed that the FFT from region 1 (far from the interface) exhibits weak spots doubling the periodicity of the basic cubic perovskite unit cell along the interface plane, while in the FFT from region 2 (close to the interface) these spots are absent. Figure 3.11 (d) shows the simulation of the [1 0 1] zone axis electron diffraction pattern for a Pnma structure. Spots marked in yellow correspond to double diffraction. It can be observed that, including the latter, the agreement between the experimental and calculated patterns is excellent, in consistency also with the orthorhombic structure oriented such that the b-axis is parallel to the interface. The TEM image (Figure 3.11 (a)) exhibits blurred dark contrasts that affect the film but not the substrate images, indicating a strong sensitivity of the SrIrO₃ phase to the TEM sample preparation process, which is described in Appendix A. In fact, cross section TEM images of the orthorhombic SrIrO₃ phase, such as the present ones, are scarce in the bibliography [11] [64] [65] which indicates the challenging nature of this process.

Despite the poor quality of the image does not allow making a deep quantitative analysis of the measurements, we performed image simulations to check the correspondence between the contrast features of the experimental image and those corresponding to the proposed Pnma model obtained from [42]. Image simulations of the film and the substrate are shown as insets in the upper and bottom left corners of the image (defocus 82nm, thickness 5nm), indicating good matching with the experimental image. According to the simulation, the most intense dots correspond to Sr columns. These results indicate that beyond a certain distance from the interface, both the direct image and the FFT of the observed film are in well agreement with the perovskite SrIrO₃ phase described in the XRD measurements. This structure can be related with the Pnma space group simulated which coincides with the published resolution [42]. Moreover, no signs of strontium excess in the form of segregations can be identified, discarding this as a possible explanation for the previously observed [Sr]/[Ir]=1.3 ratio. It is worth noting also the absence of intergrowth of other RP phases in the present image.

In addition to the structural and defects information of the film, TEM cross section images also allow observing directly the interphase between the substrate and the film. Here it can be observed that the interphase between the SrIrO_3 film and the STO substrate is not completely sharp even having tested previously that the substrate had an rms below 0.2 nm. This is in well agreement with the XPS results, which will be presented below, that showed a soft transition between the film and the substrate and seems to indicate that the substrate and the film might be suffering interdiffusion at the interphase.

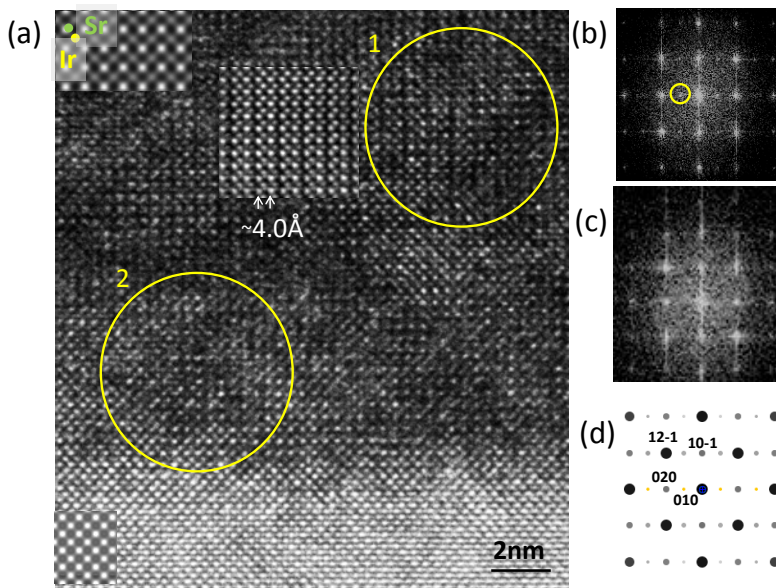


FIGURE 3.11: Cross section TEM measurements of a $\text{SrIrO}_3/\text{STO}$ film. (a) Image of the direct lattice marking two different regions. At the left of the first region a filtered image is depicted. At the superior and inferior left corners of the image a simulation of the SrIrO_3 phase and the STO substrate are depicted. (b) and (c) present the FFT of the regions 1 and 2 respectively. In the first region an additional set of peaks generated by double diffraction are marked with a circle. (d) Simulation of the FFT for a PNMA structure presenting the correspondence of each one of the observable reflections into the lattice planes.

3.2.3 X-Ray Photoelectron Spectrometry

In order to expand the initial knowledge on the stoichiometry of the films, a depth profile of the composition of a $\text{SrIrO}_3/\text{STO}$ film was evaluated by

means of XPS. With this technique the stoichiometry of films grown on STO can be directly analyzed, moreover this technique can provide insights on the presence or absence of contaminants.

To perform these measurements it was necessary first to calibrate the rate of attack of the ion milling technique at a certain conditions. This calibration was carried out by creating a pattern of squares and lines by photolithography in a flat film with a known thickness. Each one of these squares was exposed during different amounts of times to ion milling. Afterwards, the depth in each square could be measured performing an AFM profile. The ion milling rate of attack could then be fitted by a linear regression, and therefore the time of attack of the measured samples can be translated into the remaining thickness of the film. In our case the estimated ion milling rate was 0.2 nm /s.

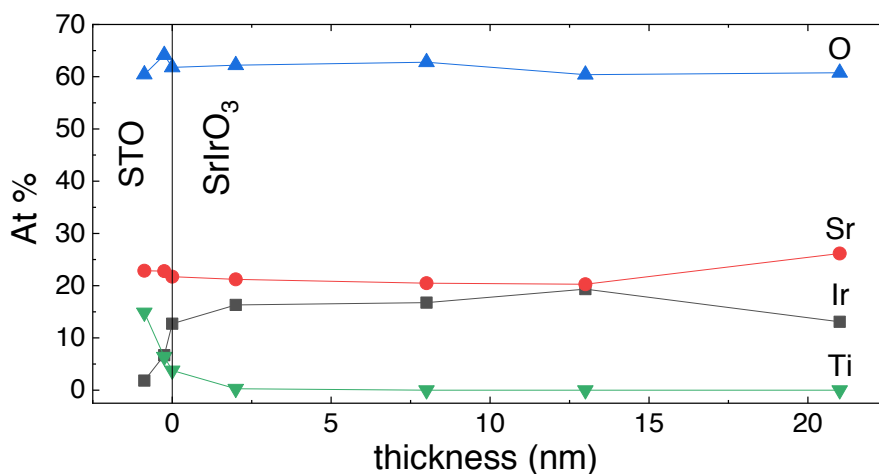


FIGURE 3.12: XPS percentage atomic profile of the different ions present in the SrIrO₃/STO films. Data is represented as a function of the film thickness from the interphase with the substrate.

Figure 3.12 depicts the Atomic percentages of the different ionic species present in the substrate and the film as a function of the depth. As it can be observed in the graph, the oxygen At % (blue triangles) takes values around 60% during the whole film and in the substrate, which is in good agreement with the nominal value in perovskites (ABO₃). On the other hand, Strontium cations (red circles) seem to have a higher concentration at the surface of the film (>25%) and after the first nanometers they decay to a constant value slightly above the nominal 20%. Since both the film and the substrate have the same nominal value for Sr, once crossed the interphase the

Atomic % of the Sr is maintained constant. Iridium cations (black squares) represent only the 13% of the atoms at the surface, compensating this way the overpopulation of Sr. Beyond the surface, the value of the Ir cations increases and it is stabilized at values of 16-19% which are slightly below the nominal value (20%). When the thickness of the film is approaching the interphase, the iridium starts to decrease smoothly first, and more abruptly after the interphase. Titanium atoms (green triangles) do not appear up to 2 nm from the interphase when their proportion start rising slowly to the interphase and more sharply after it. The Iridium and Titanium atoms describe a clearly concomitant dependence near the interphase showing a decrease of Ir atoms of the film while the signal of the Ti atoms of the substrate is increased.

With the present measurements several conclusions can be stated. In first place, it can be observed that at the surface of the film there is a higher [Sr]/[Ir] ratio than in the rest of the film suggesting an excess of Sr at the surface or an increase of the Ir vacancies at it. The composition of the inner film seems to be constant with a clear predominance of the Sr ions over the Ir. Nevertheless no titanium cations from the substrate occupy the B positions in the film. The lack of this interdiffusion indicates the presence of Ir vacancies in the film. It could be also possible that a certain amount of Sr vacancies were present in the film, nevertheless these cannot be observed directly by XPS due to the At % also depends on the O (which could have vacancies as well).

It can also be observed that the Ir and Ti cations change progressively in the surroundings of the interphase. The broadness of the thickness associated with this transition can be explained by two factors. In the first place the film/substrate interphase has a certain roughness which broadens this transition. Moreover the XPS technique has a certain range of penetration on the measured sample and it is possible that Ti signals starts arising even before the whole SrIrO₃ film has been removed by the ion milling.

Analyzing the [Sr]/[Ir] ratio in the different sections from the surface to the surroundings of the interphase (2-21 nm) an estimation of the stoichiometry of the whole film can be made. Weighting every section by their length and assigning the [Sr]/[Ir] of the average of both of its extremes the calculated ratio is [Sr]/[Ir]=1.30. It is worth noting that this estimation is in a very good agreement with the ratios calculated by electron microprobe on NGO and LAO substrates, therefore proving that electron microprobe measurements are indeed a good approximation to the films deposited on STO.

3.2.4 X-Ray Diffraction

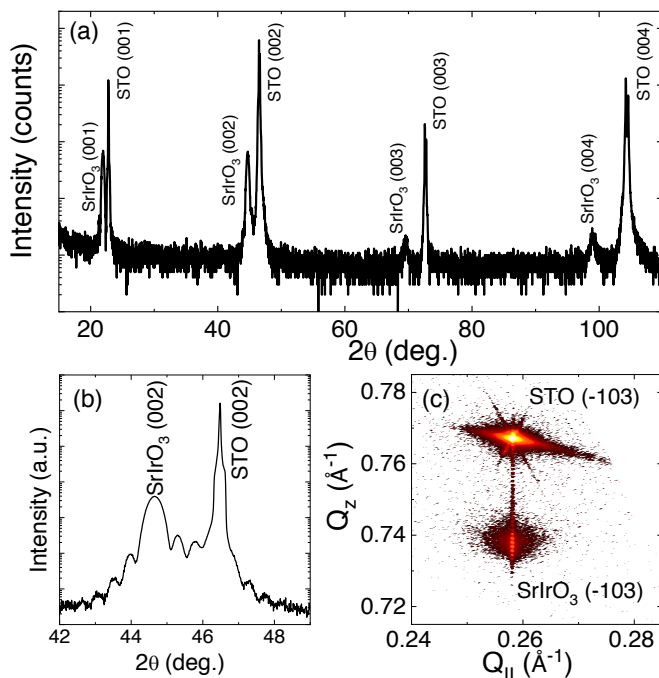


FIGURE 3.13: X-Ray diffraction measurements of a 21 nm film. (a) Complete θ - 2θ scan where only the (001) peaks of the film are present. (b) High Resolution θ - 2θ scan of the (002) reflection. The thickness fringes surrounding the film peak indicate the high crystallinity of the film. (c) Reciprocal Space Map of the (-103) reflection, the fully strained nature of the film can be deduced by the coincidence of both peaks at the same Q_{\parallel}

The structural characterization of the films has been performed by X-Ray diffraction techniques. Figure 3.13 (a) shows a complete θ - 2θ scan of a film with 21 nm of thickness. Besides the substrate reflections, only the (001) family of peaks of the film can be observed indicating the purity of the deposited phase and its epitaxial growth on STO (001). In Figure 3.13 (b) the high resolution scan of the (002) reflection can be observed. In this scan a series of fringes appear around the SrIrO₃ (002) reflection. These oscillations are generated by the diffraction of the incident X-Rays with the finite planes of the film that have coherent thickness. The presence of these satellites is indicative of a high crystallinity of the film and its analysis confirms a thickness of 20 nm, which is in good agreement with the 21 nm obtained by the reflectometry measurement. The (002) peak of the film is centered

at 44.66° which corresponds to an out of plane parameter “ c ” of 4.056 \AA calculated by the Bragg’s law. This value is significantly larger compared to the bulk value (3.943 \AA) [42] and corresponds to an out-of-plane strain of 2.87% (pseudocubic notation is used for simplicity). This elongation is caused by the elastic behavior of the film when is forced to compress its in-plane parameter to the one imposed by the substrate ($a_{STO} = 3.905 \text{ \AA}$). The phenomenon responsible for this is known as Poisson effect and states that if a material is subjected to a strain in a direction it can react with a deformation in the orthogonal direction [66].

These deformations can be studied with more detail in an asymmetric reflection RSM. Figure 3.13 (c) depicts a reciprocal space map of the (-103) reflection of the STO substrate and the SrIrO₃ film. Both the peak of the film and the peak of the substrate appear at the same in-plane reciprocal vector (Q_{\parallel}) which indicates that they have the same in-plane parameter and confirms the fully strained nature of the films. The compressive in-plane strain of the film is -0.96%.

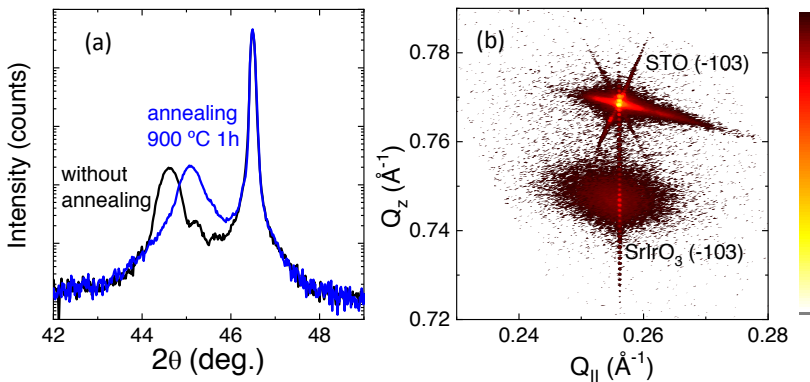


FIGURE 3.14: (a) θ - 2θ scans of SrIrO₃ films with (blue line) and without (black line) “in situ” annealing. The change in the position of the peak towards larger values indicates an oxygenation process in the annealing and therefore suggests the presence of oxygen vacancies in the non-annealed films. (b) RSM of the (-103) peak of film grown with 1h of annealing.

The degree of oxygenation in perovskites can be a key factor for transport properties. In order to check if the films have oxygen vacancies, SrIrO₃ films were grown at the same conditions but adding an annealing step after the deposition. The annealing consisted in keeping the sample during 1 hour at 900°C with an Oxygen atmosphere (370 Torr). In this way the film

increases its oxygenation level, which could cause changes in the crystallographic structure. Figure 3.14 (a) depicts the comparison between the θ - 2θ scans of SrIrO₃ films with and without annealing. Here it can be observed that the (002) peak is shifted to higher values. This is the consequence of the oxygenation of the film that has shrunk the unit cell of the perovskite reducing the out of plane lattice parameter. The change in the structure due to the oxygenation suggests an extended presence of Oxygen vacancies in the samples without annealing. This hypothesis can be further confirmed by comparing the volumes of the unit cells. Both films are fully strained with the STO substrates, as it can be observed in the RSMs of Figure 3.13 (c) and 3.14 (b), this means that they both have the same in-plane parameters of the STO (3.905 Å). The out-of-plane parameter can be calculated with the θ - 2θ scans using the Bragg's law and it is 4.056 Å for the film without annealing and 4.021 Å for the annealed film. Therefore the volumes of the pseudo-unit cells, assuming that they are tetragonal, are 61.82 Å³ and 61.32 Å³ for the films without and with annealing respectively. Employing the pseudocubic unit cell of the SrIrO₃ with a lattice parameter of 3.943 Å [42] the calculated volume of the cell would be 61.30 Å³ which is in a good agreement with the one of the annealed film. The coincidence of these two values, while the one of the non-annealed sample being slightly larger, is a clear indicator of an elongation of the unit cell due to oxygen vacancies and reinforces the already mentioned hypothesis.

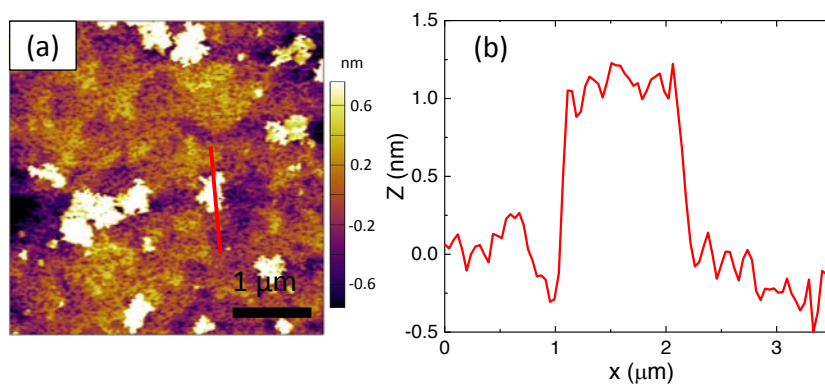


FIGURE 3.15: Topography characterization of a SrIrO₃ film grown at 900°C and 140 mTorr with a 1 h post annealing at 370 Torr and 900°C. (a) 4x4 μm² AFM image of the film showing the presence of islands. (b) Profile of the island marked with a red line in (a). The main height of the islands is ~ 1 nm above the film.

The topography of the annealed film can be appreciated in Figure 3.15

(a). Although the film conserves the flat topography already seen in the non-annealed films, flat islands of $\sim 1 \mu\text{m}^2$ of area appear covering a significant part of the film. Figure 3.15 (b) depicts the profile of an island of the previous image (marked with a red line) which shows that the islands have a mean height of $\sim 1 \text{ nm}$. Since the final porpoise of the films is to perform local electrical measurements with C-AFM, these islands of unknown composition could alter the results adding a new degree of complexity. In order to avoid this, this annealing step will not be performed in the optimized films prepared for further measurements. The films grown for the RS measurements will, thus, have a certain amount of initial oxygen vacancies. However, some studies relate the presence of these vacancies to an improving in the switching behavior in TMOs [67].

3.2.5 Stability of the films

To assess the stability of the films a resistivity measurement was performed in the same film during several months, the results are depicted in Figure 3.16 (a). The resistivity of the film is clearly in a metallic regime in a wide range of temperature except at low temperatures where a small upturn can be observed. These results are in a good agreement with the ones published in the bibliography [11] [68] [69] and will be more carefully studied in the chapter 4 of this thesis.

After the deposition, the sample was stored in a low humidity atmosphere while the resistivity was measured periodically. As it can be observed, the behavior of the resistivity curves remains unaltered through the months and the resistivity suffers only a slight increase of 0.3% from its initial value (Figure 3.16 (a) Inset). The small increase in the resistivity is a clear sign of an excellent stability of the inner part of the film and allows carrying on macroscopic transport measurements without the need of capping the film, which would make a more complex heterostructure to study. Nevertheless, during the course of the thesis it was observed that the surface of the films is progressively altered with time. Figure 3.16 (b) depicts a table of the composition percentages, measured by XPS, of a film surface at the day of the deposition and 5 months later. No major differences in the stoichiometry of the surface can be observed with time indicating that the film remains stable with time. It is worth noting that, as in the previous XPS measurements, the surface of the film is rich in strontium reaching a ratio of $[\text{Sr}]/[\text{Ir}]=1.7-1.8$.

Additionally, AFM tapping images were obtained in the same interval of time and are presented in Figure 3.16 (c) for the one taken at the growth

day and in Figure 3.16 (d) for the one 5 months old film. The image obtained at the day of the deposition presents a flat morphology, as expected for the conditions of deposition. On the other hand, after 5 months, the film is homogeneously covered by small particles that increase significantly the roughness of the film. Since the composition of the surface is unaltered with the time, these particles probably arise from the atmospheric carbon contamination. This deterioration seems to affect mainly the most outer part of the films and while it does not influence macroscopic measurements it can have a great impact in surface based techniques as the C-AFM making them less reproducible. This point will be discussed with more detail in the Chapter 5.

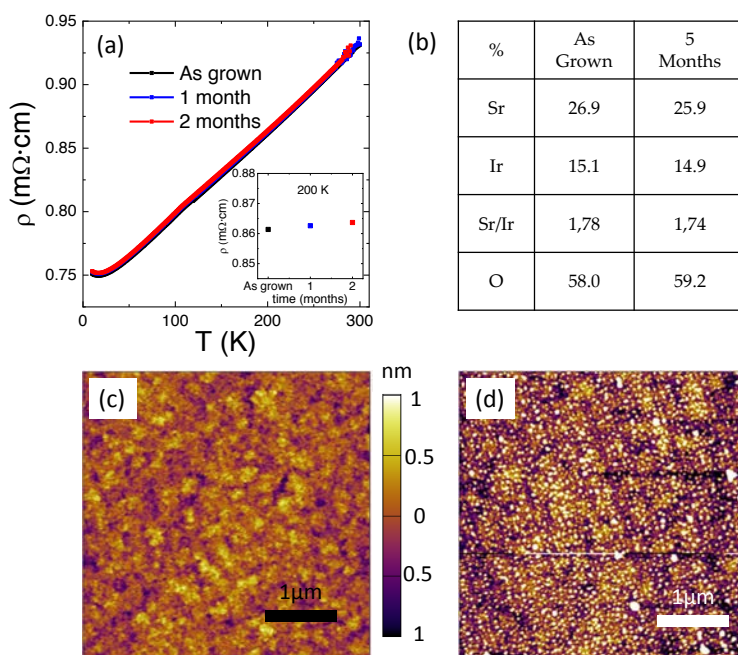


FIGURE 3.16: (a) Comparison of the $\rho(T)$ curves of the same film through the time. After few months the resistivity was only increased a $\sim 0.3\%$ keeping the same behavior, which indicates an absence of aging in the inner part of the film. Inset: resistivity of the film with the time at 200 K. Here it can be observed more accurately the slightly increase of the resistivity with time. (b) XPS measurements just after the deposition and 5 months later. No clear variations in the surface composition can be appreciated. (c) And (d) present the topography of a film the day of the deposition and 5 months later. After 5 months of storage the film gets totally covered by small particles.

3.3 Kinetics driven surface nanostructures in SrIrO₃ films

The ability to fabricate regular patterns for large areas is nowadays of a great interest from a technological point of view. The creation of those patterns can be achieved either by lithography and nanofabrication methods in what is known as the top-down approach or by self-assembling processes in the bottom-up approach. Although they are not yet used extensively for electronic applications, the self-assembled processes possess the potential to overcome the limits of the top-down approach creating smaller nanostructures more efficiently. In this context, transition metal oxides have proved to be an excellent playground to form arrays of structures. The combination of these capabilities with their wide range of magnetic and electronic properties provides oxides of a promising technological potential. Although the band structure and the electronic properties of 5d oxides as iridates may differ from their counterparts of 3d oxides, they are subject to similar surface processes. Therefore the study of their surface morphology can be comparable with other more studied oxides as manganites [70] [71].

The simplest model to describe the growth mechanisms rely on the thermodynamics. In this model the differences between the free surface energies of the substrate/vacuum, the film/substrate and the film/vacuum interfaces govern the mode of growth. According to these energies 2 possibilities of growth mechanisms can take place. Those are the Frank-van der Merwe mechanism, where the resultant film is flat due to a layer by layer growth (2D), and the Volmer-Weber growth that generate 3D separated islands on the substrate. In the middle way, the Stranski–Krastanov growth mode combines an initial 2D with a later 3D growth. This mixed growth model arises from an initial layer by layer mechanism that is tuned due to the superficial structures, which relax the elastic energy accumulated in the film due to the strain effect of the epitaxial growth. In some cases the thermodynamic approach does not predict the experimental depositions and kinetics effects must be taken into consideration. In these cases factors such as the diffusion of the adatoms in the surface can tune the final morphology of the films [72].

Figure 3.17 shows the clear variations of morphology that can be induced in SrIrO₃ films on STO (001) substrate by adjusting some conditions of the deposition as the power of the RF source or the oxygen pressure of the chamber during the deposition. At 6 mTorr of PO₂ the perovskite SrIrO₃ tend to grow in elongated islands. However, as the oxygen pressure is increased to 20 mTorr, the islands start to assemble between them creating an

array of deep holes. If the PO₂ is further increased to 60mTorr, the holes are reduced both laterally in the plane of the film and also in depth. Finally, if the deposition is carried out at 140 mTorr, the holes disappear completely and only a flat film remains. It is therefore clear that the system goes from a 3D growth mechanism at low pressures to a 2D growth mechanism at high ones. In the same Figure it can be observed that the power of the RF source has a significant influence on the morphology. In the case of the SrIrO₃ films grown at 140 mTorr an increase of the RF power induces the apparition of small elongated holes while a decrease of power has barely any influence on the topography. A similar trend can be observed in the case of the 60 mTorr films where a reduction of power can flatter the film eliminating the holes and an increase of it extend the holes and make them deeper. Therefore the film can be tuned from a 3D to a 2D growth by increasing the oxygen pressure or by reducing the RF power at the deposition.

The right inset of Figure 3.17 depicts the changes in the rms as the PO₂ increases. The maximum value of the rms is given at 20mTorr when the holes are deeper and more extended. As the holes are reduced (60mTorr) and disappear (140 mTorr) the rms experience a great downturn. The left inset of the same Figure shows the changes in the rms of the films grown with different RF power. It is obvious that the appearance (disappearance) of the holes cause an increase (decrease) of the rms value when the RF power increases (decreases). Moreover the increase of the power to 40W in the 60 mTorr films extends and makes the holes deeper which can be tracked by a clear increase of the rms value.

The mechanisms of growth that control the morphology and other properties of oxides films are not trivial and different parameters can influence the final features of the films. According to the stoichiometry studies carried out in the section 1 of this Chapter, thermodynamic conditions play a secondary role in the deposition of iridate films by sputtering. Therefore it is not expected that the thermodynamic mechanisms are the responsible for the observed variations in the morphology of the films. It has been observed that kinetics have an important impact in the deposition. These kinetic mechanisms depend mainly in the diffusion of adatoms in the surface and its combination with the morphology defects. In other oxides, the increase of the temperature, and thus the mobility of the adatoms, has been the key factor to tune the morphology of the film [70]. Nevertheless, the effect of the changes in the oxygen pressure or the power of the RF on the motilities of the adatoms are not so studied in the literature.

From the films shown in Figure 3.17 it is of an especial interest the one grown at 60 mTorr and 20 W. The topography of the same is depicted in a larger area in Figure 3.18. In both AFM (Figure 3.18 (a)) and SEM (Figure

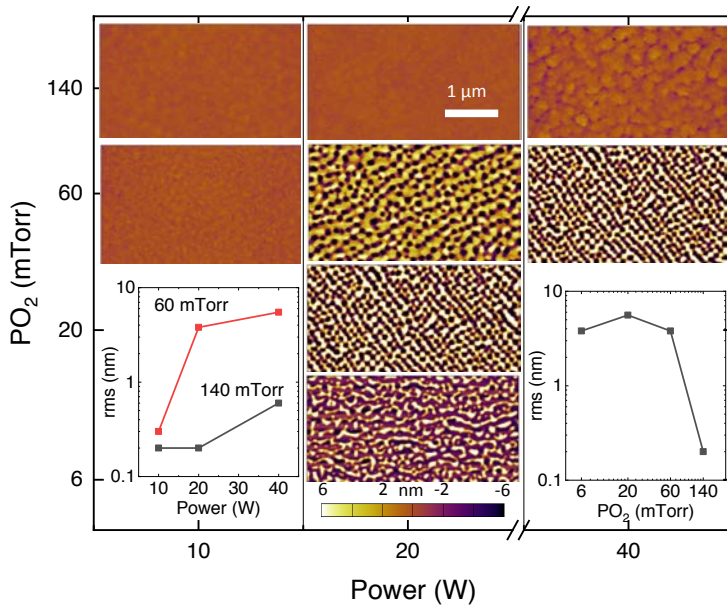


FIGURE 3.17: Series of $n=\infty$ films grown at 900°C and in a full oxygen atmosphere. The films are deposited at different pressures and different RF Powers. Lower pressures and higher powers favor 3D growth while high pressures and low powers shift the mechanism into a 2D one. In the intermediate cases arrays of holes are assembled. Inset left: variation of the rms with the RF source power. Inset right: variation of the rms with the pressure.

3.18 (b)) images regular line patterns parallel to the $[110]$ direction can be visualized in large extensions. The structure of this Nanostructured (NS) film has also been studied by means of XRD in Figure 3.18 (c) and (d). Figure 3.18 (c) depicts the θ - 2θ measurement of the patterned film. The out of plane parameter obtained from this measurement is 4.051 \AA , which is a very similar value to the 4.056 \AA obtained for the flat films. Moreover the RSM of the (-103) reflection presented in Figure 3.18 (d) shows that the film is fully strained as well.

These holes patterns have been observed also in manganites where the holes tend to grow along the steps of the underlying substrates. This behavior has been attributed to the energetic extra barrier for the adatoms to jump across the substrate terraces (Ehrlich-Schwoebel barrier) [70] [71].

In the present case a similar behavior is observed. Figures 3.19 (a) and (b) present the topography images of the underlying STO substrate before the deposition and the final SrIrO_3 film respectively. The terraces and the

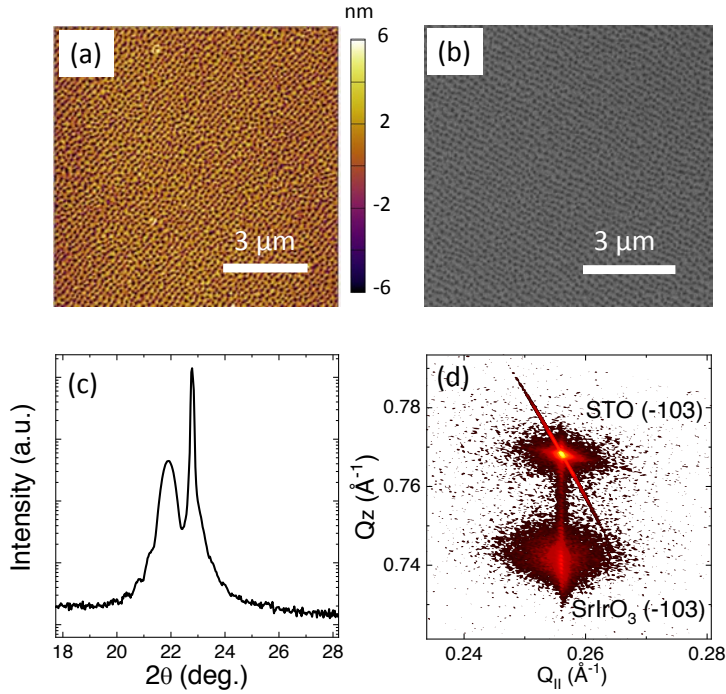


FIGURE 3.18: (a) AFM tapping image of a $10 \times 10 \mu\text{m}^2$ area. (b) Secondary electrons SEM image of a similar area. In both images the wide extension of the hole patterning can be observed. (c) θ - 2θ scan of the (002) peak of the STO substrate and the SrIrO₃ film. (d) RSM measurement of the (-103) peaks of the film and the substrate. The map indicates the fully strained nature of the film.

lines holes seem indeed growing in the same direction and with a similar spacing between lines. Nevertheless, to ensure this correspondence both images were analyzed with the autocorrelation function. Figures 3.19 (c) and (d) depict the autocorrelation function (C) of the Figures 3.19 (a) and (b) respectively. This function correlates an image with itself and is defined as:

$$C(\mathbf{r}) = \langle [z(\mathbf{r} + \mathbf{r}_0) - \langle z \rangle] \cdot [z(\mathbf{r}_0) - \langle z \rangle] \rangle \quad (3.4)$$

Where C is the value of the correlation function at a certain displacement vector \mathbf{r} , $z(\mathbf{r}_0)$ is the height of the image at a certain point, $z(\mathbf{r}_0 + \mathbf{r})$ the height of the image at the same point (\mathbf{r}_0) plus a certain displacement vector (\mathbf{r}), $\langle z \rangle$ is the average height of the image and $\langle \dots \rangle$ represents the average over all the possible values. This equation can be understood as the comparison between every point of the original image (\mathbf{r}_0) with the same image when is displaced by a vector \mathbf{r} .

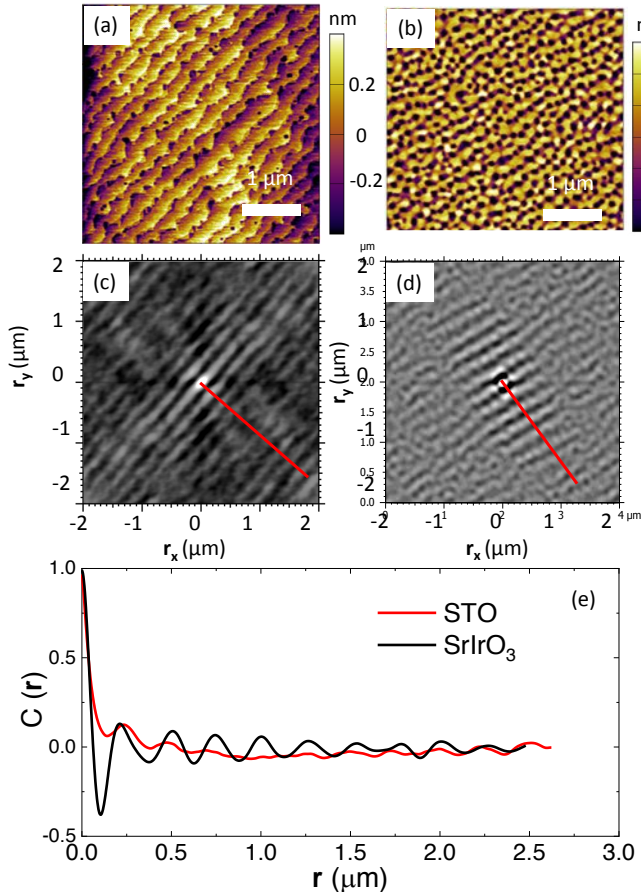


FIGURE 3.19: Topographic measurements of a NS film grown at 60 mTorr and 20 W and its substrate. (a) $4 \times 4 \mu\text{m}^2$ AFM tapping image of the STO substrate. (b) $4 \times 4 \mu\text{m}^2$ AFM tapping image of the SrIrO₃ patterned film. (c) and (d) autocorrelation function images of the AFM images (a) and (b) respectively. (e) Profiles of the autocorrelation images (c) and (d) taken from the center of the image and perpendicular to the direction of the maxima lines (marked in red).

In an image with randomly distributed heights, the value of the correlation value will be maximum at the center ($r=0$), when the image will be correlated with itself. Then C will decrease rapidly to 0 since the average of the correlation between different points will be close to the average of the heights. On the other hand if the image has a certain pattern of heights, C will replicate a maximum every time the pattern replicates with itself, even at $r \neq 0$, creating an oscillating pattern. Figures 3.19 (c) and (d) show clearly a pattern of maxima and minima in the diagonal of the images. These oscillations are caused by the terraces in the case of the substrate and by the

holes lines in the case of the SrIrO₃ film. In order to assess a clear relationship between the film pattern and the underlying substrate, two sections starting at the center of the image and perpendicular to the maxima lines (marked in red) have been obtained and their profiles can be observed in Figure 3.19 (e). The depicted lines show a clearly match of the oscillations between the film and the substrate, even at large distances, which indicates a long order network of holes and a proved correlation between the holes and the terraces.

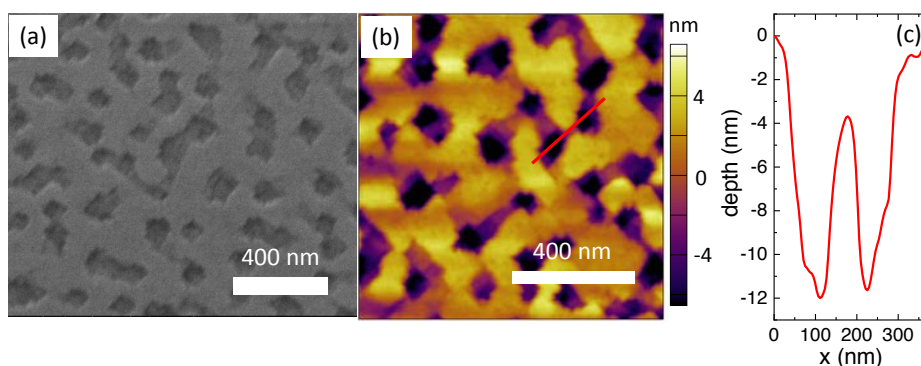


FIGURE 3.20: Topographic measurements of a film grown at 900°C and 60 mTorr with an “in situ” annealing of 900°C at 370Torr during 1h. (a) Secondary electrons SEM image. (b) AFM tapping measurement. In both measurements the polyhedral shape of the holes can be observed. (c) Profile of the two holes marked with a red line in (b) showing a mean depth of the hole comprised between 10 and 12 nm.

If an “in situ” annealing at 900°C and 370 Torr in an Oxygen atmosphere is implemented after the deposition of the film, the shape of the holes can be modified. Figure 3.20 shows the topography of the annealed film by a SEM (a) and an AFM images (b). In both Figures the holes can be observed but this time, instead of being round shaped, they adopt a polyhedral shape. The depth of these holes varies from 10 to 12 nm, which can be appreciated in Figure 3.20 (c) where a profile of two holes of the previous image is depicted. It is worth noting that the edges of the holes are oriented in the [110] and [-110] directions of the substrate. This could be induced by the increase of mobility of the atoms of the film during the annealing time. This extra mobility would reorganize the surface atoms and expose the plane faces with lowest surface energy inside the holes or to minimize the strain of the film [71]. Further studies using TEM images would be required to identify the planes exposed and determine the cause that favors them.

3.4 Deposition of Platinum Nanoparticles

In other studies performed with oxides it has been observed the preference of nanoparticles of noble metals to grow on the pits (holes) of the oxide films [71]. These pits can act therefore as a template to create patterns of nanoparticles (NP). With the aim of checking if this behavior can also be replicated on SrIrO₃ NS films, Platinum NP were grown by “in situ” sputtering deposition on SrIrO₃ thin films, both on flat films and on films with the holes pattern. This deposition was performed just after the n=∞ phase deposition at 900°C but with an Ar atmosphere of 50mTorr and using a DC source at 20 W.

Figures 3.21 (a) and (b) depict the SEM images of the NS films and the Pt NP deposited on the top. It can be clearly observed that the particles are distributed uniformly over the iridate surface and do not have any special preference for growing inside the holes. Similar to this, the Pt NPs are distributed homogeneously on a flat SrIrO₃ film as it can be visualized in Figure 3.21 (c). Although the NPs are distributed all over the surface of the films it is worth noting that they are not randomly oriented. A closer look to Figure 3.21 (a) reveals that larger NPs follow two preferential directions, which are perpendicular to each other. In order to study more deeply the possible orientation of the NPs, Pole Figures of both types of films, NS and flat, were measured. The results are depicted in the table of Figure 3.21 (d). The measurements were performed with an area detector (GADDS) at $2\theta=32^\circ$ and $\chi=45^\circ$ and rotating along the whole ϕ range (0-360°), this way the scan was centered at the (101) peak of the STO. Pole Figures show 3 different peaks that are repeated every 90° in ϕ which is indicative of the cubic (or quasi-cubic) structure of the STO substrate, the SrIrO₃ epitaxial film and the Pt crystals.

These reflections can be identified according their position in 2θ . The first peak appears at $2\theta=32.23^\circ$ and $\chi=45^\circ$ and corresponds to the (101) planes of the STO substrate and the SrIrO₃ film. These reflections provide a base to understand the relative orientation of the Pt NP to the films. The second reflection is located at $2\theta=46.65^\circ$, $\chi=44^\circ$ and at the same positions of the SIO/STO (101) reflections in ϕ . This peak can only be attributed to the (200) plane of the Pt NPs due to its position in 2θ . Its position in χ indicates that the Pt cube is deposited with the plane (101) facing the (001) plane of the film which is parallel to the surface. The third peak appears at $2\theta= 40.13^\circ$, at a similar position in ϕ as the first and the third one and in a wide range of χ (33°-54°). This last peak corresponds to the (111) reflection of the Pt NPs due to its position in 2θ . It is important to note that the value in 2θ is similar to the planes (111) of the STO and the SrIrO₃, nevertheless

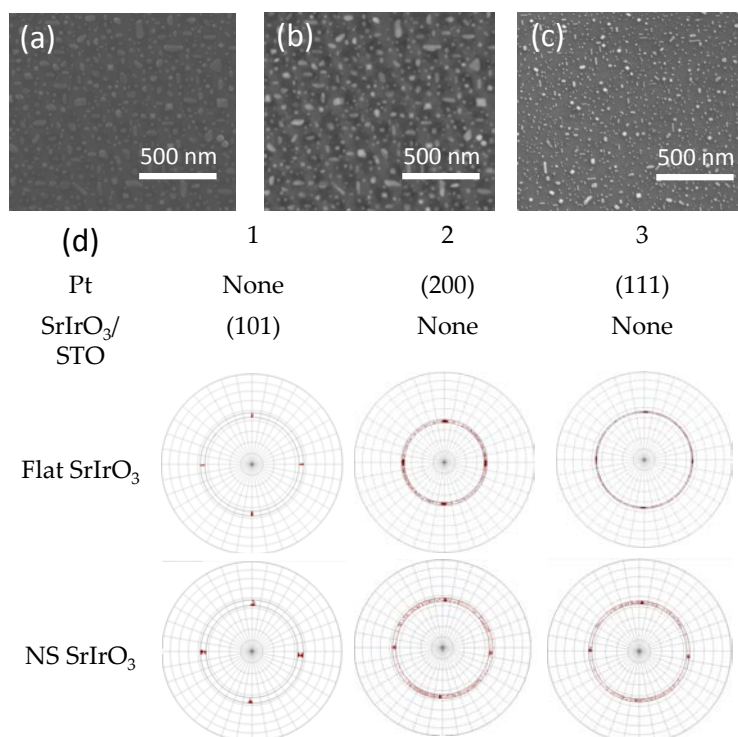


FIGURE 3.21: Characterization of the SrIrO₃ films with Pt NP. (a) Secondary electron SEM image of the NP over the NS films. (b) Backscattered electron SEM image of the NPs on the NS SrIrO₃ film. (c) Secondary electron SEM image of the Pt NPs on a SrIrO₃ flat surface. (d) Table of the different peaks of the Pt NP, the SrIrO₃ film and the STO substrate and their respective Pole Figures.

the wide range in χ indicates that the orientation towards the surface is not well defined. The apparition of such planes in this range of χ would be incompatible with the epitaxial relation of the substrate and the film indicated by the RSM and the θ - 2θ scans in the section 2 and therefore they can only be attributed to the Pt NPs.

According to the data there are two possible orientations of the Pt NP on the SrIrO₃ film. On one hand the second peak indicates the presence of a population of NP with the plane (101) parallel to the surface of the film, which corresponds to the plane (001). The reflection of these NPs appear at the same values of ϕ as the (101) planes of the substrate indicating that the direction [100] of the NPs is parallel to the [100] direction of the STO (and the SrIrO₃). On the other hand, the third peak reveals that the other

orientation of the NPs, in which the (001) plane of the Pt is parallel to the (001) plane of the substrate. Nevertheless this growth does not follow an epitaxial trend with the film. These (111) Pt peaks appear at the same ϕ from the (101) planes of the film (and substrate), therefore the [100] direction in these Pt crystals correspond to the [110] direction of the STO.

It is worth noting that both pole figures present similar results with the same two orientations of Pt NPs. Therefore it can be concluded that the particles deposited on the holes do not have any special orientation and follow the same trends as the ones deposited on flat surfaces.

Besides its orientation study, Pt NPs have been used in this thesis to improve the current C-AFM maps, as it will be presented in the Chapter 5.

3.5 Sr_2IrO_4 thin film growth

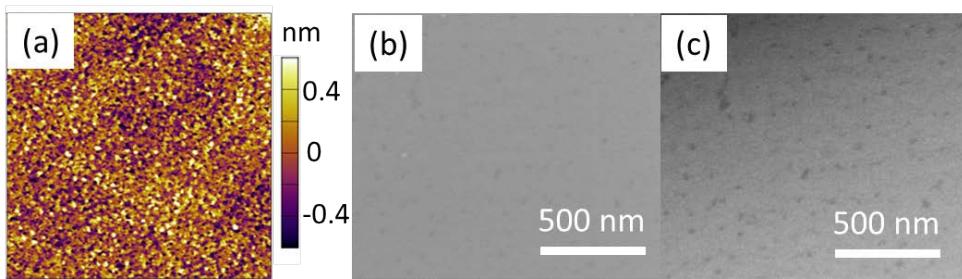


FIGURE 3.22: Morphology characterization of the $n=1$ films. (a) AFM tapping measurement showing a flat surface of $\text{rms}= 0.26$ nm. (b) Secondary electron SEM image. (c) Backscattered electron SEM image.

In this chapter, it has been proved that the $n=\infty$ phase has a preferential growth in the Sputtering deposition, even if the experimental conditions force the film to accommodate variations in the stoichiometry. In order to compare the electric and resistive switching properties of the $n=\infty$ phase and the $n=1$ phase, films of $n=1$ phase were grown by PLD. The optimization of the growth for the $n=1$ phase was carried out previously by Dr. Araceli Gutierrez in the ICN2 nanomaterials growth unit facilities. These films were grown on STO substrates at 850°C with a pure atmosphere of oxygen at 70 mTorr. The laser employed in these depositions was a KrF excimer laser at a frequency of 1Hz and a laser fluence of 1.25 J/cm².

As in the case of the $n=\infty$ phase, morphology and structural properties were evaluated with the aim of assess the quality of the films.

Figure 3.22 depicts the topographic measurements performed on the $n=1$ films. Both AFM (Figure 3.22 (a)) and SEM images (Figure 3.22 (b)) show a flat surface with an rms below 0.3 nm. Moreover the lack of contrast in the Backscattered electrons image indicates a homogeneous composition of the film at the surface.

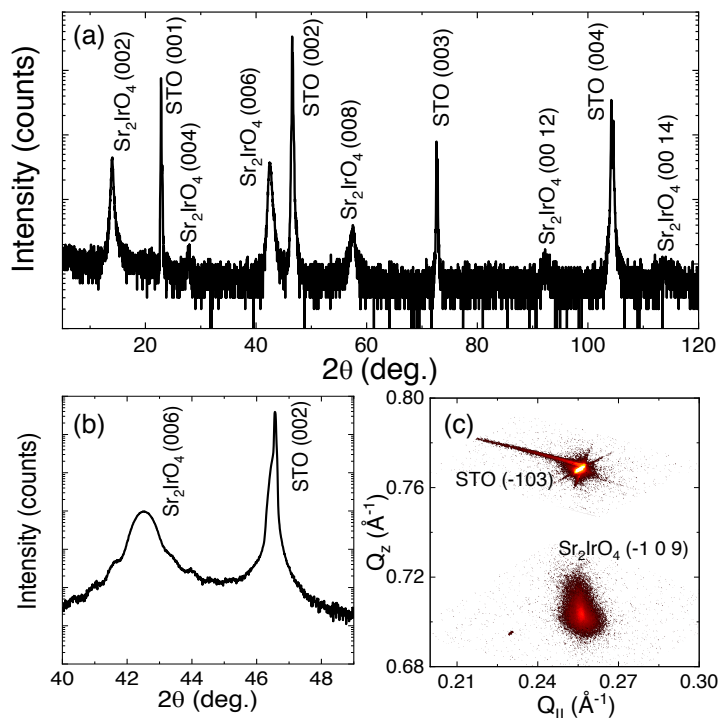


FIGURE 3.23: X-Ray diffraction measurements of the $n=1$ /STO films. (a) Complete θ - 2θ scan of a 16 nm film. (b) High resolution 16 nm (c) RSM of the (-109) reflection of a 38 nm Sr_2IrO_4 film.

The structural properties of the films have been evaluated by means of X-Ray diffraction. Figure 3.23 (a) depicts a complete θ - 2θ diffractogram of the film where, apart from the substrate peaks, only the (0 0 2l) family of planes is present. The lack of additional peaks suggests a good purity of the $n=1$ phase and the fact that only the (0 0 2l) peaks are present is indicative that the film has grown epitaxially on the (001) STO substrates. The out of plane parameter can be calculated more precisely with a High Resolution scan in the same θ - 2θ geometry (Figure 3.23 (b)). The peak of the film is shifted to higher values due to the compression of the out of plane parameter of the film from the relaxed theoretical value (12.92 \AA [57]) to the

measured one (12.78 Å). Similar to the case of the SrIrO₃ films, this out of plane compression is the direct consequence of the in plane tensile stress of the film imposed by the STO substrate.

The fully strained nature of the films is confirmed in the RSM depicted in the Figure 3.23 (c). This RSM shows the (-103) peak of the STO and the (-109) peak of the n=1 film. Both peaks are situated in the same Q_{II} reciprocal space vector, which corresponds to the lattice parameter of the STO (3.905 Å). Therefore it can be concluded that the in plane parameter of the n=1 film (3.89 Å) is forced to expand to growth epitaxially on the (001) STO substrates.

Chapter 4

Electric properties of Strontium Iridates

4.1 Transport properties of flat SrIrO₃ films

As it was explained in Chapter 2, the interplay interaction between the comparable contributions of Spin Orbit Coupling (SOC), crystal field and electron correlations in the perovskite SrIrO₃ generate a semimetallic electronic state. It is thus natural to investigate the electric transport properties of the optimized flat films. Figure 4.1 (a) shows the results for a 26 nm thick film measured in a standard four probe configuration. The resistivity of the sample follows a semimetallic behavior, i.e., a monotonous decrease with lowering temperature, in the whole measured range of temperatures (10-300K). Nevertheless, below 25K the resistivity exhibit a change of tendency when further decreasing the temperature, suggesting a transition to insulator at lower temperatures. Therefore two different regimes can be identified: a semimetallic one ($d\rho/dT > 0$) and an insulating one ($d\rho/dT < 0$) separated by a transition which can be defined as $T_{MIT} = T_{Max} (d\rho/dT < 0)$.

These dependencies in the resistivity curves are similar to the ones reported in the bibliography for equivalent thickness and substrate as it can be observed in Figure 4.1 (b). Although there is some variability in the absolute values of the resistivity and the temperature where resistivity minimum occurs, all of them follow the same tendencies. Nevertheless, it is worth noting that films grown by PLD are systematically more resistive and with a higher T_{MIT} than those grown by the Sputtering technique.

In thin films, it has been previously reported that this semimetallic behavior can be modified by small distortions including epitaxial strain [68] [73] or the reduction of film thickness [11] [69]. These external stimuli produce modifications in the band structure of the $n=\infty$ films leading to the apparition of Metal-Insulator Transitions (MITs). As it has been pointed

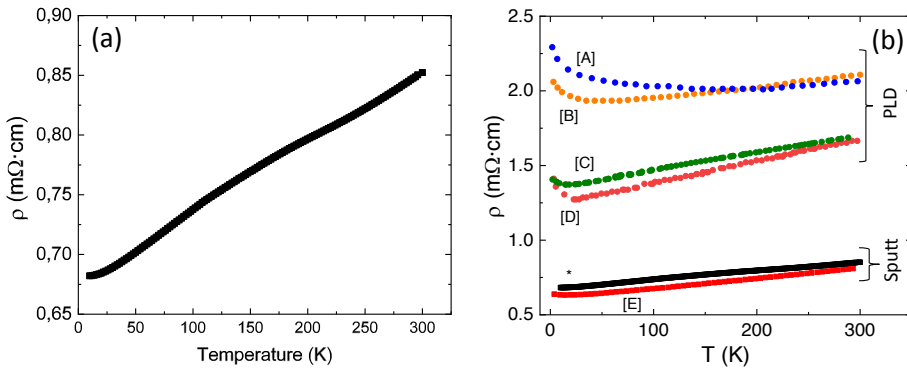


FIGURE 4.1: (a) Temperature dependence of resistivity in a 26 nm film of $n=\infty$ phase. Two behaviors can be distinguished: a semimetallic region in most of the measured temperature range and a progressive upturn at the lowest temperatures. (b) Comparison between the resistivity of the present SrIrO₃ film (*, black data points) and those reported in the bibliography ([A]-[73], [B]-[11], [C]-[74], [D]-[68] and [E]-[45]). Although the characteristics of the curves are similar, the films grown by PLD are clearly more resistive than those grown by Sputtering.

out in Chapter 2, the proximity of the SrIrO₃ films to these MITs makes them excellent candidates for testing Resistive Switching (RS) properties. Nevertheless, to fully understand the RS behavior on iridate films (see next chapter) it is first necessary to study these MITs and how the electronic properties of the $n=\infty$ films are altered by them.

4.1.1 Metal Insulator Transition in the SrIrO₃ films

In the present Thesis, we have focused on the MIT triggered by a reduction of thickness. With the aim of exploring this transition, a series of films with different thicknesses comprised between 2 nm and 26 nm were grown on STO substrates. This series were deposited with the same optimized conditions for obtaining flat iridate films that have been deeply studied in Chapter 3. The thickness of the films was analysed by XRR in the thicker and the rate was extrapolated to thinner ones to obtain the nominal thicknesses using the time of deposition. All the grown films exhibited flat surfaces with rms values below 0.25 nm and without any visible segregations, as it can be appreciated in the AFM topography images depicted in Figure 4.2. Furthermore, in the case of the thinnest film of 2 nm (Figure 4.2 (f)) a step-like morphology can be noticed. This feature is the product of the replication by the film of the atomic terraces of the underlying STO substrate.

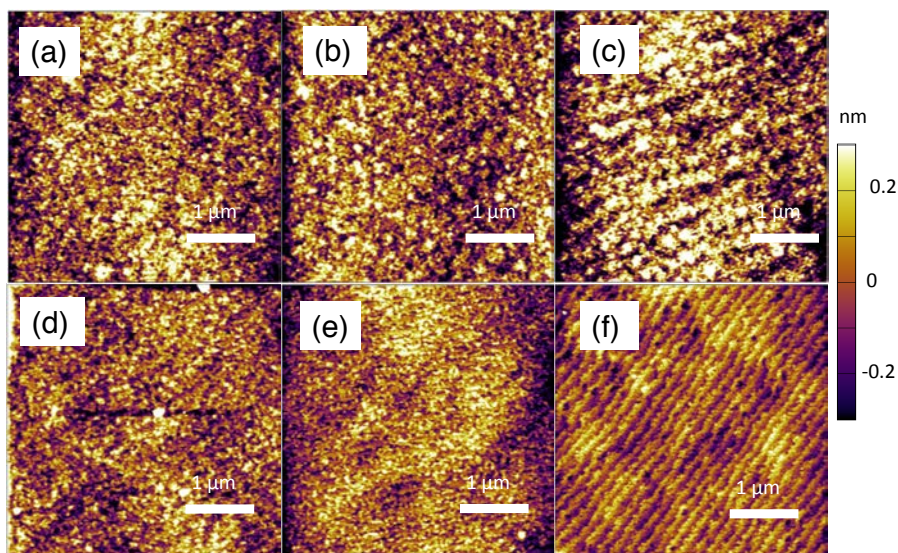


FIGURE 4.2: $4 \times 4 \mu\text{m}^2$ AFM tapping images of the SrIrO₃ films with thicknesses of (a) 26, (b) 15, (c) 10, (d) 5, (e) 3 and (f) 2 nm. All the films present an rms below 0.25 nm without any visible deformations or segregations, which are indicative of their flat nature. Moreover in the case of the thinnest film (f) the steps of the underlying STO substrate are replicated.

The structural features of the series were characterized by θ - 2θ scans around the (002) peaks, which are depicted in Figure 4.3 (a). As the thickness of the films is reduced, the intensity of the film peak is diminished and broadened but it roughly remains at the same 2θ position. While the two former effects are common features caused by the reduction of material thickness [75], the latter indicates that the out of plane parameter of the films remain unchanged within our experimental uncertainty by the reduction of thickness. This result is presented in Figure 4.3 (b) where the out-of-plane parameter (c) was obtained after fitting the measurements presented in Figure 4.3 (a). According to these data no dependency with thickness can be appreciated in c , which is placed around 4.05 \AA . Now, we should remind that in preceding Chapter 3 we have shown that the thicker films are fully strained with the STO substrates. It is thus sound to assume that thinner films also share this characteristic. As a consequence, we may consider in the following that as out-of-plane parameter remains unchanged all the films in the thickness series present similar degrees of distortion and, the epitaxial growth and the crystal lattice of the films should be comparable between them.

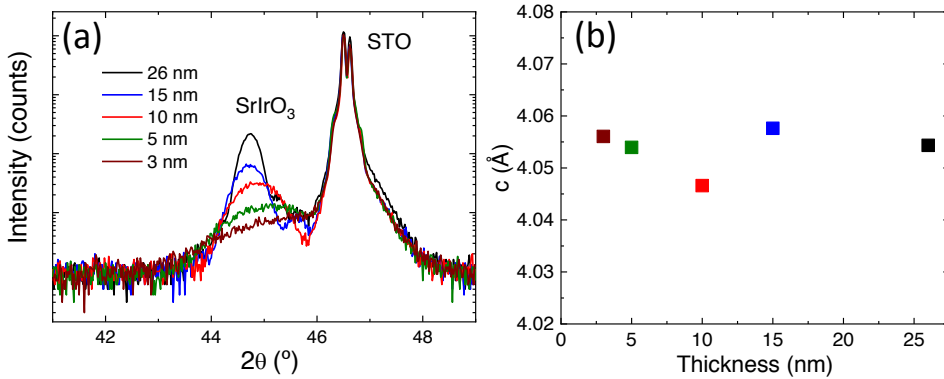


FIGURE 4.3: (a) θ - 2θ scans of the (002) peak of the SrIrO₃ films with different thicknesses and the STO substrate. The position of both peaks remains unchanged and only the film peaks are decreased and broadened due to the reduction of the thickness. (b) Out of plane parameter in the SrIrO₃ films obtained by adjusting the measurements in (a). The absence of a clear tendency indicates that all the films possess similar crystal lattices.

Therefore, it is expected that both the morphology of the films and the deformations of the lattice by the epitaxial strain do not play any role within this series of films.

Figure 4.4 depicts the electric four probe measurements performed in lithographed paths (described in the Appendix A) of the studied sample series. Figure 4.4 (a) presents the dependence with the temperature of the sheet resistance ($R_{sheet} = \rho/t$, being t the thickness) of the films in the range comprised between 300 K and 10 K. Two different behaviors are evidenced by the results in Figure 4.4 (a). First, films with thickness above 3 nm follow a (semi)metallic behavior in most of the studied range and only experiment an upturn at low temperatures. On the other hand, the thinnest film of 2 nm presents an insulating behavior (i.e., $d\rho/dT < 0$) in the whole measured range. Thus, the SrIrO₃ system undergoes an abrupt MIT when the thickness is reduced from 3 nm to 2 nm. Therefore, the MIT and the insulating regime can be observed by reducing the thickness or lowering the temperature in thin semimetallic films. Besides the change in the dependency with temperature, the absolute value of the resistivity of the system is also deeply altered by this abrupt transition with thickness. Figure 4.4 (b) depicts the thickness dependence of the film resistivity at 300K. The resistivity is almost constant within the semimetallic range (3-26 nm) but experiences a noticeable increase when the transition is crossed at the 2 nm film reflecting the abrupt character of the MIT. We should note that similar transitions

have been reported in the bibliography for similar values of the thickness [11] [69] [76].

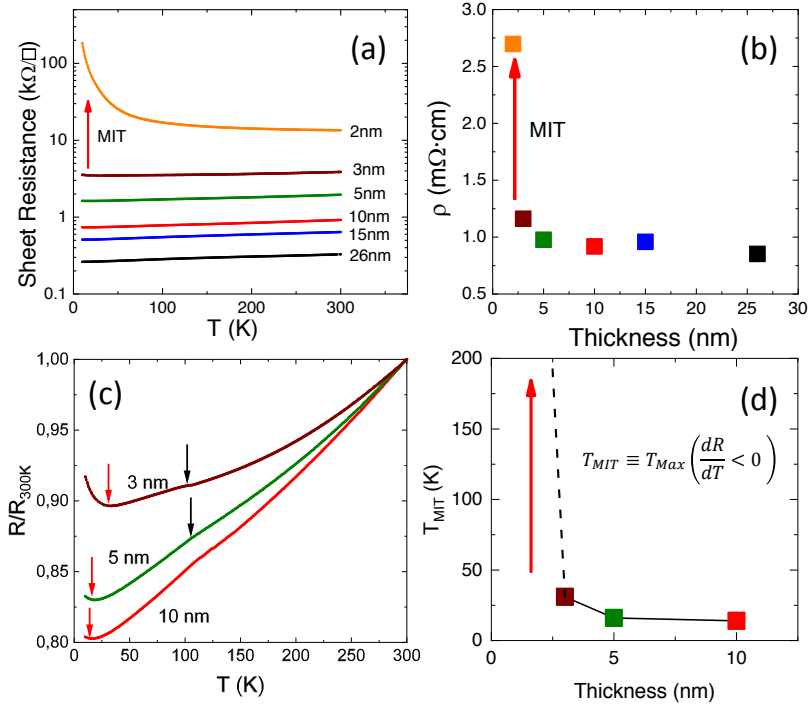


FIGURE 4.4: Metal Insulator Transition of the SrIrO₃ films triggered by the reduction of thickness. (a) Sheet resistance dependence with temperature in the series of films. The films between 3 and 26 nm show a semimetallic behavior in most of the measured range while the 2 nm film is insulating in the whole range indicating a MIT triggered by the reduction of thickness. (b) Resistivity at 300 K in the different films. The abrupt increment of resistivity between 3 and 2 nm is noticeably and is also indicative of the presence of a MIT. (c) Relative resistance of the films close to the MIT. The characteristics of both the insulating and semimetallic regimes can be better appreciated here. (d) Evolution of the T_{MIT} with the thickness. As the thickness is approaching the MIT the T_{MIT} increases abruptly.

Figure 4.4 (c) shows the resistance normalized to the value at 300K for the films between 3 nm and 10 nm, i.e., approaching the MIT transition. In this graph we may easily compare small variations of the resistivity behavior both in the semimetallic regime as well as in the insulating one:

- On one hand, in the semimetallic regime, it can be appreciated that the resistance dependence with temperature changes as the thickness is reduced, in particular, the slope of the resistivity is reduced with

reducing thickness. It is also noticeable the presence of a small kink around 100 K (marked by black arrows) which may be attributed to a structural transition in the STO substrate and it will be explained below.

- On the other hand, we may notice that the temperature at which the resistivity presents a minimum T_{MIT} (red arrows), marking the onset of the insulating regime, increases as the film thickness is reduced. Thus, the insulating region is broadened to higher temperatures shifting the transition temperature.

The overall evolution towards an insulating state by thickness reduction is monitored in Figure 4.4 (d) where the thickness dependence of T_{MIT} is depicted. Although the increment of T_{MIT} is progressive as the thickness of the film approximates the transition, the subsequent evolution from 3 to 2 nm is sharply defined indicating an abrupt apparition of the transition.

To improve the understanding of the films and get insights about the nature of the MIT, the described characteristics of both regimes were studied in more depth and are presented in the following subsections.

Semimetallic region

First, we will analyze the semimetallic region of iridate films with thickness above 3 nm. Usually, in correlated metals, temperature dependence of resistivity is fitted to a power law where the exponent gives information about the importance of the main scattering mechanisms as, for example, electron-electron or electron-phonon. For this analysis, an extended range of fitting temperatures is needed to soundly establish the extracted parameters. A quick inspection of the results presented in Figure 4.4 (c) evidences the main difficulty to perform such analysis in our films. Indeed, as pointed out before, within the semimetallic region of the SrIrO_3 films on STO a small kink can be noticed around 100K. In order to ascertain the origin of this anomaly, the derivative of the resistivity with the temperature in the 15 nm film has been calculated and plotted in Figure 4.5 (a). In this Figure it can be observed that, before the derivative starts to decrease (due to the MIT at low temperatures) there is an abrupt change of tendency around ≈ 105 K which splits the semimetallic region in two parts. It is known that at 105K the STO experiences a structural transition from a cubic to tetragonal phase. During this transition, the lattice parameters of STO are subsequently modified [77] [78] [79]. Since the iridate films are grown in an epitaxial fully strained nature (Chapter 3), it is reasonable to expect that the in-plane deformations of STO could be also replicated by the film lattice parameters

and, as a consequence be the responsible for the observed kink in the resistivity curves, being clearer in the thinnest films. A similar analysis of this extrinsic anomaly has also been reported in other films grown by sputtering [45] and by PLD [74]. Further confirmation of this extrinsic origin of the resistivity kink, may be obtained by studying the transport properties of films grown onto different substrates. To this aim, the resistivity of an 11 nm SrIrO₃ film grown on a NGO substrate was studied. Figure 4.5 (b) depicts the derivative of the resistivity of this film with the temperature. Unlike the previous case, the derivative of the SrIrO₃/NGO film does not present any abrupt variation in the whole temperature range. This lack of anomalies in the films grown on NGO strongly suggest the extrinsic origin of the resistivity kink in films grown on STO and it does not represent an intrinsic resistivity feature of the SrIrO₃ films. Nevertheless, the present results demonstrate not only the relevance of the substrate in the transport properties of these films, but also their extreme sensitivity to small structural changes.

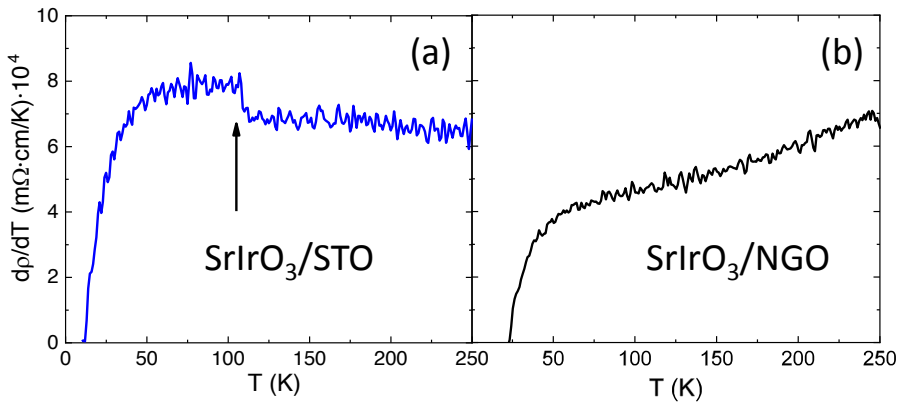


FIGURE 4.5: Temperature dependence of the resistivity derivative for SrIrO₃ films grown on (a) STO and (b) NGO substrates. A anomaly at 105 K can be appreciated only in the films grown on STO (black arrow). This variation has been related to a structural transition of the STO substrates.

As it has been commented before, the semimetallic region dependence on temperature changes as the thickness of the SrIrO₃ is reduced. To quantify these changes, the high temperature region of the resistivity curves has been assumed to follow an usual non-Fermi liquid behavior [11] [74] of the form:

$$\rho = \rho_0 + A \cdot T^\alpha \quad (4.1)$$

Where ρ_0 is the residual resistance at 0 K, A is a fitting prefactor and the exponent α accounts for the dependency of the resistivity on the temperature. This exponent contains information about the different mechanisms of scattering that affect the conductivity and their dependencies on the temperature. In order to avoid any contribution from the insulating regime and from the anomalies linked to the structural STO transition, the semimetallic region of the films was always analyzed in the range between 300 and 150 K. With this temperature range, different exponents α could lead to fittings of apparent similar quality and the best one is difficult to elucidate. Thus, for the analysis, we have followed the procedure proposed in the literature [80] where the resistivity ρ is linearly fitted against different T^α . The best fitting is then selected by choosing the exponent α that maximizes the correlation coefficient R^2 defined by:

$$R^2 = 1 - \frac{\sum_i(\rho_i - \rho_{calci})^2}{\sum_i(\rho_i - \bar{\rho})^2} \quad (4.2)$$

Where ρ_i are the adjusted collection of resistivity data, $\bar{\rho}$ is the average resistivity of this collection and ρ_{calci} is the theoretical resistivity according to the fit. The value of R^2 in a linear fitting indicates the exactitude of the match between the experimental data and the model being fitted. An exact match gives a maximum value of $R^2=1$, therefore, the closest value of R^2 to one implies the best agreement with the used α with the resistivity curve.

Figure 4.6 (a) and its inset provide an example of this procedure for the 10 nm film. In this case, the best fit is obtained for $\alpha=1.5$. Performing the same analysis in the whole series we obtain the evolution of α with the thickness, as depicted in Figure 4.6 (b). It can be appreciated that after an initial small decrease of α from 26 to 15 nm the exponent follows a clear growing tendency as the film approximates the transition. These changes are indicative of variations in the weight of the different scattering mechanisms. However, as said above, the identification of such mechanisms and their exact contributions represents a more complex problem to solve, which is out of the scope of this thesis. Nevertheless, it is worth to mention that the exponent may not only be determined by the scattering mechanisms and their relative strength but also by the degree of disorder. Recently, some models have predicted an increase of α with the disorder [81]. Moreover, several publications present results that are also in well agreement with this model in perovskite oxides as ruthenates [82] or nickellates [80]. Therefore we cannot disregard the possible role of disorder in the rise of α as thickness is decreased.

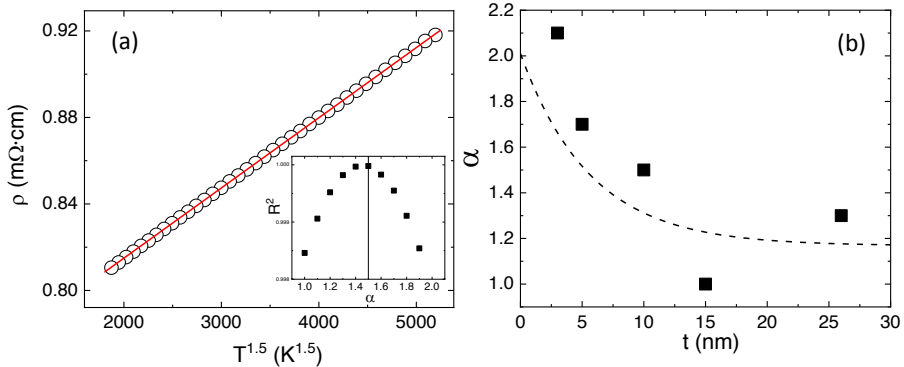


FIGURE 4.6: (a) Example of the linear fit in the 10 nm film. Inset. Optimization of the α value by studying the fits with the maximum R^2 . (b) Evolution of the α with the thickness of the film.

Insulating Region

Although the insulating regime can be observed in semimetallic films with thickness below 10 nm, a reliable analysis is only feasible for films under 3 nm where a wide enough range of temperatures is available. Figure 4.7 (a) shows the temperature dependence of the resistivity for the 3 nm film in the low temperature regime. Around the T_{MIT} (marked by a red arrow) the semimetallic regime transits to the insulating regime. Below T_{MIT} the conductivity (σ) can be nicely fitted by the expression 4.3, as depicted in Figure 4.7 (b):

$$\alpha \propto \ln(T) \quad (4.3)$$

This logarithmic dependence of the conductivity is usually associated to a weak localization regime in 2D systems. In this regime, the conductivity of a 2D material is reduced due to the interference of the electron backscattered waves. As explained in the Chapter 2 of this thesis, this decrease in the conductivity at low temperatures is produced by the increase of the disorder in a system and indicates the proximity to a MIT driven by disorder, commonly known as an Anderson MIT. This dependency is in well agreement with previous reported works, which have also found similar enhancements of the resistance due to disorder in the SrIrO₃ films at low temperatures [11] [45] [68] [69].

As it can be observed in Figure 4.8 (a), once the thickness is reduced from 3 nm to 2 nm the film undergoes abruptly an Anderson MIT and

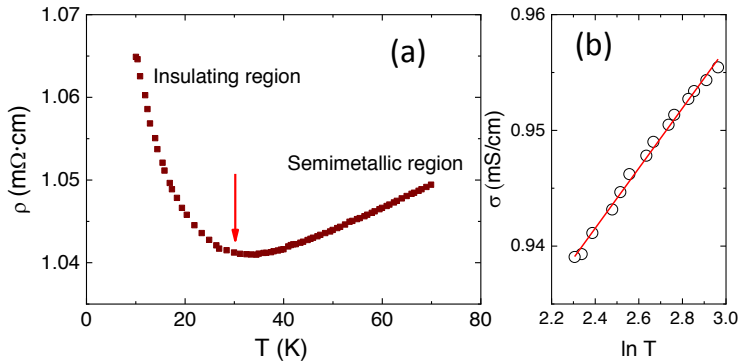


FIGURE 4.7: Analysis of the insulating part in the 3 nm film. (a) Resistivity at low temperatures showing the transition between regimes with a red arrow. (b) Conductivity dependence on the $\ln(T)$ plot, showing a good adjustment to the weak localization theory in 2D.

becomes insulating in the whole measured range, indicating a sudden increase of the disorder in the film. The black line that crosses the graph depicts the Mott-Ioffe-Regel (MIR) limit which is located at $\approx 26 \text{ k}\Omega/\square$ [11] [69]. This limit indicates the minimum mean free path of an electron before it is reduced below the lattice spacing, and, generally speaking it marks the change from weak localization to strong localization. We may observe that the resistivity of the 2 nm thick film crosses this limit at around 50 K. This may suggest that strong localization is only reached at low temperatures with disorder playing a key role in the evolution of the MIT. Similar results of strong localized behaviours in SrIrO_3 films have already been reported in the literature [11] [69].

The insulating behavior of the 2 nm film can be fitted in two different regions by different conduction mechanisms, as it is depicted in the inset of Figure 4.8 (a).

At low temperatures the measured resistivity cannot longer be described by the same mechanisms as in thicker films, i.e., weak localization. Instead, it fits very well with the typical expression for strong localized systems, i.e., Variable Range Hopping (VRH):

$$\rho(T) = \rho_0 \cdot e^{\left(\frac{T_0}{T}\right)^{\left(\frac{1}{1+d}\right)}} \quad (4.4)$$

Where T_0 is a characteristic temperature and d is the dimensionality of the system. In the present film, the linearized fit depicted in Figure 4.8 (b) is optimal considering a two dimensional system ($d=2$). This mechanism

of conduction implies that the electric carriers have to “hop” from atom to atom according to the energy of the state and the distance between atoms. The presence of such mechanism implies a strong localization of the carriers and it can be indicative of either Mott or Anderson insulators behavior. Therefore it further supports that the abrupt change of behavior when the thickness is reduced below 3 nm is driven by disorder as previously observed by other groups [11] [69].

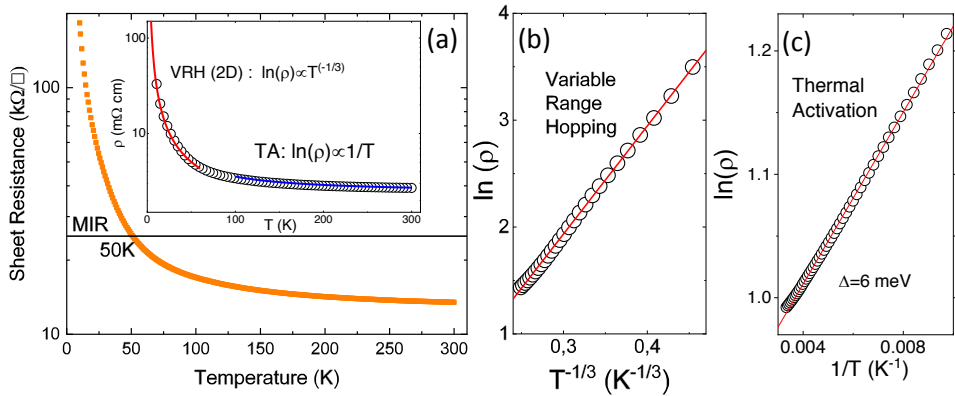


FIGURE 4.8: Resistivity measurements analysis of the 2 nm Anderson insulator film. (a) Temperature dependence of the sheet resistance. The black line represents the universal Mott-Ioffe-Regel limit ($\approx 26\text{K}\Omega$) which is crossed at $\approx 50\text{K}$ indicating a strong disordered state. (Inset). At low temperatures the resistivity can be fitted to a VRH model in 2D (red curve) while at high temperatures the experimental data fits with thermal activation dependence. (b curve). (b) Linearization of the thermal activation region. (c) Linearization of the VRH region. Red lines in (b) and (c) are the corresponding fits.

When temperature is increased, resistivity deviates from the VRH mechanism and above 50 K the it cannot explain the experimental data. In general, this is due to the fact that the VRH expression do not takes into account the possible temperature dependence of the energy of available states in the hopping probability. At higher temperatures (100K -300K) the resistivity can be simply described by a standard thermal activation mechanism following the usual Arrhenius equation:

$$\rho(T) = \rho_0 \cdot e\left(-\frac{\Delta}{k_B T}\right) \quad (4.5)$$

Where Δ is the activation energy and k_B is the Boltzmann constant. In Figure 4.8 (c) it can be appreciated how the linearization of the equation fits

perfectly with the experimental data at high temperatures. The resulting fit gives a $\Delta = 6$ meV which indicates that the energetic barrier is relatively weak in comparison with other reports [83]. This small value is the consequence of the disorder driven localized states and does not indicate the necessary presence of a gap.

Our transport results suggest that the main mechanism that drives the MIT in the SrIrO₃ seems to be the disorder. Nevertheless, we should remind that the role of electron correlation cannot be fully disregarded and it might contribute to the insulating state by the opening of a small gap in the vicinity of the Fermi level. This gap opening has been reported by some authors [46] and it is still under debate. In this scenario electron correlations act cooperatively with the disorder to bring the films into the observed insulating state.

4.1.2 Magnetotransport in SrIrO₃ films

To further confirm the disorder driven nature of the observed MIT when the thickness of the films is reduced, the magnetotransport of the films was evaluated near the T_{MIT} . As commented in the Chapter 2, the presence of a magnetic field affects directly the Weak localization phenomenon lowering its increase of resistivity. The addition of a magnetic field into a film breaks the time reversal symmetry between the forward and the backward path of the scattered electrons, and thus, it prevents the interference between the electron waves that cause the increment of resistivity. Therefore the presence of a magnetic field induces a negative magnetoresistance (MR) in weak disordered systems [24] [35]. In order to test the possible existence of this negative MR, the resistance of 2, 3 and 5 nm films were measured at low temperatures under a magnetic field comprised between -9 and 9 T. The results of the MR calculi (Appendix A) for each film are depicted in Figure 4.9 (a) corresponds to the results of MR in the 2 nm thin film. In this figure it can be observed that at 10 K the film has a clear negative symmetric MR that increases with the magnetic field and reaches a 10% at 9T. As the temperature is increased to 15 K and 25 K the negative tendency is maintained but the intensity of the MR is reduced reaching only 6 % and 3 % respectively at 9 T. In the inset of the same figure the MR at higher temperatures are depicted. At 50 K there is a sudden change of behavior and the MR is clearly positive and it increases with the field. Nevertheless, its magnitude is orders of magnitude weaker than the previous negative MR (0.1 % at 9 T). As the temperature is increased the positive MR is progressively reduced (75 K) until it cannot be longer detected (100 K).

A similar tendency can be observed in the 3 nm film (Figure 4.9 (b)) and in the 5 nm film (Figure 4.9 (c)) where the MR starts from negative values at the lowest temperatures to positive values at higher ones. In the case of the 3 nm film this transition occurs between 7.5 K and 10 K while it occurs between 5 K and 7.5 K for the 5 nm thick film. Two main observations should be noticed from these results. First, negative MR are always significantly higher than positive ones and second, the negative MR observed in the 2 nm film is more than an order of magnitude higher than for the 3 nm and 5 nm films. Although in these latter films the negative MR are still more intense than the positive ones, the measures below the transition are clearly weaker than the ones obtained in the insulating 2 nm film. Moreover, in the 3 nm film, it can be noticed that at 10 K the positive MR undergoes a softening at high fields, indicating that a positive and a negative contributions with different dependencies on the field are acting simultaneously on the film.

A global vision of these measurements can be appreciated in figure 4.9 (d) where the evolution of the MRs with the temperature is depicted in all the three samples at 9 T. In this figure it may be clearly observed that as film thickness is reduced there is an increase of the temperature at which the transition between the positive and the negative MR occurs. Moreover, it can be noticed that while positive MRs of the different films have comparable values ($\approx 0.1\%$) the magnitude of the negative MRs are higher as the thickness of the film is reduced. Both the magnitude increase of the negative MR and its transition from the positive trends seem to follow the same tendencies as the T_{MIT} . Therefore, it is reasonable to assume that the presence of negative MR is linked to the mechanisms controlling the insulating behavior of the film.

On the other hand, positive MR is usually associated to the classical (Lorentz) component which typically varies as B^2 and it strongly decreases at high temperatures. In our case, the positive MR with the higher magnitude in the three samples (50 K in the 2 nm film, 25 K in the 3 nm film and 10 K in the 5 nm film) seem to follow a linear dependence with magnetic field. Contrary to these measurements, most of the literature reports a positive quadratic dependency at high temperatures as expected from a classical Lorentz contribution [11] [73] [83]. Nevertheless, it is relevant to note that recently, some authors have reported a quasilinear positive MR that could be related to a topological transition of a SrIrO₃ Dirac node [84] [85].

A quantitative analysis of the MR in all the samples would require determining the relative strength of the different contributions. In particular,

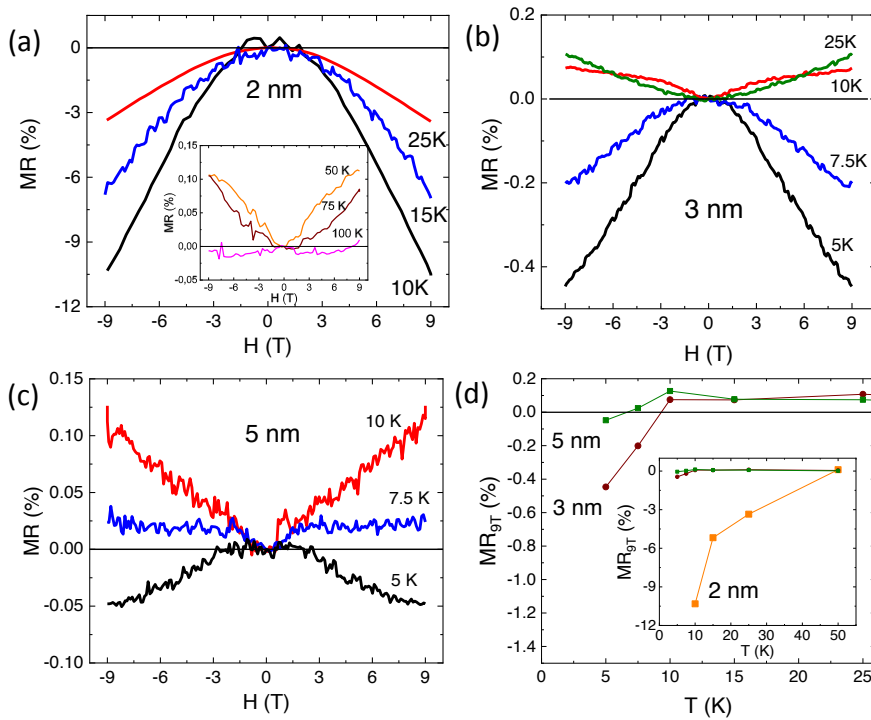


FIGURE 4.9: Magnetotransport measurements in the films near the disorder driven MIT. (a) MR in the insulating 2 nm film showing negative values at low temperatures (10-25 K), positive values at intermediate temperatures (50-75 K) and negligible MR at higher temperatures (100 K). (b) MR in the 3 nm film where the transition between negative MR and positive MR occurs between 7.5 and 10 K. (c) MR in the 5 nm film, in this case the transition occurs between 5 and 7.5 K. (d) Temperature dependence of the MR at 9 T for the measured flat films.

for samples close to the MIT (3 nm and 5 nm), weak localization and classical contributions to the MR seems to exhibit comparable magnitudes. Unfortunately, our experimental uncertainty does not allow us to accurately discriminate between both contributions and, thus, a quantitative analysis was not successfully performed.

As said above, the magnitude of the MR at low temperature in the insulating sample (2 nm) is more than one order of magnitude higher than the other contributions (see Figure 4.9 (a)). Although the physical origin of this MR is not yet elucidated in iridates, we must note that negative MR of an insulator is usually explained by Zeeman splitting of the localized states. In this scenario, Zeeman effect would split the energy levels according to the

spin, creating, therefore, new available states near the Fermi level that could contribute to the current transport, giving rise to a negative magnetoresistance with an expected H^2 dependence [86]. The observed dependence with field in the 2 nm sample varied between $H^{1.75}$ and H^2 , which is in a reasonable agreement with the expected theoretical dependence, taking into account that classical (positive) MR has not been subtracted.

Although these results may suggest that insulating phase could be sensitive to magnetic ordering, it is worth noting that no traces of ferromagnetism has been observed in any of the films by Superconducting Quantum Interference Device (SQUID) measurements. However studies have found magnetic ordering in superlattices of SrIrO₃/STO when the thickness of the SrIrO₃ was reduced [87].

4.1.3 Hall Effect measurements

To further characterize the electric properties of the SrIrO₃ films and their possible alterations due to the reduction of thickness, Hall Effect measurements at different temperatures were performed on the series of films with different thicknesses.

Figure 4.10 (a) depicts the raw measurement of the resistance between the Hall contacts in a 10 nm film at 300 K when a magnetic field (H) sweeping between 9 and -9 T is applied perpendicular to the film and a current of 1 μ A is flowing through the intensity contacts (see Appendix A). All the measurements regardless of the thickness of the film and the temperature presented linear signals. This is in contrast with several results reported in the literature [68] where non-linear Hall characteristics were attributed, in a two carrier model, to great differences between hole and electrons concentrations or mobilities.

Figure 4.10 (b) presents the same measurement once the corrections (Appendix A) to obtain the Hall voltage are applied and the sign of the effect is added taking into account the direction of the magnetic field and the current. After this step, all the measurements conserve the initial linear trend and all of them show a negative slope with the magnetic field. The resultant Hall coefficients (R_H) for the different films at 300 K are depicted in Figure 4.10 (c). It can be noticed that all the samples above the MIT limit (2 nm) have similar values of R_H (around $-7 \cdot 10^{-4} \text{ C/cm}^3$) while in the insulating 2 nm film it increases in absolute value ($-9 \cdot 10^{-4} \text{ C/cm}^3$).

The dependencies on temperature can be visualized in Figure 4.10 (d). In the case of the thicker films (10 nm and thicker), after the initial decrease (from 300 K to 200 K), the R_H follows a growing tendency towards positive values. The 5 nm film decreases faster at high temperatures and only

below 125 K it starts to grow again recovering the initial value of 300 K at 10 K. The thinnest semimetallic film of 3 nm shows a decrease tendency in the whole range of temperatures which is more abrupt at high temperatures and softened at lower ones. Finally, the insulating 2 nm follows a monotonous tendency with temperature up to the limit of our measurements, determined by the huge increase of noise when resistivity diverges at low temperatures.

Due to the semimetallic nature of the SrIrO₃ films it is widely accepted that its electrical transport is driven by both electrons and holes [44] [68]. Nevertheless, their respective contributions might not be entirely balanced. In this context Hall effect measurements can be used to determine the carrier that contributes more to the conduction [21]. The Hall coefficient in a two carrier system is described by [88]:

$$R_H = \frac{1}{|e|} \cdot \frac{(p\mu_h^2 - n\mu_e^2)}{(p\mu_h + n\mu_e)^2} \quad (4.6)$$

Where p and n represent the density of holes and electrons respectively and μ_e and μ_h are the mobilities of electrons and holes respectively.

In the present case all the Hall coefficients correspond to negative values, which is indicative of an electric transport dominated by electrons. Nevertheless, the obtained values are too small to ensure that the conduction is dominated by electrons, since the conductivity has slightly different dependencies on the density and the mobilities of both carriers, as can be observed in:

$$\sigma = e \cdot (p\mu_h + n\mu_e) \quad (4.7)$$

All the published bibliography on SrIrO₃ films coincides on the negative sign of the R_H [11] [68] [83], however, the dominance of one carrier over the other is not yet clear [76] and further measurements would be needed to resolve this dilemma.

Temperature dependences of the Hall coefficient are complex and, in the lack of a reliable model we may only offer qualitative arguments. The first striking feature of the Hall effect measurements is their difference with respect to resistivity measurements. Indeed, Hall coefficient in the insulating 2 nm thick sample exhibit a monotonous (nearly linear) dependence with temperature, reducing its absolute magnitude as temperature increases. On the contrary, semimetallic samples (see 10 nm curve) exhibit a non monotonous variation of their Hall coefficient with temperature, with a significant reduction (in absolute value) at low temperatures. As said above a single carrier model is not applicable to the iridate case as electronic

transport is controlled by the interplay between light electrons and heavy holes. Furthermore, some authors have claimed a balanced situation where a higher density of holes (up to 1.7 times that of electrons) may compensate for their lower mobility [76].

A tendency of the Hall coefficients towards lower absolute values (i.e., towards zero) is a sign that the system is changing its balance to a higher contribution of the holes. On the contrary, a shift towards higher negative values indicates an increased role of the electron carriers. Therefore, as the film approaches the insulating transition, hole contribution (either the hole density or their mobility) is less important in relation with that of electrons.

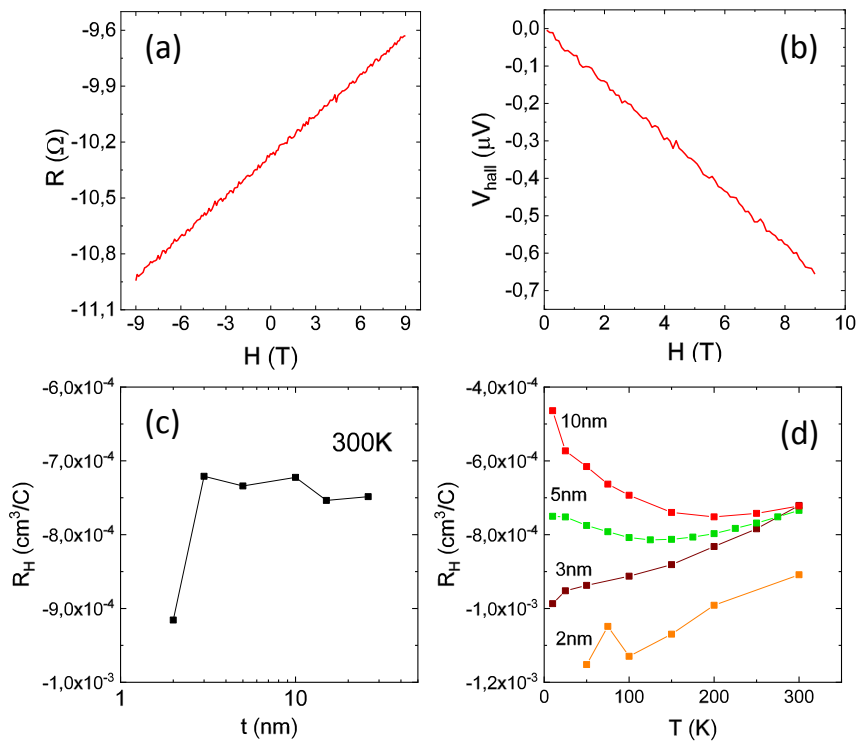


FIGURE 4.10: Hall Effect measurements in the series of SrIrO₃ films with different thicknesses. (a) Raw Hall measurement of a 10 nm film at 300 K. (b) Hall Voltage after the corrections mentioned in Appendix A are applied. (c) Dependence of the Hall coefficient with the thickness of the film at 300 K. (d) Dependence with temperature of the Hall coefficient in the films near the MIT.

4.2 Transport properties of the nanostructured films

In Chapter 3 it has been shown that the conditions of deposition in sputtering can be adjusted to obtain nanostructured (NS) surfaces of the SrIrO₃ films. Besides the potential of these holes as self-assembled arrays for electronics applications, this kind of changes in the morphology of the films can also alter physical properties of the material such as electric transport, magnetism or the crystal structure [70]. In this context it is intriguing to study if the transport properties can be altered in the NS films.

4.2.1 Metal-Insulator Transition in nanostructured films

With the aim of elucidating this dilemma, a series of films with different thicknesses were grown using the suitable conditions for the NS films. As in the case of the flat films the deposited thickness was measured by reflectometry in the thicker films and it was extrapolated by taking into account the deposition time to the thinnest ones. Figure 4.11 presents the AFM topography image of NS films with thicknesses of (a) 18 nm, (b) 5 nm and (d) 2 nm. In the 2 nm film and below, the terraces of the substrate are replicated similarly to the case of the thinnest flat films. One way to evaluate the depth of the holes is to analyze the rms of the films. Figure 4.11 (d) depicts the dependence of the rms in the film thickness for the flat and the NS series. In both cases as the thickness is reduced the roughness of the film is minimized, however this tendency is more pronounced in the case of the NS films. It is worth noting that even in the thinnest films the NS morphologies present higher values of rms than their flat counterparts indicating the presence of holes in the whole series. Figure 4.11 (e) depicts the profiles of the holes of NS films with different thicknesses. As the thickness of the films is decreased hole depths are also reduced, but even with that, noticeable traces of the holes can be visualized even in the thinnest films.

The structural properties of the films with holes were evaluated by means of θ - 2θ X-ray scans, which are presented in Figure 4.12 (a). As in the preceding section, the position of the maxima in the (002) peaks of the NS films does not depend on the thickness of the film and only a broadening and a diminution of the peak can be observed. As before, X-ray scans were adjusted to obtain more accurately the out of plane parameter, c . Figure 4.12 (b) depicts the c parameters of the NS films in comparison with the ones obtained in the previous section for the flat films. The values of the parameter are comprised between 4.065 and 4.05 Å and no tendencies with thickness can be observed from these measurements. Moreover the c parameters are in the same range of the flat films ones indicating that not major structural

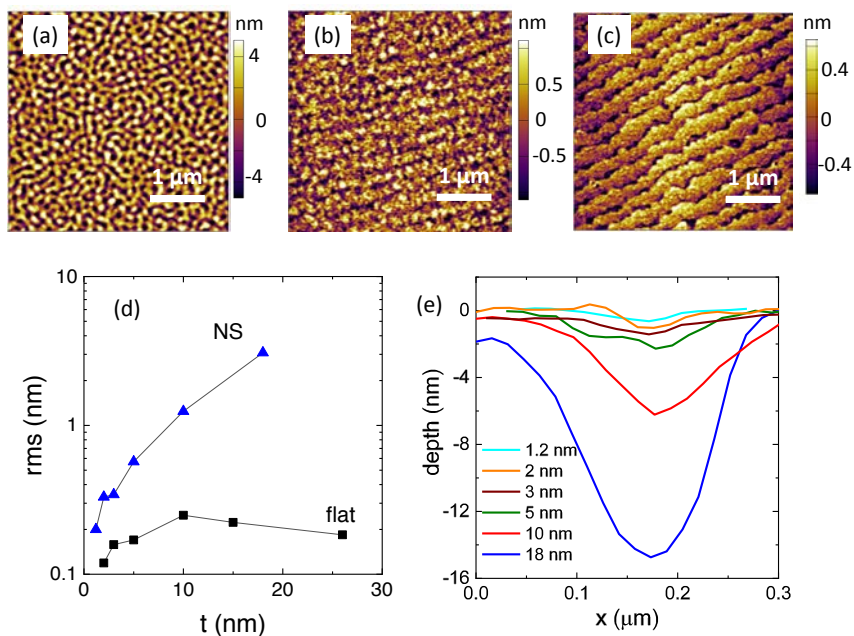


FIGURE 4.11: AFM images of NS SrIrO_3 films. The thickness of the films is (a) 18, (b) 5, and (c) 2 nm respectively. (d) Evolution of the roughness with the thickness in both the series of flat and NS films. (e) Profiles of the holes in the different films. As the thickness of the film is reduced the associated holes are decreased. Nevertheless, even at the thinnest films clear traces of the arrays of holes can be observed.

changes have occurred in the NS films. It is worth noting that, contrary to the case of the annealed films, the absence of significant differences in the c parameter between both series demonstrates that the content of oxygen vacancies did not change even in the low PO_2 atmosphere conditions used during the deposition of the NS films.

Finally, the electric properties of the NS films were evaluated with a standard four-probe configuration using platinum contacts. No measurements of Hall effect were performed in these films (Appendix A). Figure 4.13 (a) depicts the sheet resistance of the films within the usual range of measured temperatures (10-300 K). As in the case of the flat films, the NS films present a semimetallic behavior at high temperatures in the thick samples and an insulating region at low temperatures. In this series, the films are semimetallic at 300 K up to 2 nm when the MIT takes place and only

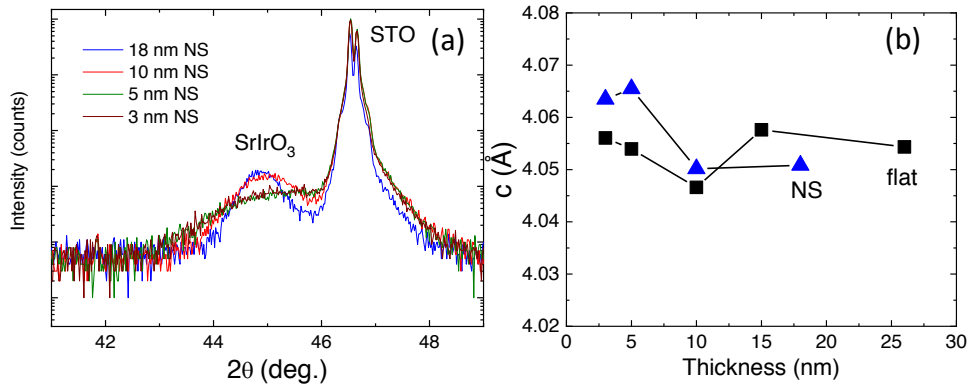


FIGURE 4.12: (a) θ - 2θ measurements of the (002) peak of the SrIrO₃ films with holes and their underlying STO substrates. All the measured film peaks appear in the same 2θ position. (b) Out-of-plane parameters of both the flat and NS films which have been obtained by adjusting the respective scans. No clear tendencies can be observed neither by changes in the thickness or in the morphology of the films.

the film grown at 1.2 nm presents an insulating behavior in the whole measured range (i.e., insulating at room temperature). It is worth noting that the films of 2 nm, 3 nm and 5 nm present very similar sheet resistances despite their different thicknesses. This overlapping in the curves could be generated by a compensation mechanism between the film thickness and the roughness. Figure 4.13 (b) presents the resistivity of the NS films measured at 300 K. The whole series of films show similar resistivity values that do not depend on the thickness, even in the insulating 1.2 nm film.

Figure 4.13 (c) depicts the temperature dependence of the resistance normalized by its value at 300K. In this plot the transitions between the insulating and the semimetallic regimes (T_{MIT}) can be easily observed. Moreover, as in the case of the flat films, it can be appreciated that the films present slightly different tendencies in the semimetallic regime according with their thickness and their curves do not collapse into a single one. The transition temperatures of the NS films, again defined by the temperature at which the minimum in the resistivity occurs, can be visualized in Figure 4.13 (d). Similarly to the flat films, as the thickness approximates to the MIT the T_{MIT} increases. Thus, in summary, transport properties of the NS films exhibit similar characteristics as those of the flat films but with a clear tendency towards an enhanced insulating regime.

To better study the differences and similitudes between both series, we

will perform a similar study as previously by separately analyzing the insulating and the semimetallic regions in the NS films.

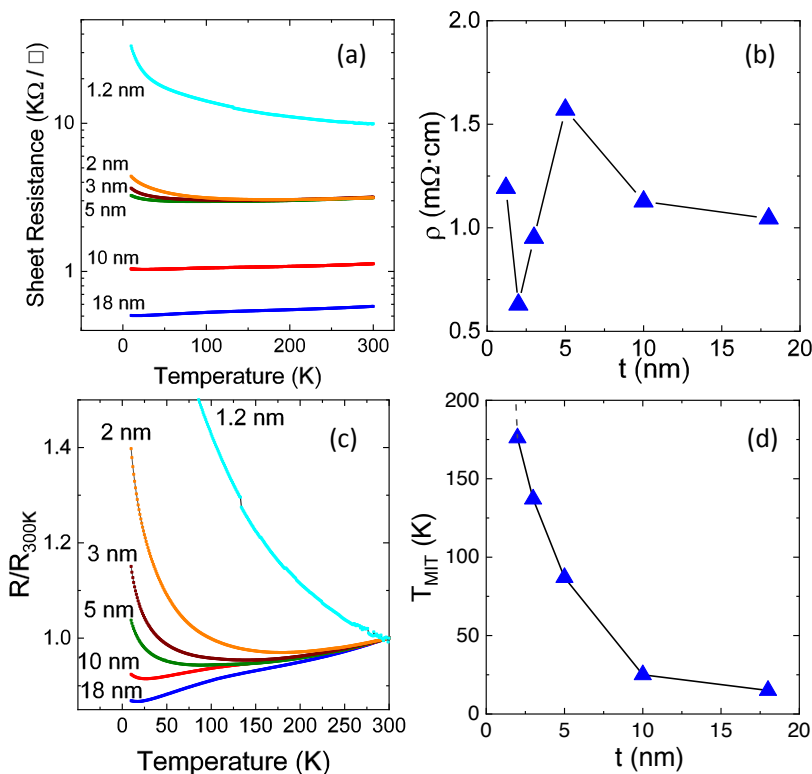


FIGURE 4.13: (a) Sheet resistance of the series of films with holes in the temperatures comprised between 10 and 300 K. (b) Resistivity of the NS films at 300 K. All the films have similar resistivity values that do not depend on the thickness of the films. (c) Dependence of the R/R_{300K} quotient with the temperature. The different NS films present slightly different dependences in the semimetallic part and different T_{MIT} . (d) Transition temperatures in the semimetallic NS films.

Semimetallic Region

We will now concentrate on the analysis of the transport in the semimetallic region. Similarly to the flat films the semimetallic region of the NS films can be fitted to a non-Fermi liquid behavior, i.e., to a power-law temperature dependence. The fittings were performed using the same methodology as previously described (as depicted in Figure 4.14 (a)). However, as MIT occurs at higher temperatures, fitting regions were accordingly adapted and,

for example, it was reduced to 200 K-300K for the 2 nm film. The results of the fittings for the whole series can be observed in Figure 4.14 (b). First, we may observe that exponents (above 2 in all the samples) are systematically higher than for the flat films. Second, a tendency towards higher exponents at lower thickness is still present although α barely changes between 10 nm and 3 nm. As previously said, this exponent not only accounts for the possible scattering mechanisms but it also may be influenced by the disorder. In particular, a higher exponent may be associated to a higher degree of disorder. Although no microstructural demonstration can be provided we again observe that the analysis of transport properties in the semimetallic region suggests a modification of disorder in the NS films.

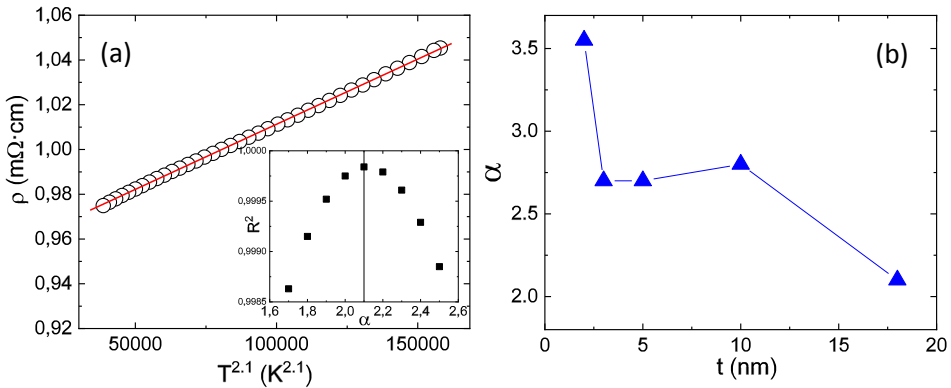


FIGURE 4.14: (a) Fitting of the 18 nm NS film resistivity with the temperature. (Inset) R^2 dependence on the α used for the fitting. In this case R^2 is optimized for $\alpha=2.1$. (b) α adjustments for the NS film series.

Insulating Region

Figure 4.14 (a), (c) and (e) depict the resistivity curves of the 2 nm, 3 nm and 5 nm films with holes. These films above the MIT present a semimetallic behaviour at room temperature which turns into an insulating regime at lower temperatures. In all three plots the red arrow indicates the beginning of the insulating regime, i.e., the transition temperature T_{MIT} . The low temperature regions of these films can be adjusted in the 2D weak localization limit, by using the expression 4.3. In all the three cases, the fitting of experimental data with theory is excellent (see Figure 4.15 (b), (d), and (f)), thus confirming a signature of the disorder driven MIT triggered by

the reduction of thickness, similar to the previous observed in the 3 nm flat film.

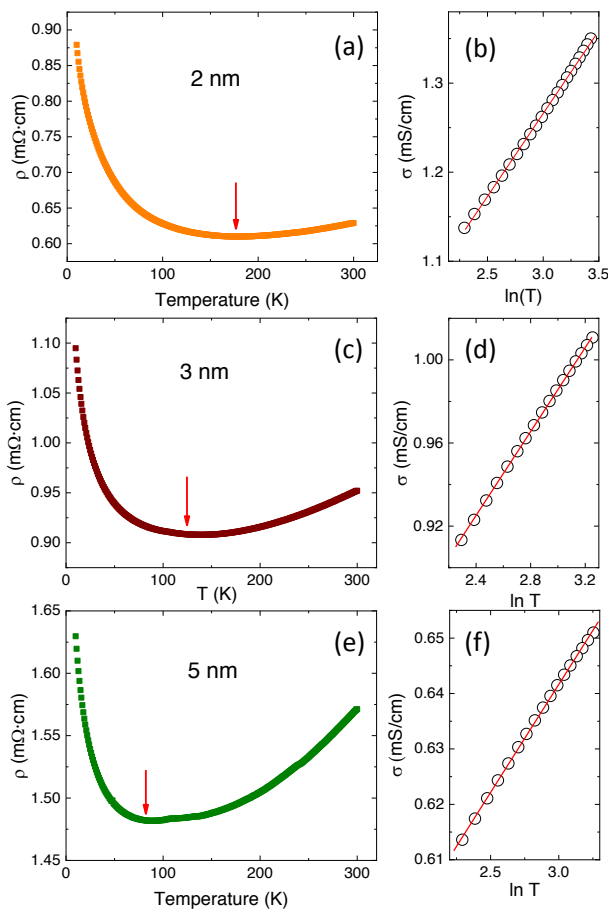


FIGURE 4.15: Resistivity curves of the (a) 2, (c) 3 and (e) 5 nm films with holes. The red arrows indicate the T_{MIT} and, thus, the separation between regimes. (b), (d) and (f) are the Weak localization 2D adjustments to the low temperature part of the previous resistivity curves.

In the case of the 1.2 nm film, the resistivity exhibits an insulating behavior in the entire measured range of temperatures, as it can be observed in Figure 4.16 (a). The sheet resistance curve crosses the MIR limit at ≈ 17 K, which is significantly lower than the one of the insulating flat film discussed in the previous section. This difference may already suggest that localization is weaker in NS films. The resistivity curve (Figure 4.16 (a) inset) can be separated in two regions according with their dependence with

the temperature. Similarly to the 2 nm flat film, the low temperature region of the curve can be nicely fitted with a VRH equation in 2D (Figure 4.16 (b)). However, unlike the flat insulating film, the high temperature region cannot be adjusted with a thermal activation equation. Nevertheless, the dependence of the conductivity in this range of temperatures is again in well agreement with the weak localization model in 2D (Figure 4.16 (c)). Thus, the transport results in the insulating region of NS films seems to suggest that growth mechanisms leading to the nanostructured surface, also modify the overall disorder in the films.

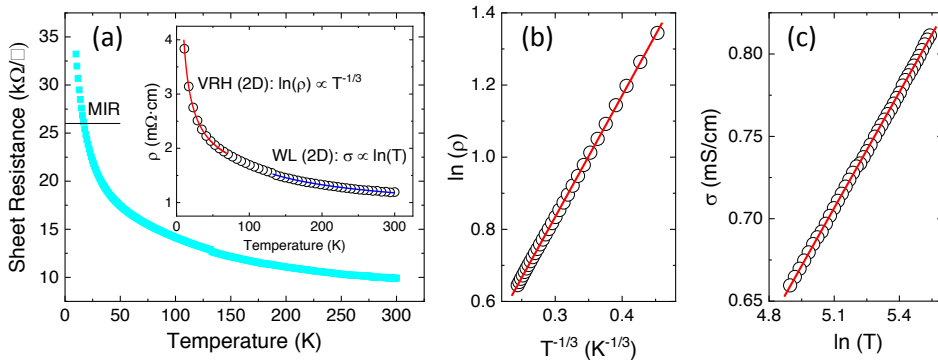


FIGURE 4.16: (a) Sheet resistance of the 1.2 nm film with holes. Inset. Resistivity curve of the same film indicating a VRH dependence at low temperatures (red curve) and a Weak localization dependence at high ones (blue curve). (b) Adjust of the VRH 2D mechanism. (c) Fit of the Weak localization model in 2D.

4.2.2 Magnetotransport in nanostructured films

As in the case of the flat films, the NS ones seem to undergo an Anderson MIT by the reduction of thickness. Therefore, as it was checked in the flat films, a negative MR dependent on the disorder should arise at low temperatures in the films near to the MIT caused by localization. Figure 4.17 presents the MR measurements in the NS films. Figure 4.17 (a) depicts the MR in the 5 nm NS film for several temperatures. As in the case of the flat films, a transition can be observed between positive MRs at high temperatures and negative MRs at low temperatures. More interestingly, at intermediate temperatures (10 K and 15 K, see Figure 4.17 (b)) a crossover from positive to negative MR may be observed. This is a clear evidence that the two different contributions (i.e., classical positive MR and negative

weak localization MR) are competing, each of them with its respective field dependence.

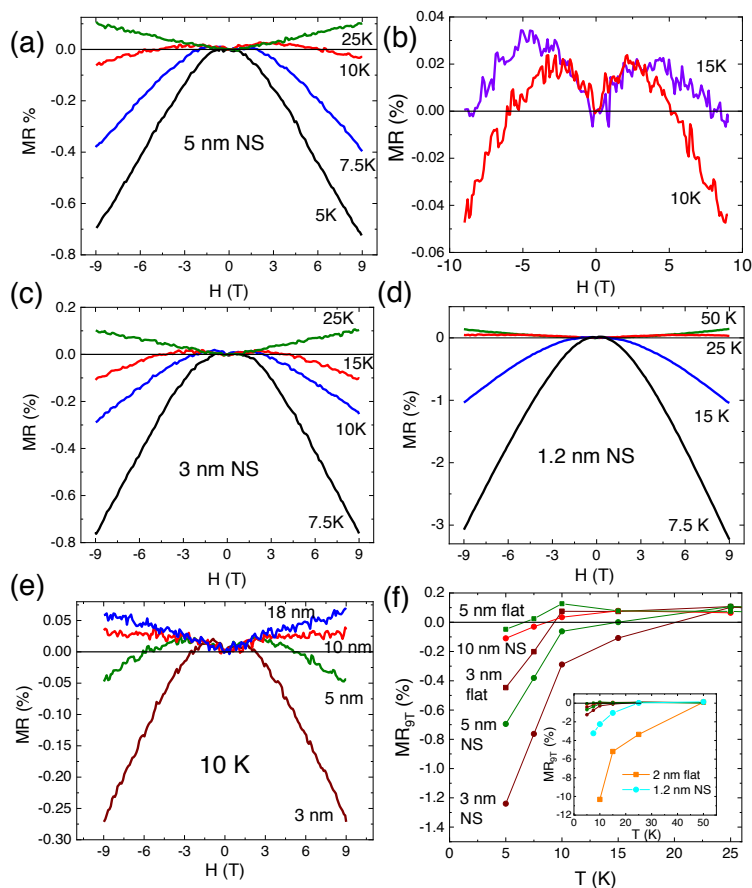


FIGURE 4.17: Magnetotransport in the series of NS films with thicknesses of (a) (b) 5 , (c) 3 and (d) 1.2 nm. (e) Evolution of the MR at 10 K for films with different thicknesses. As the thickness of the film is reduced the MR tends to more negative values. (f) Comparison between the MR at 9 T in flat and NS films. As the disorder of the film is increased the negative contribution to MR is enhanced.

As the thickness of the films is reduced to 3 nm and 1.2 nm (Figures 4.17 (c) and (d)) the negative MR increases and the transition from positive MR to negative MR is shifted towards higher temperatures. This effect can be better appreciated in Figure 4.17 (e), where the MRs at 10 K of films with different thicknesses are presented. While the thicker films of 18 nm and 10 nm exhibit a positive MR at 9 T, in the thinner films of 5 nm and 3 nm the resistance is reduced at high fields. Moreover, the transition is

progressive indicating the gradual increase of disorder as the thickness is reduced. On the other hand, the MR at 7.5 K and 9 T in the 1.2 nm film is around 3%, significantly lower than its insulating counterpart, the flat 2 nm film. A global comparison of the MRs in the NS and flat films is depicted in Figure 4.17 (f). In general, MR follows similar trends in both cases, with negative MR accompanying insulating behavior and thus, an extended range of temperatures with negative MR in the case of NS films.

4.2.3 Conclusions of transport mechanisms for flat and nanostructured films

Before concluding the analysis of the transport properties in SrIrO₃ films it is worth to compare the above results in the flat and the nanostructured films. In Figure 4.18 we summarize the results from the above Sections by depicting (a) the normalized resistivity at 300 K, (b) the metal to insulator transition temperature and (c) the α exponent of temperature dependence power law for ρ . In these figures we may observe a clear tendency towards a disorder driven MIT (Anderson like) at low thickness. In the case of flat films, the fully insulating behaviour (from room temperature) is abruptly achieved when thickness is reduced from 3nm to 2nm. On the opposite, NS films seem to follow a smoother behaviour with a progressive increase of disorder when thickness is reduced as evidenced by the T_{MIT} in Figure 4.18 (b). Noticeably, this different behaviour is not evidenced in the overall resistivity values, that are comparable for both series of samples (Figure 4.18 (a)), with only the 2 nm flat film exhibiting a larger resistivity.

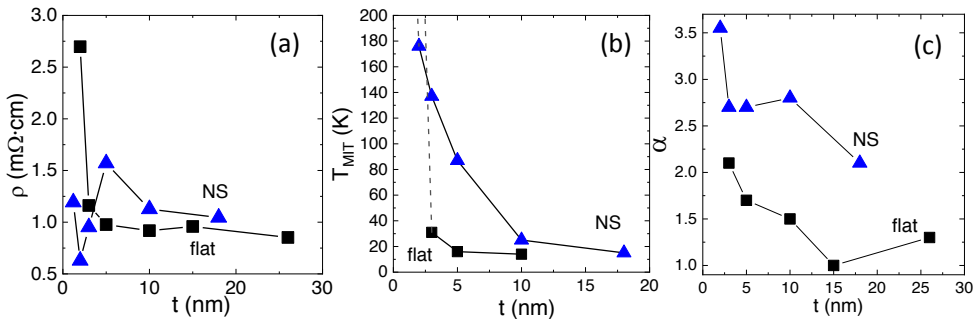


FIGURE 4.18: Comparison of the transport properties of the series of flat films (black squares) and the NS films (blue triangles). (a) Resistivity evolution with the thickness. (b) Transition temperature of both series of films.

The analysis of the temperature dependence of the resistivity suggests a higher degree of disorder in the NS films (higher exponent, see Figure

4.18 (c)). Additionally, the weak localization phenomena can be observed in a wider range of thicknesses and temperatures in the NS films in comparison with the flat films. This supports the previous observation of a broadening of the transition caused by the changes in the morphology. The magnetotransport measurements, which are presented in the previous section, are also in well agreement with these results. It is worth noting that this increment in disorder cannot be explained by a geometrical effect of the morphology, being the origin of these alterations still unknown.

4.3 Transport properties of Sr_2IrO_4 films

Additionally to the MIT triggered by the reduction of thickness, the different strontium iridates RP phases present divergent electronic transport properties. The extremes of the series are the $n=\infty$ and the $n=1$ phases which present semimetallic and insulating behavior respectively. This is the consequence of the change in the bandwidth of the orbitals, which modifies the relation between the electron correlation and the bandwidth. This variation opens a gap in the Sr_2IrO_4 films inducing the insulating state, which has been classified as Mott MIT [10]. Due to their differences in the transport with the $n=\infty$ films, the Sr_2IrO_4 films constitute an excellent opportunity to compare the electrical and RS properties.

As explained in Chapter 3, this phase can be deposited on STO substrates by PLD with an excellent quality. Depositing platinum in a four probe configuration, the electrical properties of the film can be measured by means of four probe measurements (Figure 4.19). The resultant resistivity curve of a 30 nm $n=1$ film is depicted in Figure 4.19 (a). The films exhibit an insulating behavior in the whole range of measurement (10-300 K). Similarly to the insulating 2 nm $n=\infty$ films, the obtained values of resistivity can be modeled by a VRH in 2D at low temperatures (red line) and a Thermal activation at high temperatures (blue line). However, this film is almost two orders of magnitude more resistive than the ultrathin $n=\infty$ phase. It is worth noting that at very low temperatures the experimental resistivity points of the film start to lose the coincidence with the VRH model. This effect is the product of a reduction in the increment of the resistivity with the reduction of the temperature and could be caused due to the approximation of the resistance of the system to the limit of measurable resistance of the PPMS. The quality of the shown fits can be checked in Figure 4.19 (b) for the thermal activation and in Figure 4.19 (c) for the VRH, where the linearization of the equations allow a better appreciation of the coincidence

between the fitted models and the experimental values. The fitted equation for the thermal activation at high temperatures adjust the Δ to 62 meV which is an order of magnitude higher than the one obtained in the 2 nm $n=\infty$ film. Similar adjustments in $n=1$ films with a VRH model at low temperatures and a thermal activation expression at high ones were reported in the bibliography [89].

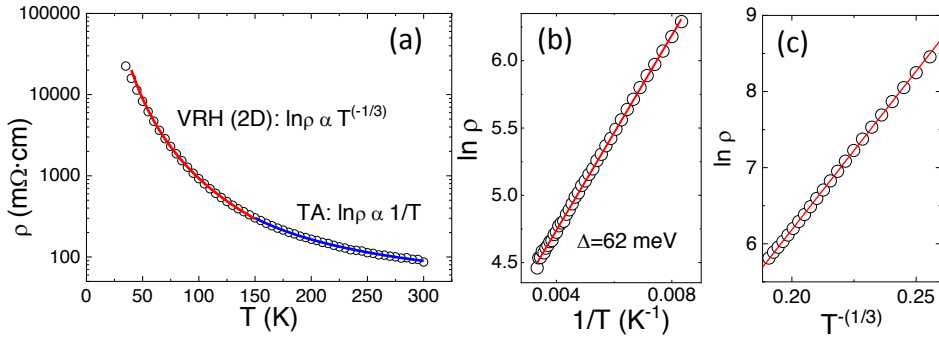


FIGURE 4.19: Temperature dependence of resistivity of a 30 nm $n=1$ film. (a) The resistivity curve can be split into a low temperature region, governed by a Variable Range Hopping mechanism (Red), and a high temperature region that can be adjusted to a Thermal Activation expression (blue). (b) Linearization of the high temperature region with the Thermal activation plot. (c) Linearization of the low temperature region showing the fit with the VRH equation.

Chapter 5

Resistive Switching in Strontium Iridates

In the second part of this thesis the macroscopic electrical properties of $n=\infty$ and $n=1$ films were studied. Strontium iridates Ruddlesden-Popper (RP) phases have proved to be an excellent playground for MITs in well agreement with the bibliographic reports [11] [68] [69] [74]. The possibility of bringing the system into the edge of a Metal-Insulator Transition (MIT) makes Strontium iridates excellent candidates to exhibit Resistive Switching (RS) properties due to the proximity of the transition and the accessibility to specific mechanisms that enhance the switching performance. Therefore the study of RS properties in the previously examined $n=\infty$ and $n=1$ films arise as an appealing case to evaluate whether the observed MITs can have a significant impact on the RS behavior.

To analyze these properties, C-AFM equipment in an in-plane configuration (see Appendix A) was employed. In this configuration the extensive properties of the film can be minimized allowing studying the intensive properties of the material and avoiding leakage currents [90] [91] [92]. This is especially relevant for films with different thicknesses where different configurations could enhance possible geometrical effects hindering the intrinsic properties of the films.

5.1 Resistive Switching in SrIrO_3 films

5.1.1 I-V curves in semimetallic flat SrIrO_3 films

Figure 5.1 (a) depicts a representative complete C-AFM I-V cycle on a semimetallic SrIrO_3 film of 26 nm of thickness. The whole curve can be split in 4 different parts which are represented with distinct colors and numbered.

1. The black curve starts at 0 V applied to the film and as the Voltage is increased the current starts to rise up to 5 V in the High Resistance State (HRS). Although in Figure 5.1 (a) no current can be appreciated up to 4 V, a closer look of the measure shows a smooth increase from 0 V.
2. In the red part, as the voltage drops from 5 V to 0 V the current starts to decrease by the upper part of the graph in the Low Resistance State (LRS) until it reaches 0 V.
3. Afterwards, in the blue curve, the voltage polarity is reversed and the negative current starts to increase rapidly while the system is still in the LRS. This increase of current reaches a peak at ≈ -2 V where it starts to decrease even increasing the voltage to -5 V.
4. At the point the green curve starts, the system has switched its state to HRS and therefore the curve returns to 0 V close to 0 nA in the graph. Once a complete cycle has been performed the system is in the HRS and the next cycle can start again (1).

Although Figure 5.1 (a) represents directly raw cycle obtained by the C-AFM, the scale does not allow appreciate many details contained in the I-V curves. This is particularly relevant in the parts of the curve in the HRS, since the low measured currents cannot be differentiated from the total absence of current. In order to avoid this problem, the curves presented in this thesis are depicted in absolute values of current and in logarithmic scale. This can be appreciated in Figure 5.1 (b) which shows the same I-V curve with the same colors and numbers. In this figure the HRS parts of the curve ((1) and (4)) can be observed in more detail. Contrary to the first impression of Figure 5.1 (a), the absolute value current increases continuously from 0 V in both branches without any clear threshold Voltage (V_{th}).

Analyzing the whole curve it can be stated that SrIrO₃ films present a bipolar RS behavior, where positive voltage (applied to the sample) sets the system into the LRS and negative voltage reverses this situation and resets the system into the HRS. The resistance values for the HRS and the LRS suffer changes between the different branches and the different cycles. Nevertheless an estimation of the relative variation of resistance between states (R_{HRS}/R_{LRS}) can be made by comparing the currents of both states at low Voltages (0-1 V), where no transitions are expected to occur ensuring, therefore, that the system is completely set in one of the resistance states. This relative variation of resistance ranges between 10^2 and 10^3 evidencing a strong RS effect. It is worth noting that while the presented curve of Figure 5.1 was measured using a voltage cycling between 5 and -5 V, the RS effect

was also observed using other limit voltages. As the tension is increased the cycle tends to “open” more, boosting the R_{HRS}/R_{LRS} quotient. Nevertheless, at the same time the surface degradation is accelerated, thus, reducing the maximum number of consecutive cycles in a single point. Therefore, a balance must be established between the endurance of the switching and the relation between resistance states by adjusting the cycling voltage. During the experiments this was optimized for 5 V and was kept at this value for the $n=\infty$ samples to allow the comparability between the results in different films.

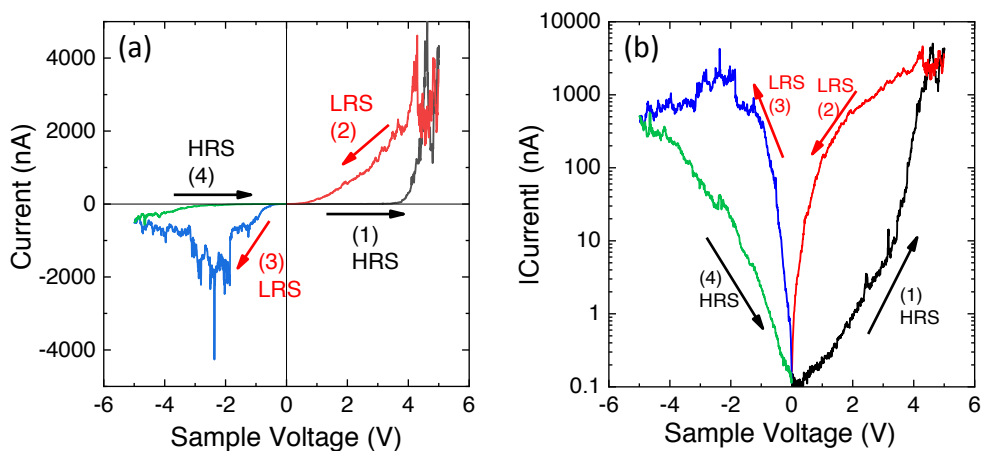


FIGURE 5.1: Complete RS cycle on a 26 nm $n=\infty$ film. The complete cycle can be divided in 4 parts numbered (1), (2), (3) and (4) which are represented with the colors black, red, blue and green respectively. The arrows indicate the path of the voltage applied to the sample. The system enters into the LRS (red arrows) by applying positive voltages while negative voltages induce the HRS (black arrows) forming a double hysteresis pinned at 0 V. The curve is represented in a linear scale in (a) and in logarithmic scale of the absolute values of the current in (b). Since the details of the RS can be better appreciated in (b), in the rest of the Chapter the logarithmic scale will be used to present the I-V curves.

It is worth noting that stability of the cycling cannot be extended beyond 10 cycles (approximately). This performance is very poor in comparison with the maximum of cycles of designed devices (10^6 - 10^8) [7] but is in well agreement with other similar experiments considering the usual problems of stability that have C-AFM when measuring RS curves [93] [94]. These drawbacks include the anodic oxidation of the surface, the progressive degradation of the tip and the presence of atmospheric contamination.

5.1.2 Resistive Switching in SrIrO₃ films over large areas

In this context, during the C-AFM measurements, the present films have shown a particular tendency to react under large positive sample voltages. Figure 5.2 (a) and (b) depict the topography and the current map of a $15 \times 15 \mu\text{m}^2$ whose central $10 \times 10 \mu\text{m}^2$ squared area was previously scanned at 5 V of sample voltage. On one hand, the topography image has experienced an expansion in Z in comparison to the surrounding non-scanned area. On the other hand, the current map shows a clear decrease of the current (black square) from the pristine state (bright surrounding area). The coincidence between the changes in morphology and current can be better appreciated in Figure 5.2 (c) where the profiles of the lines depicted in (a) and (b) showing a clear correlation. Moreover, in this graph these alterations can be better quantified. On one hand, the affected area experiences a swelling of 5 nm while, in the same region, the current is decreased 3 orders of magnitude. Another prove of the alteration of the surface due to the application of voltage can be observed in Figure 5.2 (d) where a grid of spots with an increase of the height can be appreciated. The places where these spots are located were used to perform I-V curves that include high positive sample voltages. It is therefore clear that enough large positive voltages induce a reaction in the surface that alters the topography and generates a decrease in the current. These combined effects can be explained with an anodic oxidation effect at the surface of the iridate film [95].

Moreover the surface of $n=\infty$ films can become unusable with time due to the surface contamination, as it has been explained in the Chapter 3. Since C-AFM measures depend highly on the state of the surface, all the I-V curves were taken at the same day of the deposition minimizing the contamination at the surface and obtaining this way reliable measurements. Nevertheless, current maps are more aggressive than I-V curves since the apex of the tip has to rub the same area multiple times at high voltages. Moreover the obtaining of entire current maps is also more time consuming than the I-V curves which holds up the process of optimization of the measurements. These two factors make the current maps more challenging to be performed.

In order to measure properly current maps, several strategies were applied. Firstly, the measurements were conducted in a close chamber with a Nitrogen atmosphere reducing, in this manner, the humidity near the operation zone. This minimization of the humidity reduces the surface oxidation processes that degrade the film when electrons are injected from the probe [95].

Secondly, a non continuous layer of Pt NP was deposited “in situ” on

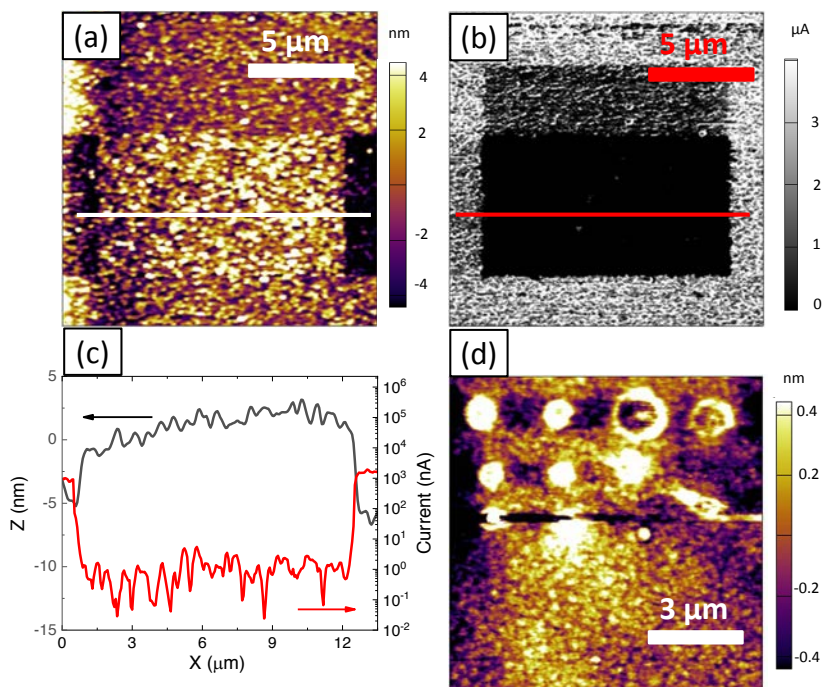


FIGURE 5.2: (a) Topography and (b) current map of a $15 \times 15 \mu\text{m}^2$ area where the central area was scanned previously at 5 V. The anodic oxidation produced in the surface generates a change in both images. (c) Correlation between the current and the topography alterations in the profiles of (a) and (b). (d) Grid of points where I-V curves were performed changing the topography of the film.

$n=\infty$ films as described in the Chapter 3. The purpose of this capping layer is threefold. On one side, it improves the contact between the sample and the probe increasing the current signal. In second place, it removes the debris of the tip apex rubbing it against the NP. Moreover the capping acts as a protective layer between the probe and the film making the C-AFM measurements less aggressive to the film. The size and distribution of the NP coverage are key factors to ensure that the subsequent C-AFM measurements can take place with unambiguous results. Pt NPs must be as extended as possible without forming continuous paths over the surface. If an overextension takes place the lower resistivity of the Pt would prevent the current to circulate through the iridate film and, therefore, preventing any switching between states. On the other hand, if the NPs are too dispersed its effect would be diminished and would not protect the film and improve the contact so effectively. In the case of the size, NP must be large

enough to prevent being swept by the lateral force of the AFM tip when scanning. Small particles are usually less attached to the film surface and its removal could be seen as a change in the conductivity of the surface hindering possible RS effects.

Finally the positive voltages necessary to set the film into the LRS have to be reduced from those used in the I-V curves to avoid the observed oxidation effects.

Taking these steps as precaution, the current maps of the HRS and LRS were measured in a 26 nm film of $n=\infty$ phase as it is depicted in Figure 5.3. To illustrate the different resistance states in the same image, a series of scans applying different voltages were performed sequentially. The sequence of scans is composed by steps of "writing" and "reading". In the former ones the sample is biased with enough voltage to switch between the resistance states while in the last ones the scans are performed in a larger areas at 0.2 V to observe the previous writing steps without modifying them.

Figure 5.3 (a) presents a reading $50 \times 50 \mu\text{m}^2$ current map made of an area of the film where a previous writing scan of $35 \times 35 \mu\text{m}^2$ was already made in the central square while applying -5 V. In this image two zones can be distinguished: a central dark square and its bright surroundings. The central dark square has experienced a reduction of conductivity due to the previous scan in comparison with the pristine state that surrounds it. During the previous scan, the "written" part of the film had been set into the HRS following the same tendency exhibited in the I-V curves. Figure 5.3 (b) depicts the topography of the current map, showing that the change in conductivity had no effect on the morphology of the film. Figure 5.3 (c) shows the current map of the same area after a writing scan of $20 \times 20 \mu\text{m}^2$ biased at 3 V had been performed in the center of the image. In this case three different resistance states can be visualized: the pristine state in the outer part of the image, the HRS as a dark squared ring and the LRS as a bright square in the center of the image where the positive biased scan was performed. It is then clear that positive biased scans with enough voltage can reset the HRS into a more conductive LRS as in the case of the previously studied I-V curves.

Figure 5.3 (d) depicts the topography image of (c) where minor alterations of the surface can be noticed in the area of the LRS by a slightly darker contrast. These changes in the morphology could be produced by a compression of the film in this area or by a partial removal of the Pt NPs in this zone. If Figure 5.3 (d) is observed carefully no accumulation of particles can be detected in the borders of the LRS central square. Moreover the current in the affected area is increased instead of diminished. For these

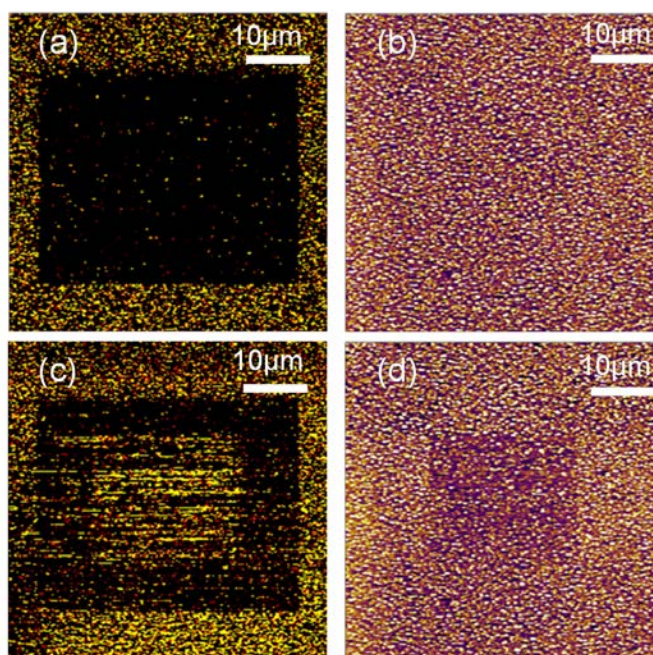


FIGURE 5.3: C-AFM current maps and topographic images of RS Set and Reset processes in a 26 nm SrIrO₃ film with Pt NP on the top. (a) 50x50 μm^2 current map with a 35x35 μm^2 inner square set in the HRS. (b) Topography image of (a) showing the lack of changes in morphology from the pristine state. (c) 50x50 μm^2 current map of the same area after a reset process of a 20x20 μm^2 inner square to LRS. (d) Topography image of (c) where small modifications of morphology can be observed in the inner square.

reasons the sweep of the particles can be discarded. On the other hand, the film compression in this scan could be explained by the increase of the normal load applied from 570 nN in the other scans to 1140 nN in this particular one. The increase of the normal load in this scan was necessary due to the lower voltage used in the scan (3 V) compared to the I-V LRS switch (5 V) and the present set process (-5 V). The voltage of this switch had to be lowered due to the possible presence of surface reactions of anodic oxidation [93] [94] that happened at +5 V which prevented the switching damaging the film.

All the described scans were carried out as square measurements of 256 points and lines with a speed of 1 line/s except for the one performed at 3 V which was executed at 0.1 line/s. This reduction of velocity results in an improving of the quality of the switching into the LRS, nevertheless, the

time needed to perform the whole set of measurements increased from 17 to 55 minutes. On the other hand, the possibility of having both resistance states in the same current maps, despite the huge amounts of time needed to perform the writing-reading processes, proves clearly that the RS is of a non-volatile nature. Moreover the fact that these states can be implemented over large areas demonstrates the robustness of this RS behavior.

5.2 Resistive Switching through Metal-Insulator Transition

In the second part of the results of this thesis the electric properties of the SrIrO₃ films were analyzed. According to the obtained results, the transport behavior of the films can be altered by changing the thickness (and triggering the MIT) or the morphology of the films. With the aim of evaluating the impact of these features into the RS characteristics, films with diverse thicknesses and topographies were measured by means of C-AFM I-V curves.

5.2.1 Resistive Switching in films with different thickness

Figure 5.4 (a) and (c) show the cycles for semimetallic films of 26 and 5 nm respectively while (e) presents the same I-V cycle performed on an insulating 2 nm ultrathin film. This last film has undergone the disorder driven Anderson MIT while the former two display a semimetallic behavior. On one hand, all three films have similar LRS curves which decrease regularly from +5 V to 0V and after reaching -2 V the current saturates or decreases indicating an increase of the resistivity.

Besides its effect on the shape of the RS hysteresis, the MIT also modify the reproducibility of the cycling. Figures 5.4 (b) and (d) present consecutive I-V cycles in semimetallic films of 26 and 5 nm. Although the different cycles follow the tendency described above, they do not fully coincide with each other having a wide variability in the path of the curves. On the other hand, in the 2 nm insulating film (Figure 5.4 (f)) one can observe that the consecutive cycles follow the same paths both in the positive and the negative part of the graph. These different behaviors suggest that a wide range of resistance states can be achieved in the semimetallic films and therefore HRS and LRS can have different values of resistance for the different cycles. In the case of the insulating film only two defined states can be achieved (HRS and LRS) and the system can only switch between them.

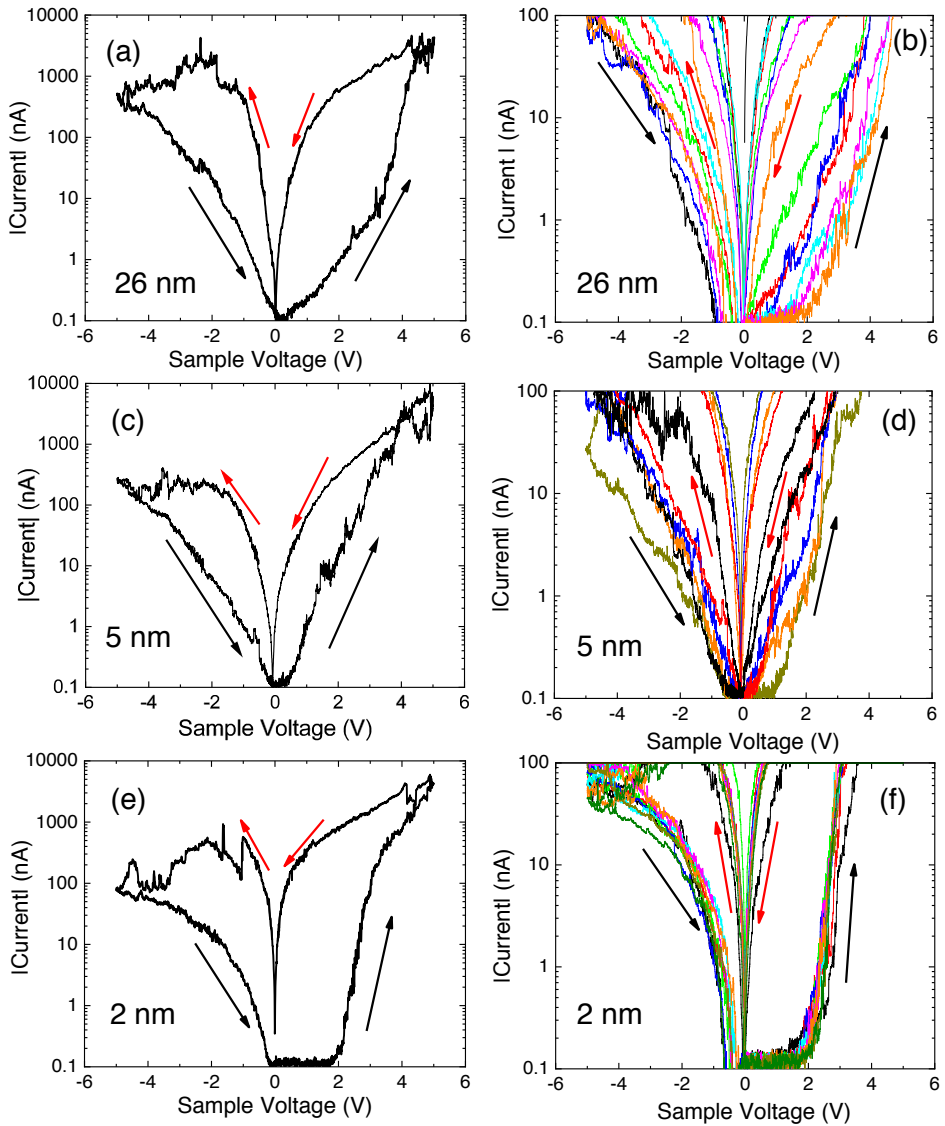


FIGURE 5.4: RS cycles for SrIrO_3 films with thicknesses of 26 (a), 5 (c) and 2 (e) nm, which follow the same bipolar RS behavior. While the two first cycles (a) and (c) correspond to semimetallic samples, (e) is taken in an insulating film which has undergone a MIT. A voltage threshold appears at the positive branch in the insulating 2 nm film, while in the thicker semimetallic ones it is absent. Consecutive RS cycles in $n=\infty$ films with thicknesses of 26 (b), 5 (d) and 2 (f) nm. In both semimetallic films of 26 nm and 5 nm the cycles have a greater variability in comparison with the cycles performed in the 2 nm insulating film. In all the cycles of the insulating sample a clear threshold appears at ≈ 2 V.

On the other hand, the HRS depends on the relative position of the sample to the thickness controlled MIT. Semimetallic samples (26 and 5 nm) follow the same tendencies with a smooth increase of the voltage in both the positive and negative branch. Contrary to this, in the positive branch of the insulating film (2 nm) the current remains at 0 up to ≈ 2 V when suddenly increases. The presence of this clear voltage threshold in the insulating film and the absence of it at the semimetallic films, regardless to their proximity to the MIT, indicate that the MIT and not the thickness is the responsible for changes in the RS behavior. This variation in the performance of the cycles is caused by the changes in the band structure of the films and it will be discussed in more depth in the section 4 of this Chapter.

Again, no significant differences can be observed between the 26 nm and 5 nm films ensuring that the changes in the resistivity do not come from extensive properties, such as the thickness, but from the intrinsic properties of the films that change due to the studied MIT.

5.2.2 Resistive Switching in nanostructured films

RS properties were tested as well in NS SrIrO₃ film. Two different films were measured: a 24 nm semimetallic film (Figure 5.5 (a) and (b)) and an insulating 1.2 nm film (Figure 5.5 (c) and (d)). In both cases the I-V curves present many resemblances with the already studied flat films. Both NS films show a bipolar cycle with the same polarity observed before. In the case of the 24 nm semimetallic film (Figure 5.5 (a)) the current experiences a smooth increase in the positive branch and no clear V_{th} can be observed similarly to the 26 nm flat film. On the other hand, the insulating 1.2 nm film (Figure 5.5 (c)) does not present any current up to 2 V when the V_{th} is surpassed and a sudden increase of the intensity occurs. It is worth noting that not only this behavior match with the one observed in the insulating flat film but also the value of the V_{th} is similar in both films. Figures 5.5 (b) and (d) depict several cycles of the 24 and 1.2 nm films respectively. As it can be observed both types of cycling are reproducible. However, in this case, the endurance of cycling in the thinnest films is reduced and non-consecutive cycles were depicted for this film. The evident similarities between flat and NS films indicate that the variations of electrical behavior studied in the NS films do not affect the RS properties of the film. Only significant changes in the bandstructure driven by the thickness triggered MIT can alter the I-V characteristic curves and induce the apparition of threshold.

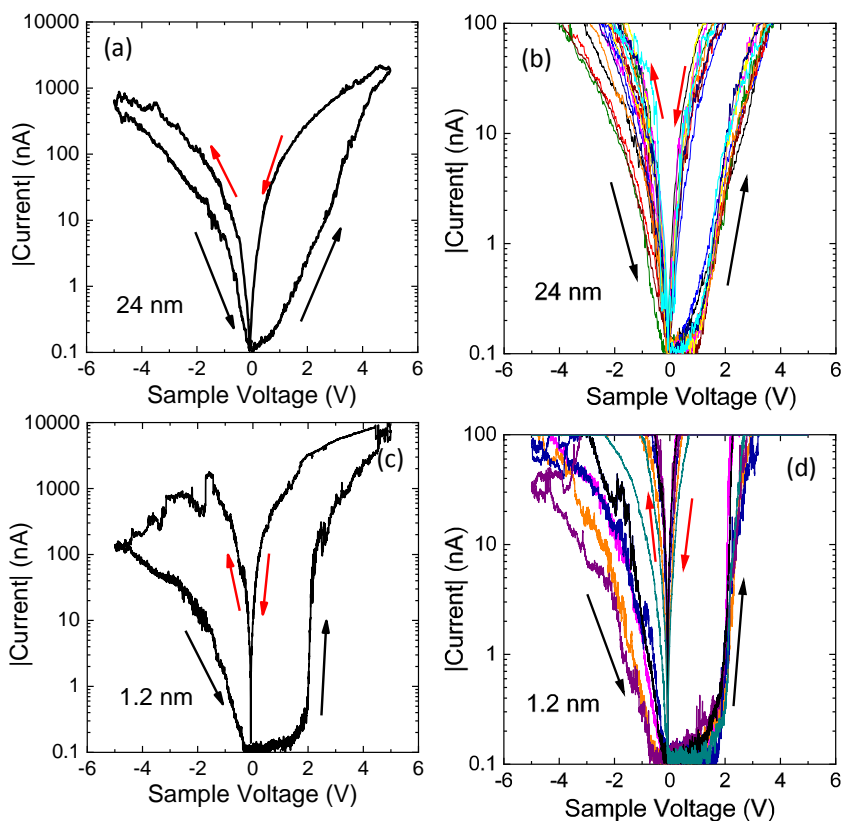


FIGURE 5.5: I-V RS curves on NS films. Complete cycles of a 24 nm (a) and a 1.2 nm (c) films. Several cycles of the 24 nm (b) and the 1.2 nm (d) films.

5.3 Resistive Switching of Sr_2IrO_4 films

In the previous section the RS properties of the SrIrO_3 films were studied at both sides of its MIT. In the present one the characteristic RS behavior of the $n=\infty$ phase is compared to the $n=1$ one, the other extreme of the RP series. The electric properties of this phase were studied in Chapter 4. Sr_2IrO_4 films were, in good agreement with bibliography, insulating in the whole range of measured temperatures. This behavior can be tuned to a more conductive one by different strategies. Among them the most used one has the substitution of metallic cations [49] [50] [51]. Nevertheless, a decrease in the resistivity of this phase has also been obtained in a volatile way by modifying the angle between Ir atoms whether by applying an external pressure [12] or by using large electric fields [52]. It is therefore appealing

to study the RS in this RP phase by the same methods used $n=\infty$ to compare their behaviors and possible mechanisms.

5.3.1 I-V curves in Sr_2IrO_4 films

Figure 5.6 depicts a complete I-V cycle of a 16 nm Sr_2IrO_4 thin film measured in a random point of the film by C-AFM (The voltage referenced is applied to the sample as in the case of the $n=\infty$ films). The cycle starts at 0 V and voltage rise continuously while the current keeps its value unaltered at 0 nA (arrow 1), being clearly at the HRS. At ≈ 4.5 -5 V an abrupt increase of current occurs and it keeps increasing up to 6V. As the voltage returns to 0, the current decreases more smoothly by the upper part of the graph (2) indicating that the system has been switched into the LRS. As the voltage is reversed to negative values, the current starts to increase immediately (3), symmetrically to the 6-0 V part of the curve. This increase of the current stops at ≈ -2 V where it starts to decrease smoothly until the maximum of -6 V indicating that the system is switching from the LRS to the HRS. Finally the I-V curve returns to 0 V slowly in the HRS (4).

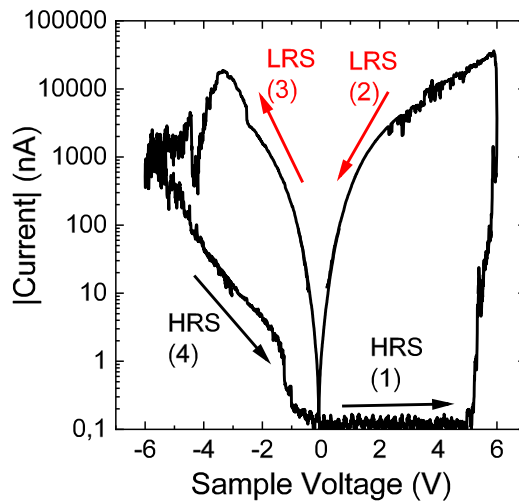


FIGURE 5.6: Complete RS cycle of a Sr_2IrO_4 film of 16 nm of thickness. The arrows follow the path of the I-V curve and indicate the current resistance state of every part. As in the case of the $n=\infty$ phase, positive voltage induce the LRS and negatives ones the HRS.

The present RS cycle shows many similarities with the ones of $n=\infty$ films presented in the previous sections. Both RS behaviors are bipolar based,

where positive sample voltage induces the LRS and negative voltages reverse it into the HRS. However the apparition of a threshold reminds more to ultrathin insulating film than its thick semimetallic counterpart, reinforcing the established causality relation between the MIT and the threshold.

5.3.2 Comparison with semimetallic and insulating SrIrO_3 films

A more detailed comparison of the different behaviors in the iridate films can be observed in Figure 5.7, where complete RS cycles of the 26 nm SrIrO_3 (a), 2 nm SrIrO_3 (b) and 16 nm Sr_2IrO_4 (c) films are depicted. As mentioned, only the films with an insulating behavior at room temperature present this voltage threshold in the ascending path of the positive branch, regardless from the origins of their insulating nature (Disorder driven in the case of the 2nm $n=\infty$ or electron correlation in the case of the $n=1$). It is worth noting that the thresholds do not have the same value (≈ 2 V for the 2 nm $n=\infty$ film and ≈ 4.5 -5 V for the $n=1$ thin film). Moreover, the Thermal Activation fits (Arrhenius equation) that describe the temperature dependence of insulating films at room temperature (Figure 5.7 (d)) provide distinct values of the Activation Energy. In the case of the ultrathin $n=\infty$ film this value is 6 meV while in the $n=1$ film is one order of magnitude larger (62 meV). It can be notice that an increase of the Δ could be the responsible of generating an increase of the V_{th} , establishing, therefore, a connection between the necessary voltage to overcome the HRS and the necessary energy to overcome the barrier of the insulating state. This same relationship has been observed in other systems including TMOs [96] [97].

5.3.3 Resistive switching in Sr_2IrO_4 over large areas

Similarly to the ones on $n=\infty$ phase, the sequences of C-AFM current maps were performed in the $n=1$ films with an "in situ" non-continuous layer of Pt NPs. The growth of these particles by PLD has been explained in the Chapter 3 and, as in the case of the SrIrO_3 , the NPs have a multiple role helping the stability of the current and protecting the film. In this case as well, all the writing and reading processes were carried out in a nitrogen rich atmosphere to remove the humidity and avoid surface oxidation processes.

Figure 5.8 (a) depicts the reading current map of a $50 \times 50 \mu\text{m}^2$ area of a 16 nm $n=1$ film after two sequences of writing. In the first one, a scan of $35 \times 35 \mu\text{m}^2$ was performed while the sample was biased at +4.5 V. This square coincides with the bright ring of the reading map characterized for a higher conductivity, which indicates that the area scanned has been switched into

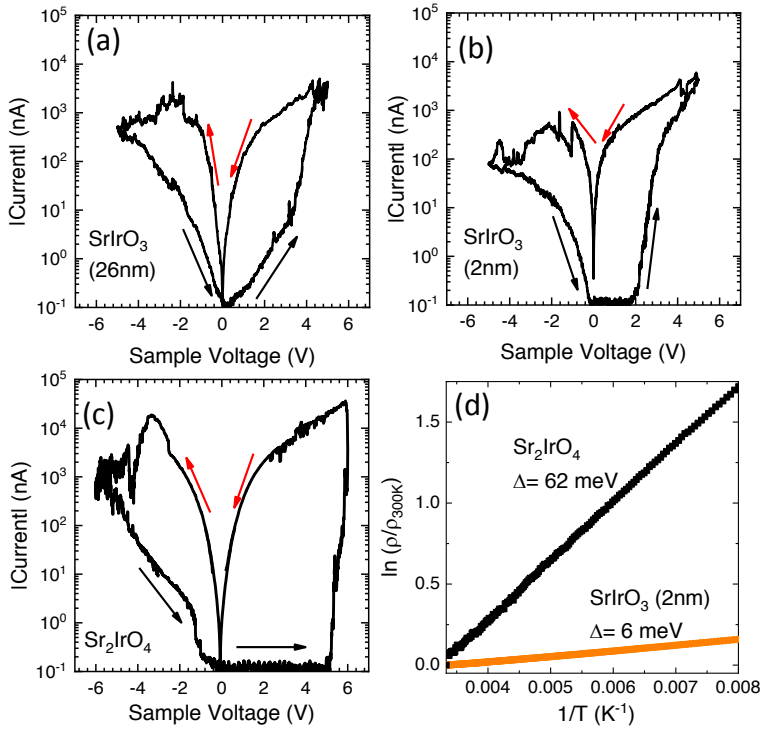


FIGURE 5.7: Comparison between the RS cycles of (a) semimetallic $n=\infty$ film, (b) an insulating $n=\infty$ film and a (c) film of $n=1$. The voltage thresholds in the positive branches only appear in the insulating films. (d) Arrhenius plot of the insulating films enhancing the differences in Activation energies. The magnitude of the threshold in the RS curves can be related to the activation energy of each film.

the LRS. In the second one, a scan of $20 \times 20 \mu\text{m}^2$ was carried out in the center of the previous one at -5 V. The scanned area can be identified in Figure 5.8 (a) as a dark square located in the center of the image. The rise of resistivity in the scanned area indicates that it has been switched into the HRS. Therefore, 3 states can be observed in Figure 5.8 (a): the pristine state as the exterior dark ring which has not been “written”, the LRS as a bright ring and the HRS as the central dark square. Figure 5.8 (b) depicts the topography image obtained simultaneously during the reading current map of Figure 5.8 (a). It can be observed that while the outer LRS ring does not produce any topological changes, the inner HRS square might suffer from minor modifications of morphology. In this square, and the area surrounding it, thin stripes can be noticed in the x direction. Unlike the case of the

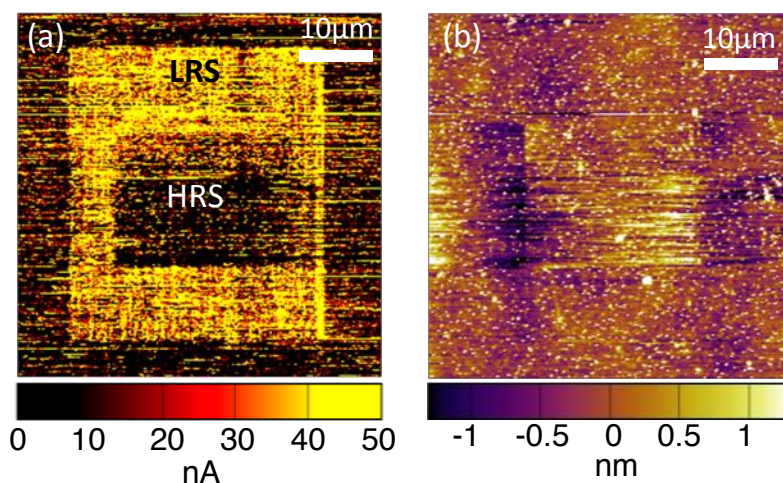


FIGURE 5.8: Current (a) and topography (b) images of a $50 \times 50 \mu\text{m}^2$ area in a Sr_2IrO_4 film. (a) Reading current map of the area where 2 previous writing scans have been performed: a $35 \times 35 \mu\text{m}^2$ scan at $+4.5 \text{ V}$ which has set the film into the LRS (bright squared ring) and a $20 \times 20 \mu\text{m}^2$ scan biased at -5 V which has reset the area into the HRS. (b) Morphology image of the current map showing minor changes of topography due to NPs dragging.

SrIrO_3 films, the affected zone does not show a different average height so the compression of the film can be ruled out as a possible explanation. It is worth noting that these stripes are in the same direction as the AFM probe indicating that some NPs could be being dragged during the reading scan.

Similarly to the measures performed in the section 1 with SrIrO_3 , several conclusions can be extracted from the current map. Firstly, the polarity of the switching is in fully agreement with the results of the I-V curves. While positive sample voltage induce the LRS, negatives ones can switch the system into the HRS. Secondly, the possibility of writing both HRS and LRS on large surfaces illustrates the robustness of the cycling from a statistical point of view. Finally, in the present current map the pristine state appear to be more similar to the HRS than to the LRS. To further study this issue, KPFM measurements were performed.

5.3.4 Resistive switching effect on the surface potential

Although C-AFM is the most used Scanning Probe Microscopy (SPM) technique to study RS in oxides due to its direct evaluation of the resistance, some reports [90] [98] [99] have used complementarily Kelvin Probe Force

Microscopy (KPFM) to characterize the RS behavior. KPFM measurements provide maps of the Contact Potential Difference (CPD) on the surfaces. In RS systems based on the change of ions valence, the CPD can be modified due to the resistivity switches, allowing to track the resistance states avoiding a direct interaction with the film. This method is therefore less aggressive than the current maps and do not suffer from the frequent current instabilities of the C-AFM. Moreover KPFM images offer complementary information of the film about these valence changes and the Fermi level modifications in the different states. In the present case of the Sr_2IrO_4 films, this technique also provides a better perspective to study the pristine state than the corresponding current maps, which will be discussed in the section 4 of this Chapter.

Figure 5.9 (a) shows a KPFM image of an equivalent $50 \times 50 \mu\text{m}^2$ area of the film with Pt NPs used in the previous current map. As in the previous case two writing scans have been performed before the depicted reading image. In the first one, carried out in a $35 \times 35 \mu\text{m}^2$ area, the film was biased at 5V leading the system into the LRS. This can be visualized in the potential map as the dark ring with the lowest CPD. In the second writing scan a $20 \times 20 \mu\text{m}^2$ of the sample was biased at -6V forcing it to switch into the HRS. The scanned area can be perceived as the bright square in the center of the image. In the present reading scan the three states can be visualized, being the HRS the one with more CPD, the LRS the one with lowest CPD and the pristine at an intermediate value. To appreciate better these differences, a transversal profile depicted as a green discontinued line in Figure 5.9 (a) has been plotted in Figure 5.9 (b). In order to observe the changes in the CPD with more clarity, ΔCPD is used taking the pristine state as the origin, as described in:

$$\Delta\text{CPD} = \text{CPD}_{\text{LRS/HRS}} - \text{CPD}_{\text{pristine}} \quad (5.1)$$

The profile presents the three states with stable variations of CPD. Since ΔCPD is defined with the origin in the pristine state this has an initial $\Delta\text{CPD} \approx 0$ meV. Once the scan of $+5\text{V}$ is performed the area is switched into the LRS and the ΔCPD is reduced to ≈ -50 meV. After the second writing scan at -6V the inner square is switched into the HRS increasing their ΔCPD in ≈ 300 meV (50 to 0 and 250 meV above the pristine state).

In order to study if the ΔCPD of the LRS can be modified by adjusting the writing scan voltages, a series of writing scans at different positive sample voltages were performed in different areas and were measured by KPFM. Figure 5.10 (a) depicts a reading scan of this series where a $50 \times 50 \mu\text{m}^2$ area at the center of which a previous $35 \times 35 \mu\text{m}^2$ scan has been carried

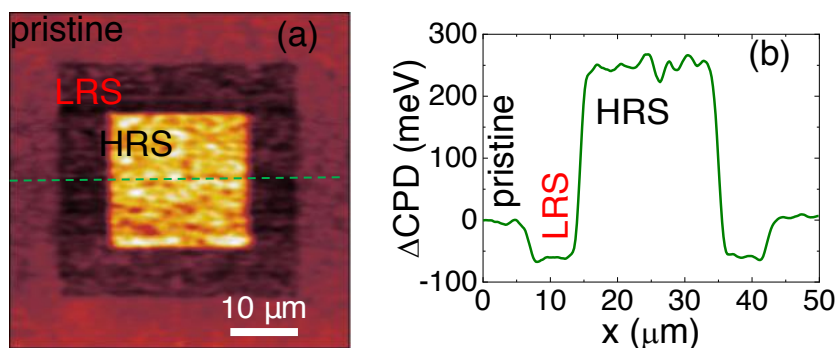


FIGURE 5.9: (a) KPFM image of a $50 \times 50 \mu\text{m}^2$ area of a Sr_2IrO_4 thin film. The three resistance states observed in C-AFM (pristine, LRS and HRS) present different CPDs. (b) Profile of the potential map showing more clearly the changes in CPD for the LRS and HRS.

out at + 4.5 V. In order to analyze more precisely the differences in ΔCPD , histograms of the LRS areas were performed for each writing voltage. One example of this methodology can be found in Figure 5.10 (b), where the histogram of the LRS switched by 6 V is depicted. Since the data is already shifted establishing the pristine state at 0, the value of the LRS peak represents directly the ΔCPD . The values of the LRS peaks for the different writing voltages are depicted in Figure 5.10 (c) where the error bars of the graph represent the Full Width Half Maximum (FWHM) of the LRS peaks in their respective histograms. With writing voltages of 3 V and 4 V there is a lack of contrast between the pristine state and the scanned area and therefore the histogram of the central part of the image coincides perfectly with the outer part of it. This is indicative that the writing scan has not been able to switch the system into the LRS and the value of ΔCPD is therefore 0. However as the writing voltage reaches 4.5 V a clear contrast appear in the scanned area whose histogram is shifted implying a switch into the LRS. As the writing voltage is increased to 5 and 6 V the ΔCPD keeps decreasing to more negative values, which is in well agreement with studies performed on other TMOs [90]. It is worth noting that the minimum value of writing voltage where a shift in the CPD occur (4.5 V) coincides perfectly with the threshold voltage observed in the I-V curves of Figure 5.6. This result reinforces the relation between the ΔCPD and the change in the resistivity of the film seen before. Moreover it clearly proves statistically the value of the voltage threshold to switch the film into the LRS.

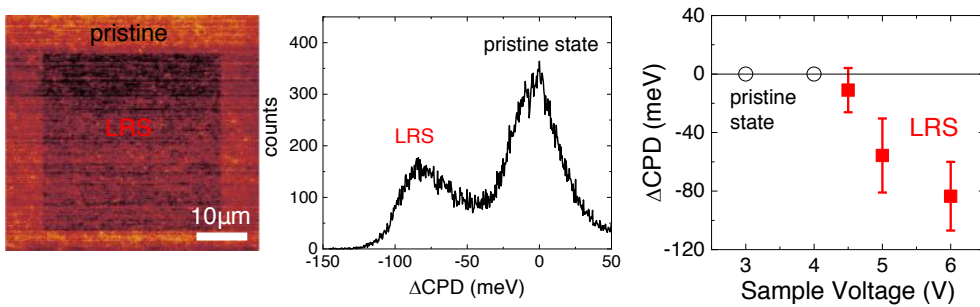


FIGURE 5.10: (a) KPFM image of a $n=1$ film with a covering of Pt NPs. The central square of the image has been previously scanned at 4.5 V switching this area into the LRS while the outer ring is in the pristine state. (b) Histograms of the pristine and LRS showing the shift in CPD due to the switching in the resistance. (c) Dependence of ΔCPD in the writing voltage of the switching. Only the voltages above the threshold of 4.5 V can switch the film into the LRS generating a change in the CPD.

5.4 Discussion on the Resistive Switching mechanisms

During the previous sections of this Chapter, the RS properties of the SrIrO_3 and Sr_2IrO_4 phases have been characterized. Nevertheless, the underlying mechanisms that give rise to such properties and the observed differences between films are not trivial and require a more profound discussion.

As it has been observed, all the studied films of the $n=\infty$ and the $n=1$ phases possess a bipolar RS with the same polarity which switches the film into the LRS by applying positive sample voltages and to the HRS with negative sample voltage. Due to these similarities the most probable scenario is that all the films have the same or very similar RS mechanisms.

5.4.1 Filamentary vs Interfacial type

As it is explained in the Chapter 2, RS can be roughly classified in two main mechanism groups: the filamentary RS and the interfacial RS. In the former group, a conductive filament between two metallic contacts is created in an insulating switchable material. To perform this type of switching the Insulating layer of the material must be sandwiched between two metallic contacts in a Metal-Insulator-Metal geometry. In the present case, an in-plane configuration of the C-AFM is used to measure the RS properties (Annex A), which implies a separation between the two metallic contacts in the order of millimeters. This distance is 5 or 6 orders of magnitude larger

than the usual thickness of the switchable layer (generally in the range of nanometers) and, thus, the voltage needed to switch the whole distance would be extremely large. Moreover in the case of the semimetallic films the insulating nature required for the filamentary type would not be satisfied. For these reasons, the filamentary type can be ruled-out of the possible mechanisms.

On the other hand, the interfacial RS type only switches the interface between the material and the electrode, but since the present measures are carried out by C-AFM they are perfectly detectable. Moreover, the initial state of the switchable material does not need to be insulating, which allows a wider diversity in the analyzed samples. Therefore, the interfacial RS seems to be a better approach to determine the mechanisms responsible for the observed RS characteristics. Additionally, similar studies in the same C-AFM configuration also invoke the interfacial mechanism to explain their RS behaviors [90] [91].

As explained in Background, there are several mechanisms in the interface type RS, such as the Vacancy based, the one based on electronic phenomena and the ferroelectric one. Since both the $n=1$ and the $n=\infty$ phases do not show any ferroelectric properties, the mechanism based on the ferroelectric polarization can be easily discarded. On the other hand, both the vacancy and the electronic and electrostatic types could be the responsible for the present mechanisms. In any case, most of the systems with mechanisms based in the electronic or electrostatic phenomena precise from vacancy incorporation or migration to explain the switching, thus, vacancies must be present in the switching process.

5.4.2 Mechanism of Switching in the $n=\infty$ phase

As pointed in the Background, the accumulation of oxygen vacancies in a specific place of the oxide induces the nearby ions to reduce their oxidation state to compensate the lack of anions and maintain locally the neutrality of the material. The additional electrons placed in the metallic cations can cause different effects in the electric transport according to the properties of the material. In systems where the electric transport is dominated by electrons, the additional electrons increase the density of carriers, thus, decreasing the resistivity of the material and inducing the LRS, while the HRS can be achieved by removing them from the interface. On the other hand, in materials where holes are the majority carrier, the extra electrons are considered as scavengers of the holes, thus, reducing the conductivity of the

material. In this case the HRS is achieved by the accumulation of vacancies, while the LRS can be induced eliminating them from the interface [15] [92] [100].

In the present case of the perovskite SrIrO_3 thin films, the dominance of electrons or holes is not clear yet. Although it is generally accepted that both holes and electrons are responsible for the $n=\infty$ phase transport properties, the identification of the majority carrier is currently under debate. On one hand, the reported Hall effect measurements [11] [45] [68] and the ones presented in the part of this thesis in the Chapter 4 point to an electron based system (due to their negative values of R_H). On the other hand, the values of the R_H are small and its combination with other reported measurements of Seebeck effect suggest that holes might be the dominant carrier [76]. This complex and delicate scenario could also be modified by variations in the stoichiometry of the film or by its proximity to the observed MIT, creating an even more complex situation. Due to the uncertainty regarding the principal electric carrier, two mechanisms driven by vacancies will be discussed to relate the observed RS characteristics with the motion of the oxygen vacancies.

Assuming that the electric transport is governed by electrons, the present I-V curves could be explained with a system of vacancy migration in the interface (Figure 5.11). If a positive Sample Voltage (SV) is applied to the system (negative biased tip) (Figure 5.11 (b)) the vacancies are electrostatically attracted to the interface increasing their concentration in that area. The increase of vacancy concentration produces an increment of electrons in the Ir^{4+} cations reducing their oxidation state and increasing their Fermi level due to addition of extra carriers, which increases locally the conductivity and switches the system into the LRS. Even after the biased voltage is reduced (Figure 5.11 (c)), the vacancies remain in the same position leaving a non-volatile LRS. The affected area can be switched back to the HRS by applying a Negative SV (positive tip voltage) which expels the vacancies from the interface (Figure 5.11 (d)). This reduces the accumulation of vacancies in the vicinity of surface Ir cations, lowering their Fermi level and its conductivity. Again, the changes in the vacancy distribution do not vanish after the voltage removal (Figure 5.11 (e)) and, hence, their electric properties neither.

Alternatively, if it is assumed that the transport properties of the $n=\infty$ phase are mainly dominated by holes, a redox reaction in the vicinity of the interface is needed to explain the switching. When a positive voltage is biased to the sample, the redox reaction 5.2 takes place in the interface of the SrIrO_3 film.

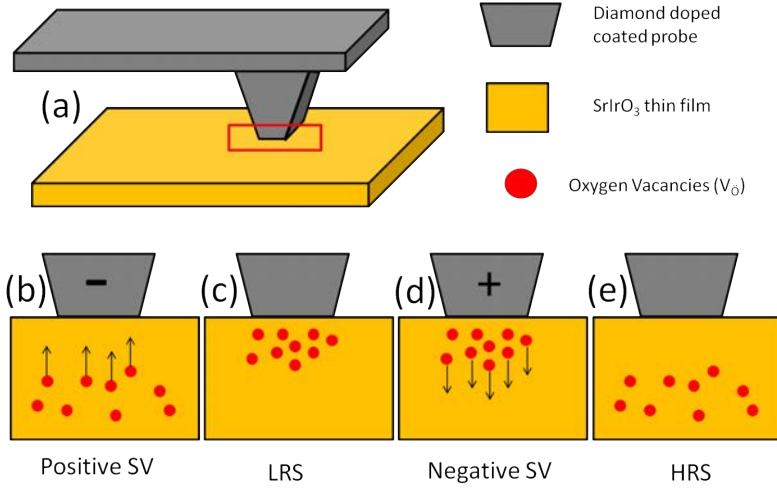
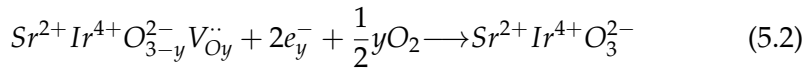
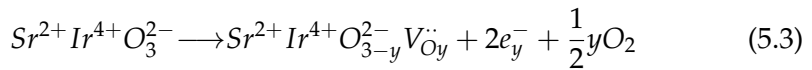


FIGURE 5.11: Mechanism of vacancy migration in $n=\infty$ films assuming the electrons as the principal carrier. (a) Sketch of the C-AFM measuring the film, indicating in a red square the area where the switching is produced. (b) Upon the application of positive SV the oxygen vacancies are attracted to the interface between the tip and the film. (c) Once removed the tension, the oxygen vacancies remain in the same position switching the affected area into the LRS. (d) If a Negative SV is applied, the vacancies are expelled from the interface. (e) After returning the bias SV to 0 the concentration of vacancies is diminished and the region is switched into the HRS.



In this process oxygen molecules of the atmosphere are incorporated into the film, filling the vacancies and removing them from the surface (Figure 5.12 (a)). The depletion of vacancies reduces the Fermi level and switches the area into the LRS, which is maintained after returning the voltage to lower values (Figure 5.12 (b)). This step can be reversed by biasing the sample with negative voltage, which induces the reverse redox reaction 5.3.



In this way, oxygen molecules are created from the oxygen anions of the film, leaving behind vacancies that increase the resistivity of the system (Figure 5.12 (c)). Once the voltage is removed the vacancies remain in the

interface and the affected area is switched into the HRS (Figure 5.12 (d)). This mechanism has been described in other oxides whose electric transport is dominated by holes [92] [100].

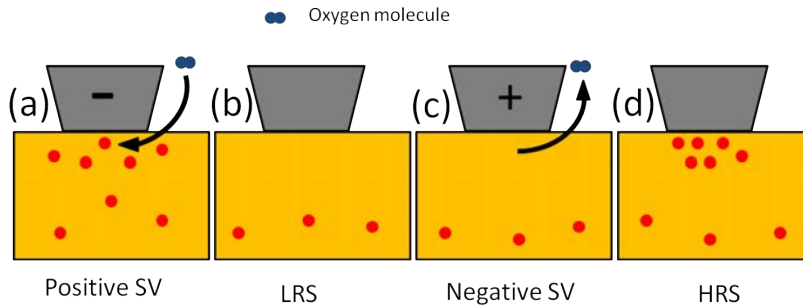


FIGURE 5.12: Mechanism of redox processes in SrIrO_3 films assuming that holes are the main carriers. (a) Oxygen incorporation to the interface, which removes the existent vacancies. (b) The depletion of the vacancies switches the area into the LRS in a non-volatile way. (c) Biasing the sample with negative Voltage, oxygen molecules can be liberated from the oxygen anions of the film. (d) This process leaves vacancies in the interface that turn the affected area into the HRS.

5.4.3 Differences between the semimetallic and insulating SrIrO_3 films

Both of the above mechanisms can explain the observed results in both the insulating and semimetallic films. Nevertheless, there are remarkable differences between the I-V curves (Figure 5.4) that suggest that the effect of the vacancies may be slightly distinct for the different films. As it has been extensively studied in the Chapter 4, the 2 nm $n=\infty$ thin films behave as strongly disordered materials (Anderson Insulator) which means that the Fermi level lies on a localized states area inside the band structure. These localized states are separated from the extended ones, which can contribute to the conduction, by a mobility edge (E_c). Moreover the possible contribution of electron correlation would also start to open a small band gap in the band diagram. On the other hand, thicker semimetallic films have a continuity of states with a band structure that sometimes has been described as a Dirac cone or a lifted Dirac cone [101] [102]. In any case, the differences in the band structure seem to be the root of the different RS behaviors.

One of the most noteworthy differences between the films is the apparition of a threshold voltage around ≈ 2 V in the insulating ultrathin films

while in the thicker semimetallic ones a smooth continuous increase of current can be observed. Figure 5.13 represents the band structure of both films and the changes in the Fermi level according to the carrier model and the existence of localized states. In this Figure it can be observed that for the semimetallic films (26 nm) the absence of localized states allows the shifts of the Fermi level to follow a continuous of extended states. In the case of the electron-like transport presented in Figures 5.13 (a) and (b) the increase of the Fermi level promoted by the higher concentration of vacancies drives the system into with higher DOS associated with the LRS. Similarly, if holes are considered as the major carrier (Figures 5.13 (e) and (f)), the decrease in the number of vacancies decrease the Fermi level, finding as well a state with higher DOS in the LRS.

In the 2 nm insulating film, the shift in the Fermi level operates similarly for the electron's (Figures 5.13 (c) and (d)) and hole's (Figures 5.13 (g) and (h)) assumptions. Nevertheless, the presence of localized states (marked in red) prevents the current to flow until the mobility edge can be overcome. Thus, below threshold voltage, the current remains near 0, and once it is surpassed it increases rapidly, in contrast with the smooth increment (without threshold) of the semimetallic films.

Moreover, the repeatability of the cycle seems to be also a key difference between the films. In the case of the 2 nm thin film, the good repeatability of the cycles can be related with a sharper separation between the localized and the extended states, which creates a stable switching between two very well defined states (HRS and LRS). On the contrary, the semimetallic 26 nm film presents more variability in the cycles. This is caused due to the absence of any specific barrier that must be surpassed to switch and, thus, a continuous of states can be achieved. In this multi-level paradigm, the HRS and the LRS labels are more approximated and can change from one cycle to other causing the observed greater variability.

The general mechanism of the semimetallic thicker films could be described, therefore, as a vacancy type RS while in the case of the insulating ultrathin films this mechanism is supported by the proximity to the MIT, which makes the cycles more defined and with a clear threshold. Moreover the current maps presented in section 1 suggest that the pristine state of the thick semimetallic films resembles more the LRS than the HRS.

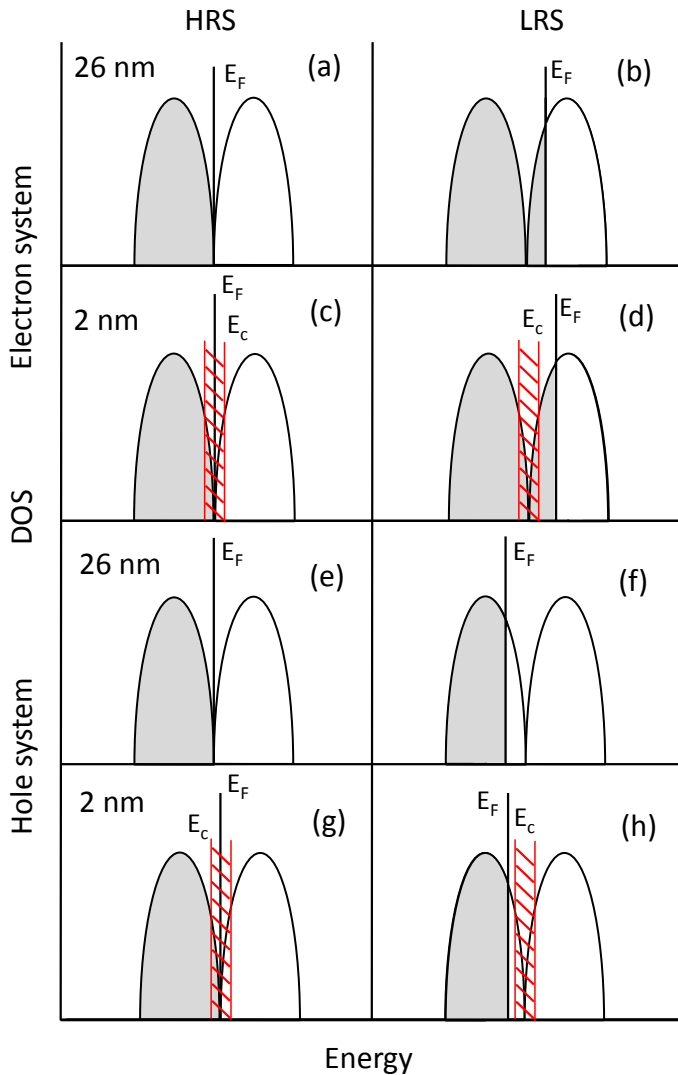
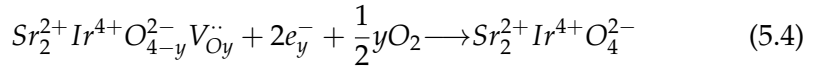


FIGURE 5.13: Sketch of the band structure in both 26 and 2 nm SrIrO₃ films. The variations in the Fermi level due to the RS induce the LRS and the HRS for the two possible carrier assumptions. (a) and (b) depict the switch in a semimetallic film assuming electrons as the dominant carrier. (c) and (d) show the same transition in the 2 nm film. The marked red area represents the localized states limited by the mobility edge (E_c). (e) and (f) illustrate the transition in a 26 nm film where the main carriers are the holes. (g) and (h) reproduce the same switch in the 2 nm insulating film with the energy levels near the Fermi level are localized.

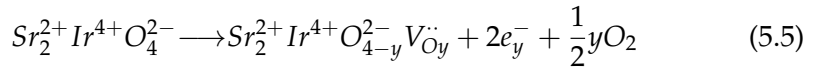
5.4.4 Mechanism of Switching in the n=1 phase

In the case of the Sr_2IrO_4 films, it is widely accepted that holes are the main transport carriers as observed in Hall effect and Seebeck effect measurements [49] [51]. This reduces the complexity of the problem, since only the mechanisms compatible with a hole-like transport can be considered.

Since in these films the polarity of the switching, for both the HRS and the LRS, is the same as the one of the $n=\infty$ films only the mechanism involving the redox reaction can be the responsible for the vacancy RS. Similarly to the hole-like case of the SrIrO_3 films (depicted in Figure 3.12), when a positive voltage is biased to the probe, the redox reaction 3.4 takes place in the interface of the film:



This reaction fixes atmosphere oxygen to the interface, depleting the vacancies of the area in contact with the tip. The diminution of vacancies decreases the Fermi level, which increases the conductivity switching the area into the LRS. Conversely, the transition to the HRS can be performed by applying negative SV and inducing the reverse redox reaction 3.5:



In this reaction the oxygen anions of the film are oxidized and oxygen molecules are released to the atmosphere leaving vacancies in the affected interface. The vacancies act increasing the Fermi level and, thus, decreasing the conductivity of the area.

The implications of this mechanism in the band structure can be observed in Figure 5.14. Due to the Mott insulator nature of the Sr_2IrO_4 films, a band gap is opened in the $J_{eff}=1/2$ band of the iridium. Similarly to the case of the ultrathin $n=\infty$ films in the HRS the Fermi level lies in a zone without conductive states (Figure 5.14 (a)). The depletion of vacancies can decrease the Fermi level shifting it below the energy gap into the LHB (Figure 5.14 (b)). In this case the Fermi level also needs to overcome an energy barrier to reach conductive states and, as a consequence, a threshold voltage appears in the I-V curves at $\approx 4.5\text{V}$.

The KPFM measurements depicted in Figures 5.9 and 5.10 of this Chapter corroborate the presented redox based mechanism. An increase (decrease) of the CPD can be directly related to a decrease (increase) of the sample's workfunction (see Appedix A) which is the consequence of an increase (decrease) of the Fermi level. Assuming that the shifts in the Fermi level are caused by the changes in the concentration of oxygen vacancies, an

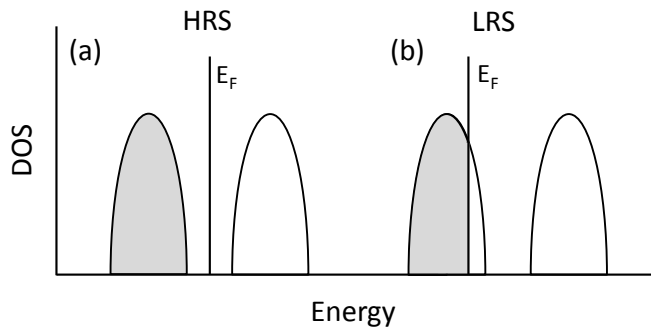


FIGURE 5.14: Sketch of the band structure for the $n=1$ films for the two different resistance states. (a) HRS where the Fermi level lies into the energy gap. (b) after the switch to the LRS the Fermi level is shifted to lower values overcoming the gap and reaching the LHB.

increase (decrease) of the Fermi level would mean that more (less) electrons are placed on the Iridium cations which could be related with a vacancies concentration increase (decrease).

In the HRS, which is obtained applying negative Voltage, the CPD is increased which means a shift of the Fermi level towards higher values and consequently an increase of the vacancies concentration. On the other hand, in the LRS, the reduction of the CPD implies a decrease of the Fermi level and a reduction in the number of oxygen vacancies. The increase of the local conductivity (LRS) due to the lower number of vacancies and the increment of resistivity (HRS) due to a larger number of them are indicative of a hole-like conductivity. Therefore both the C-AFM and the KPFM measurements are congruent with each other, with the reported articles about the hole-like nature of the $n=1$ films [49] [51] and the presented redox mechanism.

Nevertheless, the pristine state of these films is not fully understood. On one hand, the current map depicted in section 3 suggests that the initial state of the film resembles more to the HRS than to the LRS. On the other hand, the presence of vacancies in the system would be the responsible for the HRS in the film. According to this, a complete absence of vacancies in the system would lead to the LRS and the Fermi level would be situated outside the gap created by the electron correlation. This is contradictory to the insulating nature of the $n=1$ phase in its most unaltered form. A possible explanation for the observed measurements would be that a certain amount of cationic vacancies (either Sr^{2+} or Ir^{4+}) are present in the films from the deposition. With this new scenario some initial oxygen vacancies would induce the observed insulating pristine state. Once the oxygen

vacancies are depleted, even beyond the equivalent for the existent filled cation positions, a net hole doping would be induced into the system leading the material into the LRS by shifting the Fermi level below the gap. The addition of more vacancies to the system would therefore lead the system into a more resistive state (HRS). This scenario would be in a good agreement with the KPFM measurements since the CPD of the pristine state does not coincide with the CPD of the HRS. The increment of the ΔCPD in the HRS suggest that it possesses more vacancies than the pristine state, thus, situating the resistive initial state of the film halfway from the LRS and the HRS. In any case very accurate local composition measurements, for example Photoemission electron microscopy, would be needed to elucidate this hypothesis.

Chapter 6

Conclusions

In the present thesis the Resistive Switching properties of iridate thin films have been studied. The main results obtained in this thesis can be split in 3 different parts:

The main conclusions that have resulted from the Chapter 3, which was dedicated to the iridates growth, are:

- The depositions of strontium iridates by sputtering present a preferential growth towards the perovskite SrIrO_3 phase, even accommodating variations in the stoichiometry. This is the result of a kinetic controlled scenario where a large resputtering takes place at high temperatures.
- The SrIrO_3 films grown by sputtering are flat, stable, homogeneous and possess a high level of crystallinity.
- The morphology of the films can be tuned kinetically to obtain 3D nanostructures. Moreover, these nanostructures can be ordered following the terraces of the underlying substrate.

The principal conclusions of the macroscopic electrical transport contained in the Chapter 4 are:

- Thickness dependent metal-to-insulator transition driven by disorder is observed in SrIrO_3 films. Thick films, above 3 nm, are semimetallic with signature of the MIT at low temperatures due to weak localization.
- An abrupt transition to fully insulating behavior attributed to Anderson localization occurs for 2 nm films exhibiting strong negative magnetoresistance at low temperatures.
- This transition is also present in nanostructured films but with a softened evolution with the thickness.

The Conclusions of the Resistive Switching part of results (Chapter 5) are:

- Both SrIrO_3 and Sr_2IrO_4 phases possess a bipolar Resistive Switching that promotes the Low Resistance State with sample positive voltages and the High Resistance State with negative sample voltages.
- The semimetallic thick SrIrO_3 films present a smooth transition between HR-LR states with a poor reproducibility of the cycling.
- In thin insulating SrIrO_3 films, the switching occurs at a well-defined threshold voltage at 2 V with good reproducibility.
- The insulating Sr_2IrO_4 films showed a similar behavior with a higher threshold at 4.5 V indicating a relationship between the insulating energy barrier and the voltage threshold.
- The switching has been attributed to a valence change mechanism based in the oxygen vacancies motion (or creation). In the case of the semimetallic films the smooth Resistive Switching behavior is the consequence of shifting the Fermi level inside a band. On the other hand, in the insulating films an energy barrier has to be overcome to achieve the Low Resistance State, thus, generating a sharp threshold.

Finally, the present thesis has proved a novel Resistive Switching effect in high quality Iridate thin films and its feasibility for ReRAM memories. Moreover, it has been observed that the switching features of these oxides can be tuned by the presence of Metal-Insulator Transitions. These results have already been published in Peer-Review Journals of high impact and have been selected as a key innovation by the European Commission. (<https://www.innoradar.eu/innovation/36215>)

6.1 Further work

The exposed results and conclusions can lead to different possibilities for further research:

- The origin of the preferential growth for the SrIrO_3 film deposited by sputtering is still an incognita. Although the role of resputtering has been already signaled the exact mechanisms that prevent the formation of other Ruddlesden-Popper phases remain unknown.
- The ability to achieve nanostructured film surfaces needs to be further exploited to tune the physical properties.

-
- The temperature dependence of the resistivity in the semimetallic SrIrO₃ films as well as the negative magnetoresistance in insulating films are still open questions. In particular, it could be interesting to deeply study their connection with the disorder.
 - Resistive Switching properties should be explored when Metal-Insulator transitions are achieved by other routes as for example, strain or in other systems, as nickelates.
 - Further insights in the Resistive Switching mechanisms in oxides should be acquired by combining C-AFM and KPFM measurements.

Appendix A

Experimental Techniques

From the deposition of thin films to the electric characterization, many different experimental techniques and procedures have been used in this Thesis. This appendix pretends to provide an overall vision of all the techniques employed in the course of this Ph.D. thesis allowing the reader to understand the basics of each one.

A.1 Thin Film deposition techniques

The samples studied in this work were grown by Physical Vapor Deposition (PVD) techniques, in particular, Pulsed Laser Deposition and Plasma Assisted Physical Vapor Deposition.

A.1.1 Plasma Assisted Physical Vapor Deposition (Sputtering)

Plasma Assisted Physical Vapor Deposition (also known as Sputtering) is a technique in which the surface atoms of a target are vaporized due to the momentum transfer of bombarding plasma ions [103]. Figure A.1 (a) presents a scheme of a sputtering system. The system consists of two electrodes connected to a bias Voltage which are separated by a gas atmosphere. A target of the material that is intended to deposit is placed on the Cathode. In the Anode a heater controls the temperature of the deposition. The distribution of a sputtering chamber can be observed in a picture in Figure A.1 (b). The simplest case for sputtering is the DC configuration in which a constant Voltage is applied between the Cathode (-) and the Anode (+). The whole process of deposition of DC Sputtering is depicted in Figure A.1 (c). In the first place free electrons are ejected from the cathode to the anode due to the applied electric field (1) in what is called a discharge process. Accelerated electrons can collide gas molecules near the cathode generating cations and more free electrons (3). This mixture of gas neutral atoms, electrons and ions is known as plasma. Since each collision generates a new electron, this

effect is reproduced in cascade needing just a small amount of starting collisions to create stable plasma. The positive ions of the plasma are then accelerated to the cathode due to the applied electric field (4). These ions bombard the target causing the ejection of neutral atoms by momentum transfer (5). These neutral atoms are finally deposited in the anode where they can grow as a thin film (6) [104]. As can be observed in Figure A.1 (d), plasma can be visualized by a particular glow which is caused by the energy release of the recombination between free electrons and positive ions of the plasma [104].

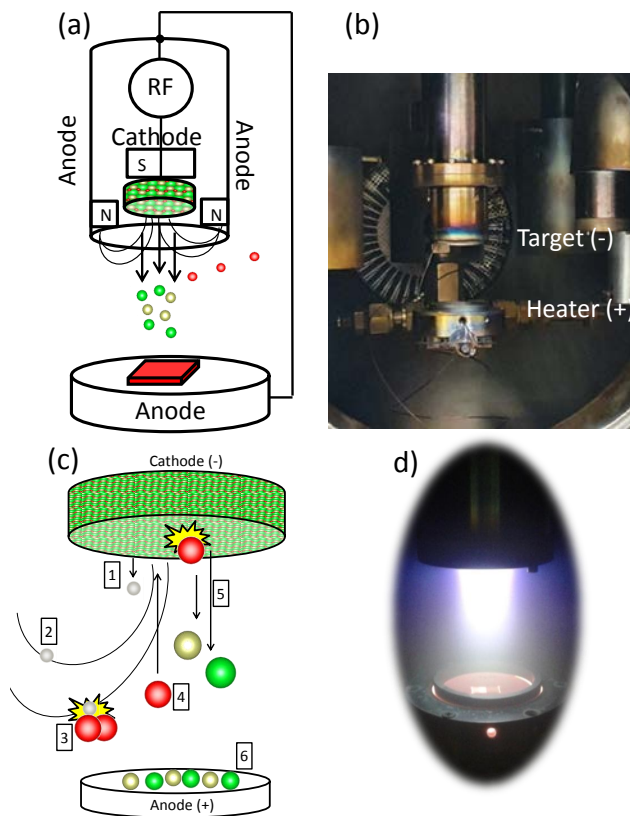


FIGURE A.1: (a) Complete scheme of a RF magnetron sputtering. (b) Photography of the employed Sputtering chamber. (c) Scheme of a magnetron sputtering process. (d) Picture of the deposition of a material in DC sputtering. The visible violet glow on the superior electrode is the plasma generated by the electron discharge.

The process of sputtering must be performed on a chamber with a pressure atmosphere usually ranging from 10-200 mTorr. A very low pressure

will reduce the probabilities for an electron to collide with a gas particle thus preventing the formation of plasma. On the other hand, a very high pressure will increase excessively the collisions and the electrons will not have enough energy to ionize the gas in the chamber, therefore the plasma will not be generated as well [104].

The energy of the accelerated ions is also crucial for the process. Energies should be close to 20 eV, otherwise, other phenomena as condensation or implantation will dominate the process of impact of the ion on the target and subsequently the rate of deposition will decrease [104].

Even fulfilling all these conditions, DC sputtering presents several drawbacks. The most limiting one is the lack of capability to use insulating targets. When the target is not conductive, the current flow is reduced and the discharge process does not take place, charging the insulating target and therefore blocking the sputtering process [105].

In order to avoid this problem, a Radio Frequency (RF) Voltage source is used instead of the constant Voltage one, in what is called RF Sputtering. In this variant, a radio frequency voltage (usually of 13.56 MHz) is applied to the target electrode. As is depicted in Figure A.2, in the course of a complete cycle two different parts can be distinguished. When the electrode is at positive Voltage it collects electrons coming from the discharge of the other electrode while at negative polarities ions are accelerated towards the target [106]. Since the electron current at every cycle is larger than the positive ions one, in the first cycles the target is charged to negative voltage values until it reaches a position (V_{bias}) where the currents are balanced [105]. Is worth noting also that at these frequencies only the electrons can follow the changes in potential, the positive ions, on the other hand, are more massive and there is not enough time to reverse their acceleration to the target. Due to this the growing film in the other electrode does not suffer from "backsputtering" and can grow in more favorable conditions [104].

The deposition rate in both RF and DC Sputtering techniques is usually too low. One possible solution to overcome this problem is the employment of Magnets in what is called Magnetron Sputtering. Placing magnets in a certain configuration a magnetic field can be created around the target. This magnetic field traps free electrons and force them to move close to the target (Figure A.1 (c) (2)). This confinement of the electrons increase highly their probability of collision with gas molecules incrementing the ions collisions with the target and the deposition rate. Moreover magnetron sputtering traps the emitted electrons near the target, and therefore, avoids the bombarding of the substrate which can cause heating and damage to the film [103] [105]. A non-commercial Sputtering was employed for most of the depositions carried out in this thesis. The sputtering, which is located in the

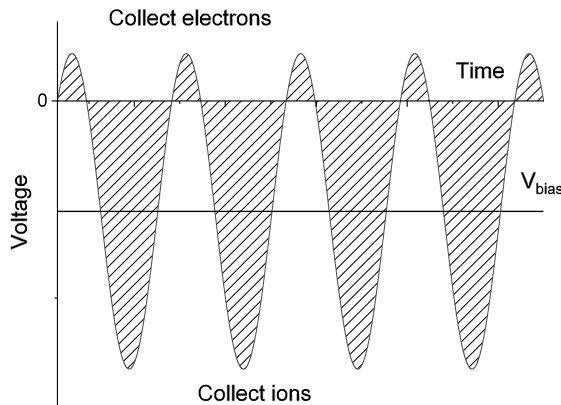


FIGURE A.2: Balanced state of a RF sputtering potential. In this image it can be observed that the Voltage is biased to negative values due to the electron current is larger than the ion current in an unbiased cycle.

ICMAB, possess several magnetrons that can be used alternatively in DC or RF mode. The chamber can operate with Oxygen or Argon and, moreover, the combination between the pressure sensors and a vacuum turbo pump allows selecting a determined pressure with a precision of 1 mTorr approximately in the range of 1 to 200 mTorr, which are the usual range pressures during the deposition. The Heater where the samples are deposited consists on an electric resistance connected to a thermocouple that can sense the temperature with 1°C of sensibility. The combined temperature system allows performing depositions between room temperature and 900°C .

A.1.2 Pulsed Laser Deposition

Similar to Sputtering, in Pulsed Laser Deposition (PLD) the target atoms are expelled and deposited on a substrate, but in this case, instead of a plasma source the vaporization is due to the action of laser pulses. In PLD systems a target with the same (or similar) composition of the material that is planned to deposit is placed in front of the substrate where the film is intended to grow. An optical system focuses an excimer UV Laser on the target and through the action of pulses the photonic energy of the laser is used to vaporize atoms from the target. When the power density of the Laser surpasses a certain threshold (which depends on the target material and the laser wavelength among others) the photonic energy is absorbed. This energy is then transformed into electronic excitation of the target atoms and transferred to the lattice heating at a local scale the target. The heated atoms

are vaporized from the target creating a mixture of neutral atoms, ions and electrons (among others) known as plasma plume. Finally neutral atoms of the plume are recondensed on the substrate, forming a thin film [107] [108]. In this thesis a commercial PLD workstation from "Surface" (located at the ICN2) was used for the depositions of the n=1 phase. This equipment allows performing depositions from room temperature to 850 °C in a controlled atmosphere of oxygen, argon or a mixture of both gases. The employed laser was a KrF excimer laser with $\lambda=248$ nm wavelength and the specific depositions carried out in this thesis had a spot size of 6mm² and an energy fluence of 1.25 J/cm².

A.2 X-Ray based Techniques

During this thesis different techniques based on X-Rays have been used to evaluate the structural properties, the thickness and the composition of the thin films.

A.2.1 θ - 2θ Measurements

θ - 2θ scans are one of the most common measurements in the X-Ray diffraction (XRD) field. In thin films, they are employed to identify the present phases in the sample (film and substrate materials) as well as their crystal quality. In these measurements an incident X-Ray beam (of λ wavelength) is focused on the sample at an angle θ (from the plane of the sample) while the detector is placed at an angle 2θ (from the incident beam) with the aim to collect the sample's diffracted beam. The system scans the angle θ while the detector makes the coupled movement in 2θ (Figure A.3 (a)). When a crystallographic plane of the sample (with an interplanar distance d and miller index (hkl)) fulfills the Bragg's condition (eq. A.1) a diffracted peak is detected.

$$\lambda = 2d_{hkl} \cdot \sin\theta \quad (\text{A.1})$$

In θ - 2θ measurements, only the planes parallel to the sample surface can be detected. On one hand, in a non-oriented polycrystalline powder sample, all the peaks that not suffer systematic extinctions can be detected. Since each grain is randomly oriented, statistically there will be a portion of the grains in the correct position to receive and diffract the X-Ray beam (Figure A.3 (b)). On the other hand, in an epitaxial thin film only the planes parallel to the surface of the film (Symmetrical reflections) can be detected [75][109].

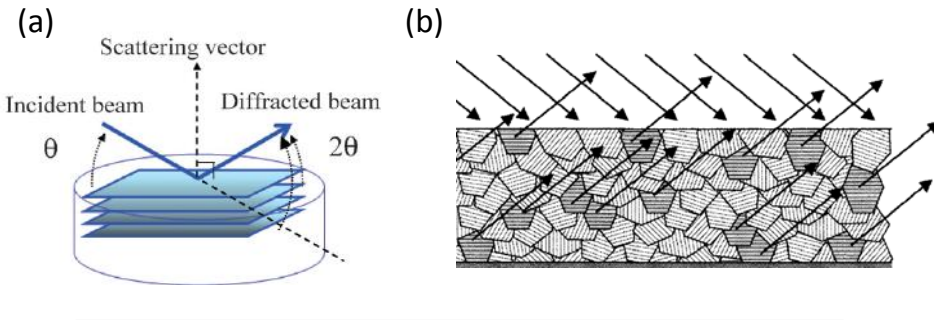


FIGURE A.3: θ - 2θ measurements. (a) Scheme of the geometry on a θ - 2θ scan showing the scan direction of the angles [110] (b) Scheme of the diffraction on a polycrystalline sample. It can be noticed that while all the marked planes are the same, only the ones parallel to the surface of the sample can diffract the incident beam [111].

A.2.2 Reciprocal Space Mapping

In order to measure the planes of an epitaxial thin film that are not parallel to the surface (Asymmetrical reflections), the incident x-ray beam is focused into the sample from a very small angle (Figure A.4 (a)). In this geometry, planes with an in-plane component can be reached and detected. These planes can be studied with a measurement called Reciprocal Space Mapping (RSM). In RSM, the angle between the crystallographic plane and the detector (ω) is kept constant (in a stepwise) while the angle between the plane and the diffracted beam (2θ) is scanned. The resultant matrix of intensities can also be plotted as a function of reciprocal vector components (Q_x , Q_y and Q_z) representing a slice of the reciprocal space (Figure A.4 (b)). The conversion from the angle based components to the reciprocal vector coordinates can be performed using equation A.2 and A.3 [111][75].

$$Q_x = \sin\theta \cdot \sin(\omega - \theta) \quad (\text{A.2})$$

$$Q_z = \sin\theta \cdot \cos(\omega - \theta) \quad (\text{A.3})$$

Since the measured reflections can be asymmetric, one can obtain in-plane information with this technique.

A.2.3 Pole Figures

In addition to the identification of phases in a sample and the evaluation of the crystal quality, X-Ray Diffraction can also be used to evaluate the

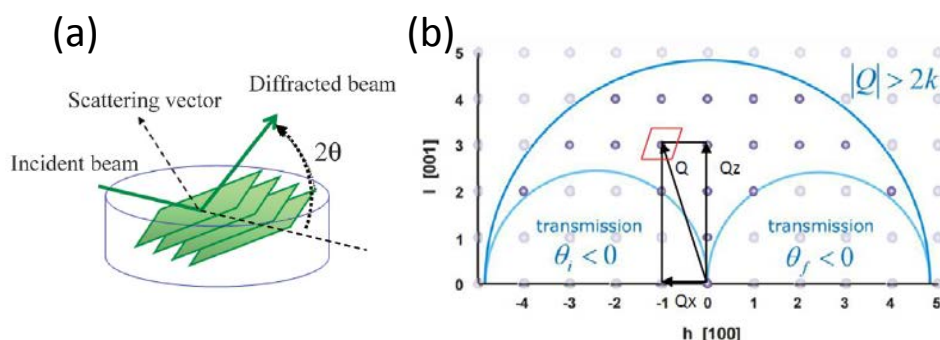


FIGURE A.4: Scheme of the diffraction of a plane not parallel to the sample's surface. It can be observed that the incident beam penetrates to the sample with a very small angle. [110] (b) Scheme of the Reciprocal Space. The area scanned in a RSM of a reflection would be the red rectangle at a certain coordinates of the Reciprocal vectors Q_x and Q_z [112].

crystal orientation of a sample in a technique called Pole Figure. In these measurements the sample and the detector's angle (ω and 2θ) are placed to measure one specific Bragg's reflection. Then two new angles are scanned to collect all the possible orientations of this reflection. These angles are ϕ and ψ , which are depicted in the Figure A.5 (a). ϕ is the rotation along the sample's normal direction and allows to collect the different in-plane orientations. On the other hand, ψ is the tilting angle and collects the different tilting orientations from the normal of the sample crystals. Pole Figures are usually represented in a stereographic, as the one depicted in Figure A.5 (b) [111].

A.2.4 X-Ray Reflectometry

Besides the crystallographic characterization by diffraction, material diffractometers can also use the reflection phenomenon to evaluate the thickness of thin films, in what is known as X-Ray Reflectometry (XRR). In these measurements the thin film is scanned in a θ - 2θ scan at grazing angles. Considering the case of a single film on a substrate, the incident X-Ray beam would be splitted into two when arrives to the films surface. Part of the radiation will be reflected (according to Snell's law) at the surface of the film while the other one will penetrate up to the substrate and will be reflected in the interface between the film and the substrate. Therefore two X-ray beams with the same λ will be reflected at the same angle (Figure A.6 (a)). This

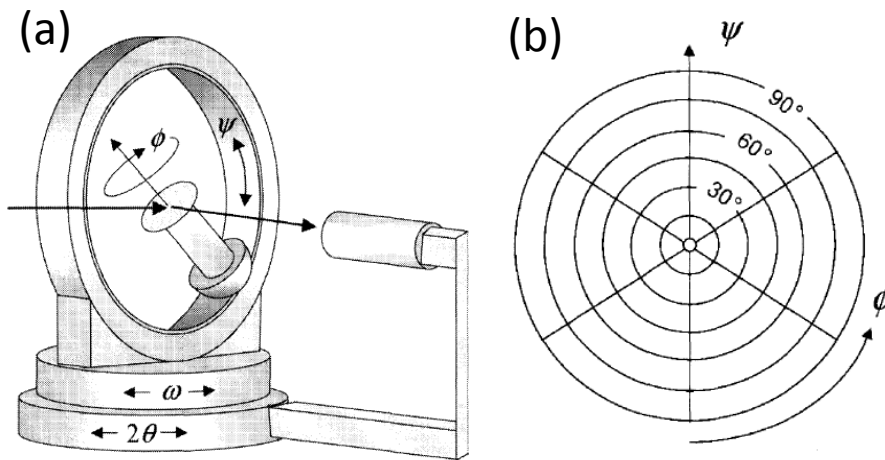


FIGURE A.5: (a) Scheme of the different angles used in the X-Ray diffraction techniques in a 4 circle diffractometer. (b) Pole Figure stereographic projection. The two angles used to collect the different orientations (ϕ and ψ) are depicted in it[111].

will cause an interference pattern of minimum and maxima that will depend on the incident angle (θ), the wavelength of the radiation (λ) and the thickness of the film (t) (Figure A.6 (b)) [113][111].

There are several methods to calculate the thickness of the film from the interference pattern. In this work equation A.4 has been adjusted to obtain a value of t . First the minima of the oscillations (θ_n) pattern are measured and added to the equation. These minima must be consecutive to be assigned to an index value (n). With these data the equation can be adjusted to obtain a value of thickness.

$$\left(\frac{\sin(\theta_n)}{\lambda}\right)^2 = \frac{(n + n_0)^2}{t^2} + \frac{1}{d_0^2} \quad (\text{A.4})$$

The term n_0 represents the initial index value while d_0 corrects the errors on the θ_n measurements.

Every technique explained above requires from specific characteristics of the diffractometer to be performed. In the present thesis the high resolution θ - 2θ scans were carried out in a PANalytical X'PERT PRO MRD system (ICN2) with a 2θ step size of 0.01° in the range of 36 to 49° . On the other hand, the low resolution scans were performed in a D-5000 diffractometer from Siemens (ICMAB) in the 2θ range from 5 to 120° and with a step of

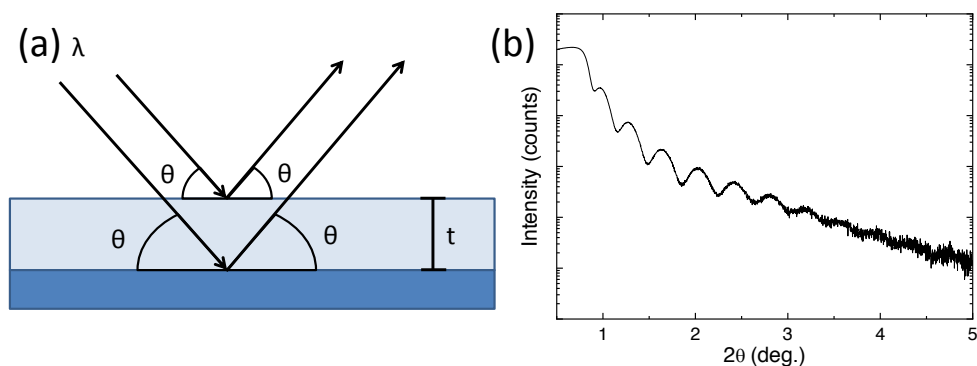


FIGURE A.6: Scheme of the X-Ray Reflectometry measurement, in which an incident X-Ray beam is reflected in both the film and substrate and generates an interference pattern that can be used to calculate the thickness of the film. (b) Example of a reflectometry performed in a 21 nm SrIrO₃ film on a SrTiO₃ substrate. The position of the maxima and minima can be used to determine the film thickness.

measurement of 0.02° . Part of the RSMs were performed in a PANalytical X'PERT PRO MRD (ICN2) system with step sizes of 0.03° in 2θ and 0.03° in ω . The rest of the RSMs were carried out in a Bruker D8-Discover (ICMAB) with a step size of 0.01° in 2θ and 0.034° in ω . On the other hand, the Pole Figures were measured in a Bruker D8 Advance (GADDS), located in the ICMAB, taking advantage of its area detector which takes, in the ones of this thesis, the reflections between 20° and 50° in 2θ . Finally, all the reflectometries performed during the course of this thesis were carried out in a D-5000 diffractometer from Siemens, at the ICMAB, with measurements ranging from 0.5 to 5° in 2θ and a step of 0.002° . Moreover, the analysis of the thickness was performed using the program XRR-thickness.

A.2.5 X-Ray Photoelectron Spectroscopy

Additionally to the explained techniques of XRD and XRR, X-Rays can be used with compositional analysis proposes. This is the case of the X-Ray Photoelectron Spectroscopy (XPS) where the photoelectric phenomenon is employed to determine the surface composition of a sample. First the generated X-Rays undergo to a process of monochromatization and are focused on a sample (Figure A.7 (1)). Then, the energy of the photons is transmitted to the material, ionizing core-shell electrons of the atoms (Figure A.7 (2)) in what is call the photoelectric effect. Although the X-Rays can penetrate up

to several microns into the material, the mean free path of the ionized electrons is short enough inside the material to ensure that the signal from these electrons only comes from the few first atomic layers of the material. Every expelled electron possesses a kinetic energy (E_K) that can be described as equation A.5:

$$E_K = h\nu - E_B \quad (\text{A.5})$$

Where $h\nu$ is the energy of the X-Ray photon that has ionized the electron and E_B is the binding energy of its orbital of origin. Since the X-Ray beam is monochromatic, the resultant E_K will depend only on the binding energy of the orbital. The electrons that are able to escape from the material are collected then by an energy analyzer, which only allows passing those electrons with a certain kinetic energy while measuring their current (Figure A.7 (3)). Knowing the frequency of the incident beam and the workfunction of the spectrometer one can determine the E_B of the original orbitals and, sweeping the selected energies, a complete spectrum can be obtained. Since every atom has a characteristic pattern spectrum, the surface atoms can be identified and quantified by measuring the areas of the signal and applying the appropriate correction factors. Therefore the stoichiometry of the surface can be measured with a good range of precision [114][115].

In the present thesis the analyzer used was a Phoibos 150 from SPECS (ICN2). To characterize the films first an overview scan in the range from 0 to 1380 eV was performed to analyze the possible presence of contaminants. Afterwards the most relevant and isolated peaks were analyzed in more accurate scans to study the surface composition. These peaks were the 3d of the Strontium, the 4f of the iridium, the 1s of the carbon, the 1s of the oxygen and the 2p of the titanium.

A.3 Scanning Probe Microscopies

Atomic Force Microscopy (AFM) and its variants have been employed for the morphology and the local properties characterization of the films studied in this thesis. In particular Conductive Atomic Force Microscopy (C-AFM) has provided the most relevant results in Chapter 5.

An AFM system is depicted in Figure A.8 (a). In this scheme it can be observed a nanometric tip attached to a cantilever and in contact with the sample. A laser is focused on the cantilever and the reflected light goes to a photodiode which is connected to a Feedback System (FS) that controls a set of XYZ piezoelectrics.

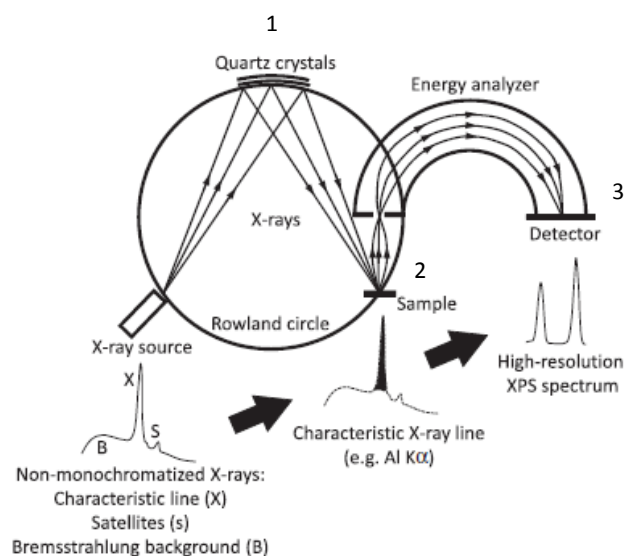


FIGURE A.7: Process of measurement in the XPS technique. (1) First a X-Ray beam is monochromatized and focused on the sample. (2) Then the photons induce the photoelectric effect on the material expelling the electrons with certain kinetic energies that depend on the binding energies of the affected orbitals. (3) The electrons go through a process of selection that allows creating a spectrum that can be analyzed to identify and quantify the surface stoichiometry [115].

Although the contact mode has not been used directly in this thesis, its explanation states a good base from where the other modes can be explained. The sensing element of the system is the nanometric tip, placed in the apex of the cantilever. The interaction between the tip and the sample due to microscopic forces induces a deflection in the cantilever. A laser focused on the apex of the cantilever is reflected towards a photodiode where the deflection of the cantilever can be detected and transformed into an electrical signal. Simultaneously, a set of piezoelectrics allows the system to scan in the XY plane (parallel to the sample surface) and define a complete image of the topography. Nevertheless letting the cantilever to deflect “freely” could cause damage to the tip and to the sample. Due to the changes of height in the measured area the strength of the interaction between the tip and the sample could induce a crash between these two. To solve this problem a feedback system (FS) is implemented in most of the AFM modes. In contact mode the deflection of the cantilever is the parameter controlled and corrected by this FS. The user adjusts a value of the deflection and the system keeps it constant during the scan. This is known

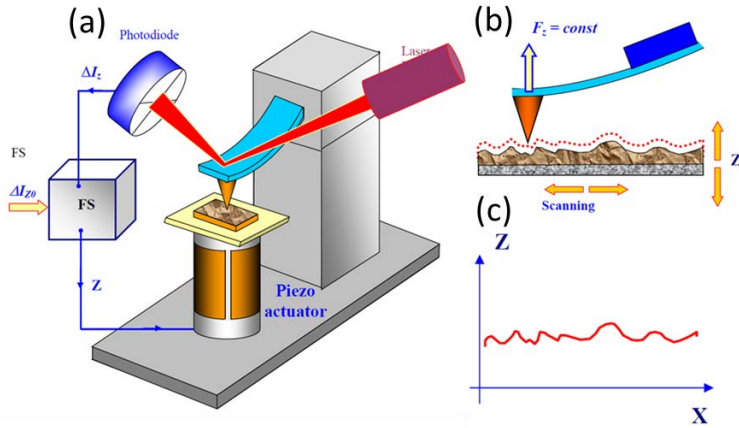


FIGURE A.8: (a) Sketch of an AFM system where the different elements interact between them through the FS in accordance with the input received by the controller. (b) Scheme of a scan in contact mode where the force between the tip and the sample remains constant (and so the deflection) while the value of Z is changed to correct the topography roughness. (c) Final image of the (b) scan recording the position of the piezoelectric system at every point [116].

as Set Point (SP). When due to a change in the height of the topography the cantilever deflection experiences a change, the FS compares this value with the SP and applies a correction voltage to the Z piezoelectric so the deflection can be kept constant at the SP. The elongation of the Z piezoelectric is then recorded for each XY point so a complete image of the topography is recorded at the end of the scan [117].

The AFM system used in this thesis has been a MFP3D from Asylum (Figure A.9 (a) and (b)). In this model the acquisition of the position values (both the height and the position in the XY plane) is given by a Nano Positioning System (NPS) [118] which is based on the Linear Variable Differential Transformers technology which is depicted in Figure A.9 (c). In this system a magnetic cylindrical core is attached to the object whose displacement is going to be measured. In its nearby three solenoid coils are placed in the center (primary coil) and in the extremes of it (secondary coils). The secondary coils (A and B) are connected in series but with opposite directions as is depicted in Figure A.9 (c). When an AC voltage is applied to the primary coil it is transferred to the secondary coils through the magnetic core generating V_a and V_b voltages. The difference between these potentials will depend on the position of the core and therefore, with the proper calibration, any displacement of the core and the piezoelectric can

be tracked [119]. The application of this system minimizes typical problems with the piezoelectrics as the non-linear voltage displacement, the hysteresis during the cycles and the creeping [118]. The NPS reduces the errors in the localization of the XY plane and in the recording of the height position.

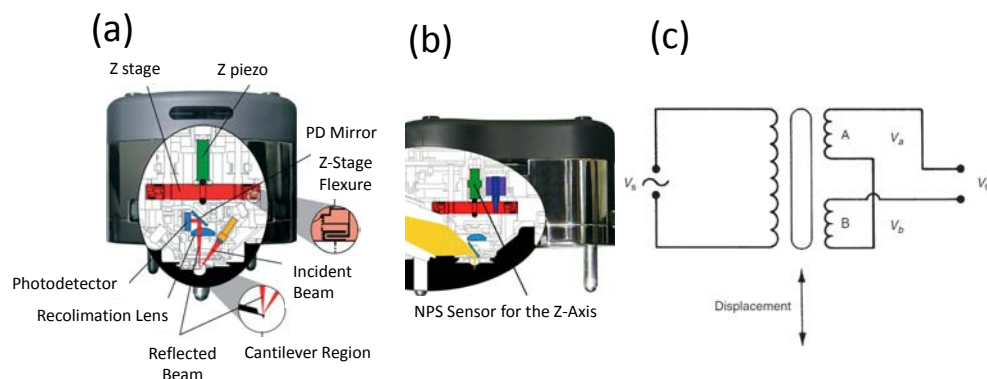


FIGURE A.9: Figure X: (a) frontal view and (b) side view of a MFP-3D head AFM system [118]. (c) Scheme of a Linear Variable Differential Transformer [119].

A.3.1 Intermittent contact mode (tapping)

Although the contact mode can measure the topography of the surfaces, one of its major drawbacks is that both the tip and the sample can be damaged during the scanning. Intermittent contact mode (commonly known as tapping) avoids this problem by “tapping” intermittently the sample surface instead of rubbing the tip with a certain force. In this mode the cantilever is forced to oscillate at its resonance frequency due to the vibration of a piezoelectric material placed in the base of the cantilever. This piezoelectric actuator is controlled by an AC source that is able to regulate the amplitude of the free oscillation (without any interaction with the sample). In tapping mode the amplitude of the cantilever oscillation is the parameter used as a SP. When the probe oscillates at the free amplitude (Figure A.10 (a) (1)) the phase between the excitation signal of the piezoelectric and the generated oscillation is 90° , ensuring a maximal energy transfer. When the tip is close enough to interact with the sample this phase is altered and, thus, the efficiency in the energy transfer is reduced decreasing the amplitude of the oscillation. This reduction of the amplitude changes linearly with the mean distance between the tip and the sample, as can be observed in Figure A.10 (a) (2) and (3). Therefore, changes in the topography of the sample can induce changes in the amplitude of the oscillation while the FS maintains

the amplitude constant by adjusting the expansion of the Z piezo. If the height of the topography increases (decreases) the amplitude will decrease (increase) and the Z piezo will retrace (expand) to correct the differences as can be observed in figure A.10 (b) [117].

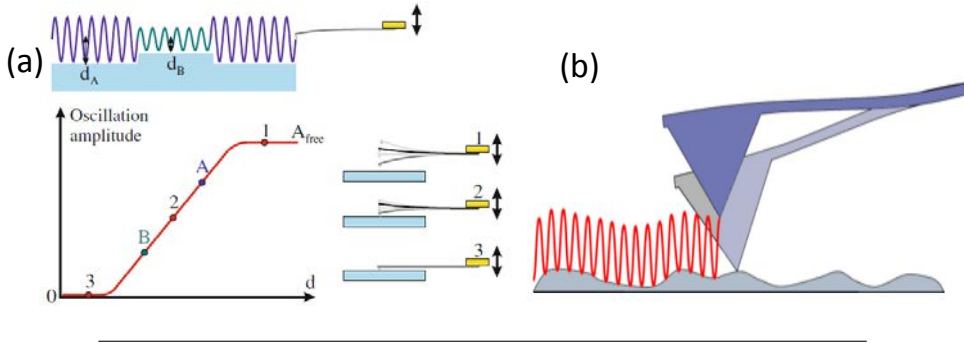


FIGURE A.10: (a) Variations of the oscillation amplitude due to the proximity between the probe and the surface (without FS). As the distance between the tip and the surface (d) is decreased the oscillation is reduced as well [117]. (b) Sketch of a measure in tapping mode. As the topography changes the probe is lifted or taken down to conserve the SP amplitude [120].

A.3.2 Conductive Atomic Force Microscopy

The local electric measurements of this thesis have been evaluated by means of Conductive Atomic Force Microscopy (C-AFM). In this mode a conductive tip (or with a conductive covering) rubs directly the sample. Similar to the contact mode, the deflection of the cantilever is used as the SP maintaining constant the applied force. Nevertheless the special feature of the C-AFM is the capability of measuring the current intensity flowing through a conductive tip when a voltage is applied between the sample and the tip. Two different main measurements can be performed in this mode:

- Current maps, where the current is measured simultaneously with the topography during a scan in the XY plane performed at a constant voltage.
- I/V curves, where the intensity of the current is measured as a function of an applied voltage in a single point.

The C-AFM system consists in a DC Voltage source (in the simplest case) biasing a conductive tip by one side and a macroscopic contact from the

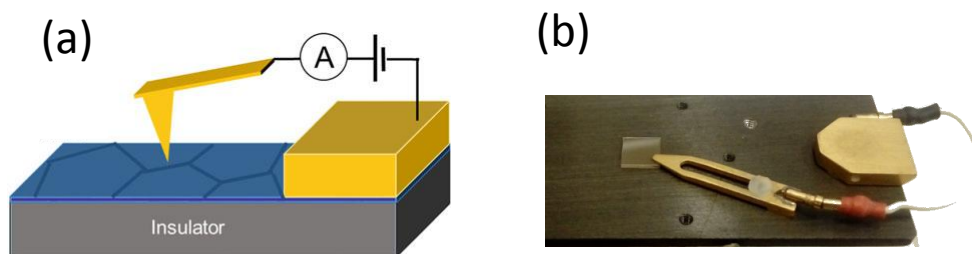


FIGURE A.11: (a) Sketch of a C-AFM system in an in-plane configuration, the one used in the measurements of this thesis [95]. (b) Picture of the real setup where a conductive clamp acts as macroscopic contact.

other side. These two elements are used to measure the conductivity of a sample in a two point configuration as is shown in Figure A.11 (a). The real setup can be appreciated in Figure A.11 (b) where the measured sample is subjected by a conductive clamp that is used also as the macroscopic contact. This scheme can be modeled as closed circuit with several resistances placed in series. It is worth noting that the measured current is mainly limited by resistance of the sample in the vicinity of the tip and the other resistances usually have a secondary role. Due to this, the system can measure the local electrical properties of the samples with enough lateral resolution to be able to correlate them with the topographic features of the sample [95].

Despite the great capabilities of C-AFM for evaluating local electrical properties, this technique is also subjected to few drawbacks related to the stability of the measurements. Besides the usual mechanic damage generated by the contact methodology, the Joule Heating can be significant at the apex of the tip even at low voltages which can produce a progressive degradation of the conductive tip or tip coating as can be appreciated in Figure A.12 [95]. Moreover, at higher voltages other surface effects, as the anodic oxidation, can take place changing the properties of the sample and generating contamination the apex of the tip [94] [93].

The C-AFM measurements shown in this thesis have been performed using a MFP3D from Asylum with a dual gain ORCA module which can track currents from 0.1 nA to 100 μ A using voltages in the range of 0 to 10 V. The AFM also possess a closed chamber module that allows an atmospheric control during the measurements. In all the images and I-V curves, a diamond doped coated probes (DDESP from Bruker) were used in order to ensure the reproducibility of the experiments and to facilitate the comparison between measurements.

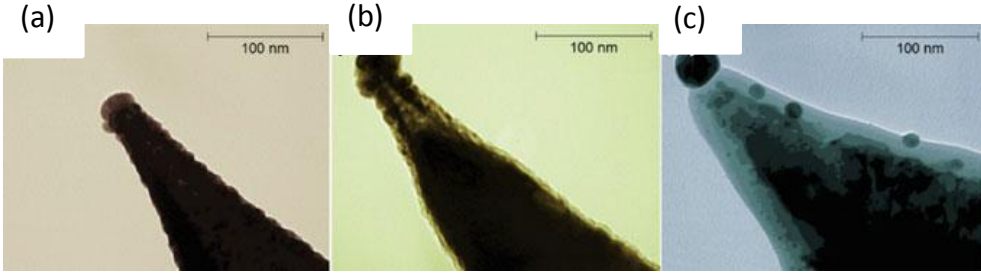


FIGURE A.12: TEM images of the apex of a conductive tip: (a) before being used, (b) annealed at reducing conditions and (c) annealed at oxidizing conditions [95].

A.3.3 Kelvin Probe Force Microscopy

The surface potential of the films have been studied by Kelvin Probe Force Microscopy (KPFM) also known by Scanning Kelvin Probe Microscopy (SKPM) or Kelvin Force Microscopy (KFM). In this AFM based technique a conductive tip is able to characterize the contact potential of a surface at the local scale. One method to measure it is by a two pass measurement. First the system measures the topography of the sample in tapping mode (Figure A.13 (a)). Then, the AFM is lifted at a certain height (z) and follows the same topography while measuring the contact potential, in this way topographic features do not influence the electric measurement (Figure A.13 (b)) [121][116].

The Contact Potential Difference (CPD) measured by an AFM tip is defined as equation A.6:

$$V_{CPD} = \frac{\phi_{tip} - \phi_{sample}}{e} \quad (\text{A.6})$$

Where ϕ_{tip} and ϕ_{sample} are the work function of the tip and the sample respectively and e is the elemental charge of an electron. The differences between the work functions of the tip and the sample (and hence the differences between the Fermi levels) produce an electrical force that can be modelled as parallel plate capacitor (equation A.7):

$$F_e = -\frac{1}{2}\Delta V^2 \cdot \frac{dC(z)}{dz} \quad (\text{A.7})$$

Where C is the capacitance of the system, and ΔV is the voltage difference between the tip and the sample. In order to measure the CPD, and V_{AC}

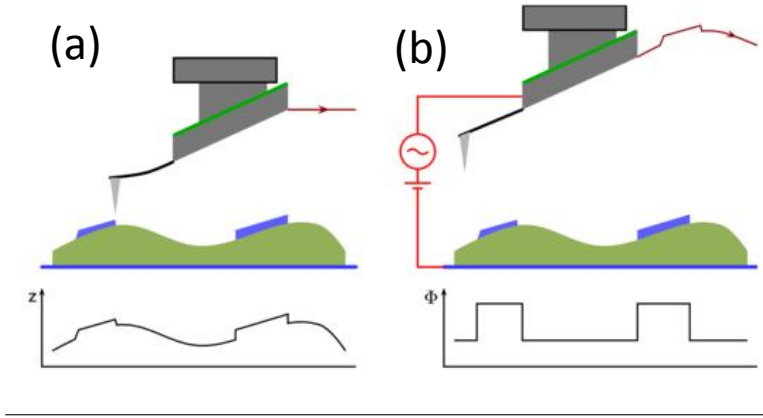


FIGURE A.13: Two pass measurement KPFM mode. (a) First pass in which the topography of the sample is recorded. (b) Second pass in which the tip is lifted at a certain height and follows the already measured topography. In this pass a V_{AC} voltage and a V_{DC} voltage are applied to the tip to measure the contact potential [122].

(at the cantilever resonance frequency) and a variable V_{DC} are applied between the tip and the sample during the second pass (as depicted in Figure A.13 (b)). Therefore the difference of Voltage can be expressed as:

$$\Delta V = V_{tip} - V_{CPD} = (V_{DC} - V_{CPD}) + V_{AC} \cdot \sin(\omega t) \quad (\text{A.8})$$

And by substituting it in the equation A.7:

$$F_e = -\frac{1}{2} \frac{dC(z)}{dz} \cdot [(V_{DC} - V_{CPD}) + V_{AC} \cdot \sin(\omega t)]^2 \quad (\text{A.9})$$

Resolving the squared voltage, 3 different Force contributions can be separated according to their dependence with the resonance frequency:

$$F_{DC} = -\frac{dC(z)}{dz} \cdot \left[\frac{1}{2} (V_{DC} - V_{CPD})^2 \right] \quad (\text{A.10})$$

$$F_{\omega} = -\frac{dC(z)}{dz} \cdot [(V_{DC} - V_{CPD}) \cdot V_{AC} \cdot \sin(\omega t)] \quad (\text{A.11})$$

$$F_{2\omega} = \frac{1}{4} \frac{dC(z)}{dz} \cdot V_{AC}^2 \cdot [\cos(2\omega t) - 1] \quad (\text{A.12})$$

By fixing a lock-in into the frequency (ω) one can monitor the CPD. To track the CPD the F_{ω} term (eq. A.11) is nullified by applying the opposite V_{DC} . Then this term is kept a 0 using a FS and correcting the differences in the scan with different values of V_{DC} . Recording the used values of V_{DC} a map

of the CPD can be imaged [117] [123]. Moreover, calibrating the ϕ_{tip} , the ϕ_{sample} can be obtained according to equation A.6.

Unlike the other SPM techniques used, all the images of KPFM depicted in the thesis were acquired in a NTEGRA Prima from NT-MDT in the Institute of Physics of Belgrade. The KPFM measurements were performed in an air conditions.

A.4 Electron Based Techniques

Besides the employment in this work of SPM and XRD techniques to evaluate the morphology and structural properties, electron based techniques have been used to contrast the information and add compositional information of the films. In these techniques electrons are emitted from an electron gun filament (usually made of tungsten) and are accelerated towards the sample. Then, electromagnetic lenses focus the electron beam into a fine probe on the sample. The electron beam penetrates into the sample and many different phenomena take place. As it can be observed in Figure A.14 (a), among these effect there are secondary electrons, backscattered electrons, characteristic X-ray emission and transmitted electrons. Every technique focus its attention to one (or more) of these phenomena to obtain information about the topography, the composition or the crystalline structure of the material [124].

A.4.1 Scanning Electron Microscopy

In this thesis, all the Scanning Electron Microscopy (SEM) images come from the detection of secondary and backscattered electrons. Secondary electrons are generated by the ejection of an orbital atom due to the collision with the incident beam. Since these electrons cannot escape from large penetration depths, only the ones emitted near the surface can reach the detector and therefore they provide topographical information. On the other hand, backscattered electrons are the ones generated by the scattering of the incident electrons with the nucleus of the material. These electrons provide compositional contrast of the sample, the more heavy is a material the brighter contrast will have in the image [124].

A.4.2 Electron probe microanalysis

Electron probe microanalysis (EPMA) uses the emitted characteristic X-ray to analyze the chemical composition of the samples. These X-rays are generated when the incident electron beam knocks out inner shell electrons of

the sample material. This inner shell ionization causes a chain of relaxation processes from outer shell electron into lower energy levels emitting X-rays in every stage. These X-rays are characteristics from every element and therefore one can use them to obtain compositional information from the sample [125] [124].

A.4.3 Transmission Electron Microscopy

Contrary to SEM and EPMA, Transmission Electron Microscopy (TEM) data is obtained from electrons that are able to cross the specimen. To be able to measure these electrons the sample under study must be thin enough to allow the path of electrons. In the case of thin films, cross sections are of a particular interest to obtain images of the film with atomic resolution. Moreover, TEM images can also provide crystallographic information and compositional contrast. In order to prepare the cross section specimens, slices of the sample are cut and glued together on a grid (Figure A.14 (b)). Then the interface of the films is attacked by an ion milling process reducing the thickness at a local scale and making it suitable for TEM measurements. The specimen is then exposed to an incident electron beam that crosses the sample and produces different kind of signals due to its interaction with the film [126] [127].

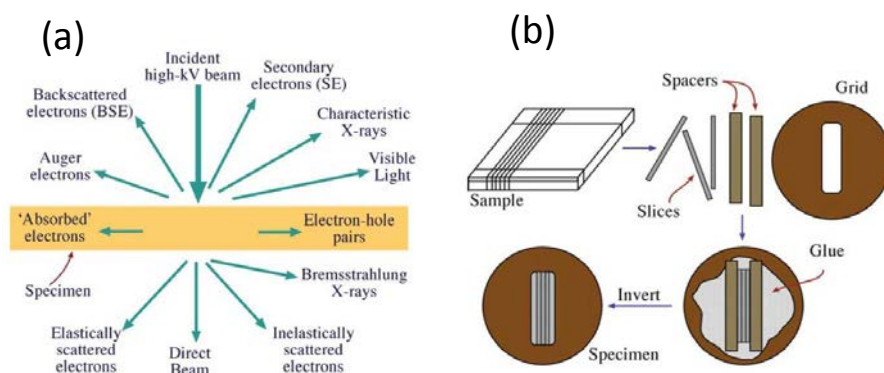


FIGURE A.14: (a) Possible resultant interactions of an electron beam with a sample. A variety of electron microscopies detect the different emitted signals providing information from a wide range of properties of the sample [126]. (b) Scheme of the preparation process for a thin film cross section [127].

In this thesis a FEI Tecnai G² F20 has been used to acquire the depicted TEM images. The mentioned preparation and the measurements of the samples were carried out by the electron microscopy unit of the ICN2. The

SEM images were obtained with a QUANTA FEI 200 FEG-ESEM located in the ICMAB and the EPMA results were measured with a commercial JXA-8230 equipment from JEOL in the CCiTUB.

A.5 Lithography processes

With the aim of obtaining macroscopic electric measurements, several films have been modified through lithographic processes. According to the precision needed in the electric measurement, two different procedures were carried out.

A.5.1 Macroscopic masks

In the samples where only the resistivity was measured a mask made of aluminum foil was placed on top of the sample. Then a Pt film was deposited with sputtering in the areas unprotected by the mask. This leaves the film with 4 elongated contacts of Pt on the thin film as it can be observed in Figure A.15 (a).

A.5.2 U-V lithography

For electrical measurements that required more precision, as Hall Effect measurements, a track was lithographed by means of U-V lithography. In this process, the film is first coated by a photosensible resist (Figure A.16 (1)). Then, it is illuminated with U-V light following a certain pattern known as mask. In our case, positive photoresist has been used, this means that the areas of the resist exposed to the U-V light become more soluble to a certain developer (Figure A.16 (2)). Therefore, submerging the film into the developer after the exposition can transfer the desired pattern from the mask to the resist (Figure A.16 (3)).

Once reached this point two different steps can be followed, as it is depicted in Figure A.16 (4). In the first case (Figure A.16 (4a)), similar to the one of the macroscopic masks, it is necessary to deposit platinum with Sputtering to add electrical contacts. This time the platinum will be only deposited directly on the film in the areas where the resist has been removed due to the UV radiation. After a lift-off process that removes the remaining resist, only the platinum deposited in these areas will stand (Figure A.16 (5a)).

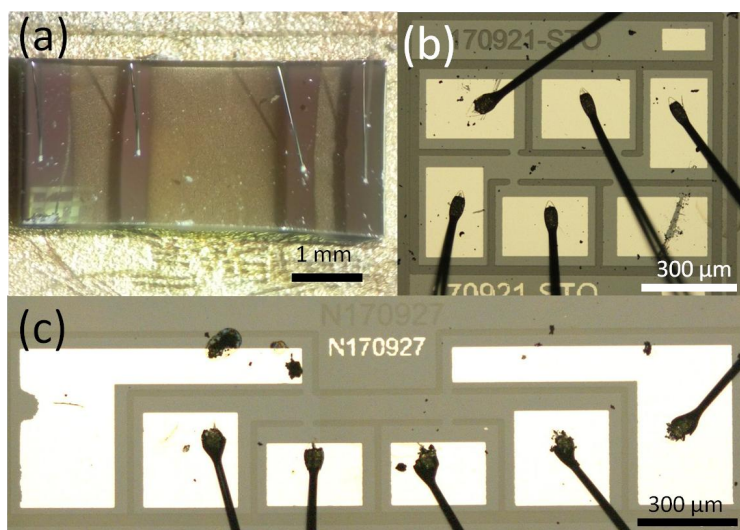


FIGURE A.15: Lithographies used in the present thesis. (a) Track consisting in 4 bars of platinum which does not require a photolithography process but can only measures the resistivity of the samples. (b) Photolithographed Track consisting in 2 intensity, 2 voltage and 2 hall contacts that allow the measurement of the resistivity and the Hall effect in the films. (c) Equivalent track to (b) with expanded contacts to ease the contact process.

On the other hand, besides the possibility of making smaller electrical contacts, photolithography has been used to create tracks with a better accuracy of the measurements. After the developing process, the film is exposed to an ion milling attack that removes unprotected parts of the film leaving the areas with resist unaltered (Figure A.16 (4b)). After removing the remaining resist with a cleaning step, only the film tracks will remain (Figure A.16 (5b)) [128]. Combining these two processes it has been possible to obtain the tracks of the Figure A.15 (b and c). The longitude (l) and width (w) of the measured track between the voltage contacts is $350 \mu\text{m}$ and $100 \mu\text{m}$ in the case of the track of Figure A.15 (b) and $400 \mu\text{m}$ and $80 \mu\text{m}$ in the case of the lithography depicted in Figure A.15 (c).

The Photolithography tracks used in this thesis were carried out in a MicroWriter ML from Durham Magneto Optics Ltd.

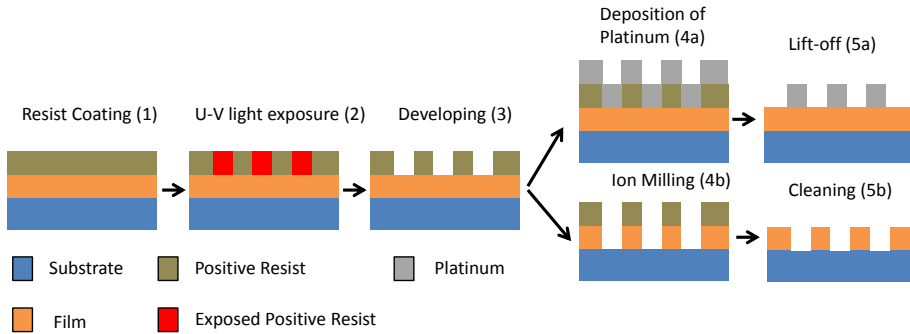


FIGURE A.16: Sketch of the photolithography process showing the mechanisms to remove part of the film or deposit metallic contacts. The use of both procedures is necessary to obtain the aforementioned tracks.

A.6 Electric Measurements

In this thesis macroscopic electric measurements have been performed using a Physical Properties Measurement System (PPMS) from Quantum Design. This versatile device allows injecting current while measuring a voltage drop at a wide range of temperatures and additionally adding a magnetic field. Therefore this instrument is suitable for resistivity, magnetoresistance and Hall Effect measurements, which will be explained in the following subsections.

A.6.1 Resistivity measurements

During these measurements, an electrical current is injected through the intensity contacts (indicated as I in Figure A.17) while the potential drop is measured between the Voltage contacts (indicated as V_R in Figure A.17). By measuring the voltage with two different contacts that those use by injecting current, in what is called four probe measurements, possible contributions of the contact resistance are avoided.

The Resistance can then be calculated by the Ohm's law:

$$R = \frac{V}{I} \quad (\text{A.13})$$

Where R is the Resistance, V is the Voltage drop and I is the intensity of the current injected. Knowing the dimensions of the track between the Voltage

contacts, the resistivity of the material can be calculated:

$$\rho = R \cdot \frac{t \cdot w}{l} \quad (\text{A.14})$$

Where ρ is the resistivity of the material, t is the thickness of the film, w is the width of the track and l is the longitude of the track.

Sheet resistance is another way to express the resistivity of thin films that does not account the thickness of the film:

$$R_s (\Omega/\square) = \frac{\rho}{t} \quad (\text{A.15})$$

A.6.2 Magnetoresistance

The term Magnetoresistance (MR) involves the changes in the resistivity of a material when a magnetic field is applied. This phenomenon is present in a wide range of materials and its origins vary from one to another [129]. In this thesis MR measurements have been performed by fixing one specific temperature and sweeping the intensity of a perpendicular magnetic field. Then, during the sweep, the resistivity of the material is measured as indicated above (V_R in Figure A.17). Finally, the value of MR in percentage can be calculated by equation.

$$MR(\%) = \frac{\rho(H) - \rho(0)}{\rho(0)} \quad (\text{A.16})$$

Where $\rho(0)$ is the resistivity at 0 magnetic field.

A.6.3 Hall Effect Measurements

When a magnetic field (H) is applied perpendicularly to a current (I), the charge carriers are deviated from their linear trajectory due to the Lorentz force. This phenomenon is known as Hall Effect and produces a Voltage (V_H in Figure A.17) perpendicular to both the current and the magnetic field [88].

The Hall Effect can be evaluated in the lithographed tracks by measuring the voltage drop between the contacts (V_H in Figure A.17). Dividing this voltage by the intensity, a value of Resistance can be obtained. Nevertheless the Hall Effect can be a very subtle effect and can be hidden in the obtained resistance by other components, as a MR or an ohmic resistance.

$$R = R_{hall} + R_{MR} + R_{ohm} \quad (\text{A.17})$$

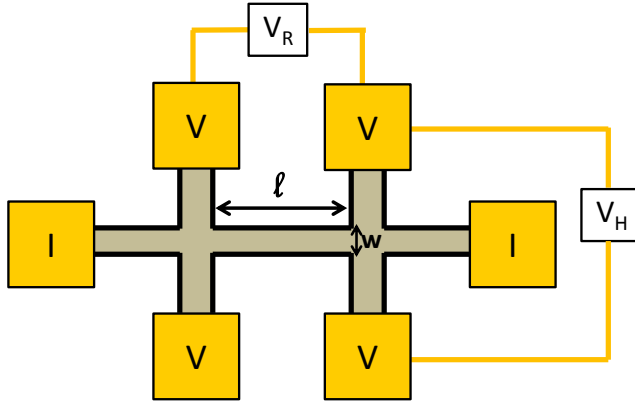


FIGURE A.17: Sketch of the electrical measurements in a four point configuration using a lithographed track.

In order to isolate the Hall component from these undesirable resistance components, the branch of resistance at positive magnetic fields is subtracted by the branch of the resistance at negative magnetic fields. On one hand, since the ohmic and the MR components of the resistance are symmetric they are cancelled. On the other hand, the Hall component is antisymmetric doubling this way its value with the difference, as it can be appreciated in the following equation:

$$\begin{aligned}
 R(+H) &= R_{hall} + R_{MR} + R_{ohm} \\
 R(-H) &= R_{hall} - R_{MR} - R_{ohm} \\
 R(+H) + R(-H) &= 2R_{hall}
 \end{aligned}
 \tag{A.18}$$

Then the Hall component can be calculated as:

$$R_{hall}(H) = \frac{R(+H) + R(-H)}{2}
 \tag{A.19}$$

In the simplest case, the R_{hall} depends linearly with the applied magnetic field, therefore is more convenient to express the Hall Effect behavior of a sample with the Hall coefficient (R_H) that can be calculated with:

$$R_H(H) = \frac{V_H \cdot t}{I \cdot H} = \frac{R_{hall} \cdot t}{H}
 \tag{A.20}$$

Bibliography

- [1] M. M. Waldrop, "The chips are down for Moore's law," *Nature News*, vol. 530, no. 7589, p. 144, 2016.
- [2] S. I. Association, "Rebooting the IT Revolution," in *Rebooting the IT Revolution Workshop*, 2015.
- [3] V. K. Joshi, "Spintronics: A contemporary review of emerging electronics devices," *Engineering Science and Technology, an International Journal*, vol. 19, no. 3, pp. 1503–1513, 2016.
- [4] N. Xin, J. Guan, C. Zhou, X. Chen, C. Gu, Y. Li, M. A. Ratner, A. Nitzan, J. F. Stoddart, and X. Guo, "Concepts in the design and engineering of single-molecule electronic devices," *Nature Reviews Physics*, vol. 1, pp. 211–230, 2019.
- [5] S. Slesazeck and T. Mikolajick, "Nanoscale resistive switching memory devices: A review," *Nanotechnology*, vol. 30, no. 35, p. 352003, 2019.
- [6] R. Waser, R. Dittmann, G. Staikov, and K. Szot, "Redox-Based Resistive Switching Memories: Nanoionic Mechanisms, Prospects, and Challenges," *Advanced Materials*, vol. 21, no. 25-26, pp. 2632–2663, 2009.
- [7] R. Waser, D. Ielmini, H. Akinaga, H. Shima, H.-S. P. Wong, J. J. Yang, and S. Yu, "Introduction to Nanoionic Elements for Information Technology," in *Resistive Switching*. John Wiley & Sons, Ltd, 2016, pp. 1–30.
- [8] E. Janod, J. Tranchant, B. Corraze, M. Querré, P. Stoliar, M. Rozenberg, T. Cren, D. Roditchev, V. Phuoc, M. Besland, and L. Cario, "Resistive Switching in Mott Insulators and Correlated Systems," *Advanced Functional Materials*, vol. 25, no. 40, pp. 6287–6305, 2015.
- [9] Y. Wang, K.-M. Kang, M. Kim, H.-S. Lee, R. Waser, D. Wouters, R. Dittmann, J. J. Yang, and H.-H. Park, "Mott-transition-based RRAM," *Materials Today*, vol. 28, pp. 63–80, 2019.

- [10] S. J. Moon, H. Jin, K. W. Kim, W. S. Choi, Y. S. Lee, J. Yu, G. Cao, A. Sumi, H. Funakubo, C. Bernhard, and T. W. Noh, "Dimensionality-Controlled Insulator-Metal Transition and Correlated Metallic State in 5d Transition Metal Oxides $\text{Sr}_{n+1}\text{Ir}_n\text{O}_{3n+1}$ ($n = 1, 2,$ and ∞)," *Physical Review Letters*, vol. 101, p. 226 402, 2008.
- [11] A. Biswas, K. Kim, and Y. Jeong, "Metal insulator transitions in perovskite SrIrO_3 thin films," *Journal of Applied Physics*, vol. 116, no. 21, p. 213 704, 2014.
- [12] N. Domingo, L. López-Mir, M. Paradinas, V. Holy, J. Železný, D. Yi, S. J. Suresha, J. Liu, C. Rayan Serrao, R. Ramesh, C. Ocal, X. Martí, and G. Catalan, "Giant reversible nanoscale piezoresistance at room temperature in Sr_2IrO_4 thin films," *Nanoscale*, vol. 7, pp. 3453–3459, 2015.
- [13] J. C. Scott and L. D. Bozano, "Nonvolatile Memory Elements Based on Organic Materials," *Advanced Materials*, vol. 19, no. 11, pp. 1452–1463, 2007.
- [14] N. Ciocchini, M. Laudato, M. Boniardi, E. Varesi, P. Fantini, A. L. Lacaita, and D. Ielmini, "Bipolar switching in chalcogenide phase change memory," *Scientific Reports*, vol. 6, p. 29 162, 2016.
- [15] A. Sawa, "Resistive switching in transition metal oxides," *Materials Today*, vol. 11, no. 6, pp. 28–36, 2008.
- [16] A. Mehonic and A. Kenyon, "Resistive Switching in Oxides," in *Defects at Oxide Surfaces*. Springer, 2015, pp. 401–428.
- [17] Z. Yan and J.-M. Liu, "Resistance switching memory in perovskite oxides," *Annals of Physics*, vol. 358, pp. 206–224, 2015.
- [18] S. Bagdzevicius, K. Maas, M. Boudard, and M. Burriel, "Interface-type resistive switching in perovskite materials," *Journal of Electroceramics*, vol. 39, 157184, 2017.
- [19] Z. Wang, H. Wu, G. W. Burr, C. S. Hwang, K. L. Wang, Q. Xia, and J. J. Yang, "Resistive switching materials for information processing," *Nature Reviews Materials*, vol. 5, pp. 173–195, 2020.
- [20] A. Biswas, K.-S. Kim, and Y. H. Jeong, "Metal-Insulator Transitions and Non-Fermi Liquid Behaviors in 5d Perovskite Iridates," in *Perovskite Materials: Synthesis, Characterisation, Properties, and Applications*. intechopen, 2016.
- [21] J. Patterson and B. Bailey, *Solid-State Physics: Introduction to the Theory*. Springer, 2016.

- [22] A. Lagendijk, B. V. Tiggelen, and D. S. Wiersma, "Fifty years of Anderson localization," *Physics today*, vol. 62, pp. 24–29, 8 2009.
- [23] E. Abrahams, *50 Years of Anderson Localization*. World Scientific, 2010.
- [24] P. A. Lee and T. V. Ramakrishnan, "Disordered electronic systems," *Reviews in Modern Physics*, vol. 57, pp. 287–337, 1985.
- [25] G. Kotliar and D. Vollhardt, "Strongly correlated materials: Insights from dynamical mean-field theory," *Physics today*, vol. 57, pp. 53–60, 2004.
- [26] A. Agarwala, *Excursions in Ill-Condensed Quantum Matter: From Amorphous Topological Insulators to Fractional Spins*. Springer, 2019.
- [27] W. Yang, Y. Yin, Y. Peng, G. Zhao, Y. Liu, S. Li, W. Wang, W. Zhou, and D. Tang, "Effect of oxygen vacancies on the resistive switching behavior of hexagonal WO_3 nanowire," *Materials Research Express*, vol. 6, no. 8, p. 085 072, 2019.
- [28] N. F. Mott, "The Basis of the Electron Theory of Metals, with Special Reference to the Transition Metals," *Proceedings of the Physical Society. Section A*, vol. 62, no. 7, pp. 416–422, 1949.
- [29] P. W. Anderson, "Absence of Diffusion in Certain Random Lattices," *Physical Review*, vol. 109, pp. 1492–1505, 1958.
- [30] M. Imada, A. Fujimori, and Y. Tokura, "Metal-insulator transitions," *Reviews of Modern Physics*, vol. 70, pp. 1039–1263, 1998.
- [31] R. J. D. Tilley, "The ABX_3 Perovskite Structure," in *Perovskites*. John Wiley & Sons, Ltd, 2016, pp. 1–41.
- [32] H. Liu and X. Yang, "A brief review on perovskite multiferroics," *Ferroelectrics*, vol. 507, no. 1, pp. 69–85, 2017.
- [33] Y.-K. Liu, Y.-W. Yin, and X.-G. Li, "Colossal magnetoresistance in manganites and related prototype devices," *Chinese Physics B*, vol. 22, no. 8, p. 087 502, 2013.
- [34] S. Royer and D. Duprez, "Catalytic Oxidation of Carbon Monoxide over Transition Metal Oxides," *ChemCatChem*, vol. 3, no. 1, pp. 24–65, 2011.
- [35] R. Scherwitzl, S. Gariglio, M. Gabay, P. Zubko, M. Gibert, and J.-M. Triscone, "Metal-Insulator Transition in Ultrathin LaNiO_3 Films," *Physical Review Letters*, vol. 106, p. 246 403, 2011.
- [36] D. A. Crandles, T. Timusk, J. D. Garrett, and J. E. Greedan, "Mott insulator to correlated metal: Optical study of $\text{La}_{1-x}\text{TiO}_3$," *Physical Review B*, vol. 49, pp. 16 207–16 213, 1994.

- [37] J. M. D. Coey, "Magnetism of electrons," in *Magnetism and Magnetic Materials*. Cambridge University Press, 2010, 6296.
- [38] Y. Cai, Y. Li, and J. Cheng, "Synthesis, Crystal Structure, and Physical Properties of the Perovskite Iridates," in *Perovskite Materials: Synthesis, Characterisation, Properties, and Applications*. inthechopen, 2016.
- [39] R. J. D. Tilley, "Modular Structures," in *Perovskites*. John Wiley & Sons, Ltd, 2016, pp. 123–155.
- [40] L. Zhang, B. Pang, Y. B. Chen, and Y. Chen, "Review of Spin-Orbit Coupled Semimetal SrIrO₃ in Thin Film Form," *Critical Reviews in Solid State and Materials Sciences*, vol. 43, no. 5, pp. 367–391, 2018.
- [41] J. Longo, J. Kafalas, and R. Arnott, "Structure and properties of the high and low pressure forms of SrIrO₃," *Journal of Solid State Chemistry*, vol. 3, no. 2, pp. 174–179, 1971.
- [42] J. G. Zhao, L. X. Yang, Y. Yu, F. Y. Li, R. C. Yu, Z. Fang, L. C. Chen, and C. Q. Jin, "High-pressure synthesis of orthorhombic SrIrO₃ perovskite and its positive magnetoresistance," *Journal of Applied Physics*, vol. 103, no. 10, p. 103706, 2008.
- [43] Y. Liu, H. Masumoto, and T. Goto, "Structural, Electrical and Optical Characterization of SrIrO₃ Thin Films Prepared by Laser-Ablation," *Materials Transactions*, vol. 46, no. 1, pp. 100–104, 2005.
- [44] Y. F. Nie, P. D. C. King, C. H. Kim, M. Uchida, H. I. Wei, B. D. Faeth, J. P. Ruf, J. P. C. Ruff, L. Xie, X. Pan, C. J. Fennie, D. G. Schlom, and K. M. Shen, "Interplay of Spin-Orbit Interactions, Dimensionality, and Octahedral Rotations in Semimetallic SrIrO₃," *Physical Review Letters*, vol. 114, p. 016401, 2015.
- [45] L. Fruchter, O. Schneegans, and Z. Z. Li, "Anisotropy and interaction effects of strongly strained SrIrO₃ thin films," *Journal of Applied Physics*, vol. 120, p. 075307, 2016.
- [46] A. Biswas and Y. H. Jeong, "Growth and engineering of perovskite SrIrO₃ thin films," *Curr. Appl. Phys.*, vol. 17, no. 5, pp. 605–614, 2017.
- [47] Y. K. Kim, A. Sumi, K. Takahashi, S. Yokoyama, S. Ito, T. Watanabe, K. Akiyama, S. Kaneko, K. Saito, and H. Funakubo, "Metalorganic Chemical Vapor Deposition of Epitaxial Perovskite SrIrO₃ films on (100) SrTiO₃ Substrates," *Japanese Journal of Applied Physics*, vol. 45, no. 1, pp. L36–L38, 2005.
- [48] M. Nuss, *Advanced Solid State Physics*. TU Graz, 2010.

- [49] Y. Klein and I. Terasaki, "Transport Properties and Cationic Substitutions in Sr_2IrO_4 ," *Journal of Electronic Materials*, vol. 38, pp. 1331–1336, 2009.
- [50] J. S. Lee, Y. Krockenberger, K. S. Takahashi, M. Kawasaki, and Y. Tokura, "Insulator-metal transition driven by change of doping and spin-orbit interaction in Sr_2IrO_4 ," *Physical Review B*, vol. 85, p. 035 101, 2012.
- [51] M. Ito, M. Uchida, Y. Kozuka, K. S. Takahashi, and M. Kawasaki, "Effective carrier doping and metallization in $\text{La}_x\text{Sr}_{2-x-y}\text{Ba}_y\text{IrO}_{4-\delta}$ thin films," *Physical Review B*, vol. 93, p. 045 139, 2016.
- [52] C. Wang, H. Seinige, G. Cao, J.-S. Zhou, J. B. Goodenough, and M. Tsoi, "Electrically tunable transport in the antiferromagnetic Mott insulator Sr_2IrO_4 ," *Physical Review B*, vol. 92, p. 115 136, 2015.
- [53] B.-J. Chen, N. Yang, N. Zhong, X.-D. Tang, P.-X. Yang, P.-H. Xiang, and C.-G. Duan, "Selective growth of Ruddlesden-Popper strontium iridate epitaxial films by controlling oxygen partial pressure in pulsed laser deposition," *Materials Letters*, vol. 202, pp. 96–98, 2017.
- [54] K. Nishio, H. Y. Hwang, and Y. Hikita, "Thermodynamic guiding principles in selective synthesis of strontium iridate Ruddlesden-Popper epitaxial films," *APL Materials*, vol. 4, no. 3, p. 036 102, 2016.
- [55] S. S. A. Seo, J. Nichols, J. Hwang, J. Terzic, J. H. Gruenewald, M. Souri, J. Thompson, J. G. Connell, and G. Cao, "Selective growth of epitaxial Sr_2IrO_4 by controlling plume dimensions in pulsed laser deposition," *Applied Physics Letters*, vol. 109, no. 20, p. 201 901, 2016.
- [56] Z. Z. Li, O. Schneegans, and L. Fruchter, *Synthesis of Perovskite SrIrO_3 Thin Films by Sputtering Technique*, 2016. arXiv: 1610.03722.
- [57] J. J. Randall, L. Katz, and R. Ward, "The Preparation of a Strontium-Iridium Oxide Sr_2IrO_4 ," *Journal of the American Chemical Society*, vol. 79, no. 2, pp. 266–267, 1957.
- [58] K. Wasa, "Sputtering Phenomena," in *Handbook of Sputtering Technology (Second Edition)*, William Andrew Publishing, 2012, pp. 41–75.
- [59] A. P. Sakhya, A. Dutta, and T. Sinha, "Dielectric and impedance spectroscopic studies of neodymium gallate," *Physica B: Condensed Matter*, vol. 488, pp. 1–7, 2016.
- [60] C. De Rango, G. Tsoucaris, and C. Zelwer, "Contribution à l'étude de la structure cristalline de LaAlO_3 ," *Acta Crystallographica*, vol. 20, no. 4, pp. 590–592, 1966.

- [61] X. Liu, Y. Cao, B. Pal, S. Middey, M. Kareev, Y. Choi, P. Shafer, D. Haskel, E. Arenholz, and J. Chakhalian, "Synthesis and electronic properties of Ruddlesden-Popper strontium iridate epitaxial thin films stabilized by control of growth kinetics," *Physical Review Materials*, vol. 1, p. 075 004, 2017.
- [62] K. Jacob, T. Okabe, T. Uda, and Y. Waseda, "Phase relations in the system Sr-Ir-O and thermodynamic measurements on SrIrO₃, Sr₂IrO₄ and Sr₄IrO₆ using solid-state cells with buffer electrodes," *Journal of Alloys and Compounds*, vol. 288, no. 1, pp. 188–196, 1999.
- [63] A. Gutiérrez-Llorente, L. Iglesias, B. Rodríguez-González, and F. Rivadulla, "Epitaxial stabilization of pulsed laser deposited Sr_{n+1}Ir_nO_{3n+1} thin films: Entangled effect of growth dynamics and strain," *APL Materials*, vol. 6, no. 9, p. 091 101, 2018.
- [64] T. J. Anderson, S. Ryu, H. Zhou, L. Xie, J. P. Podkaminer, Y. Ma, J. Irwin, X. Q. Pan, M. S. Rzchowski, and C. B. Eom, "Metastable honeycomb SrTiO₃ /SrIrO₃ heterostructures," *Applied Physics Letters*, vol. 108, no. 15, p. 151 604, 2016.
- [65] L. Zhang, H.-Y. Wu, J. Zhou, F.-X. Wu, Y. Chen, S.-H. Yao, S.-T. Zhang, and Y.-F. Chen, "TEM study of SrIrO₃ thin films with various thicknesses grown on (001) SrTiO₃ substrates synthesized by pulsed laser deposition," *Applied Surface Science*, vol. 280, pp. 282–286, 2013.
- [66] J. Pelleg, in *Mechanical Properties of Materials*. Springer Netherlands, 2013.
- [67] Z.-t. Xu, K.-j. Jin, L. Gu, Y.-l. Jin, C. Ge, C. Wang, H.-z. Guo, H.-b. Lu, R.-q. Zhao, and G.-z. Yang, "Evidence for a Crucial Role Played by Oxygen Vacancies in LaMnO₃ Resistive Switching Memories," *Small*, vol. 8, no. 8, pp. 1279–1284, 2012.
- [68] L. Zhang, Q. Liang, Y. Xiong, B. Zhang, L. Gao, H. Li, Y. B. Chen, J. Zhou, S.-T. Zhang, Z.-B. Gu, S.-H. Yao, Z. Wang, Y. Lin, and Y.-F. Chen, "Tunable semimetallic state in compressive-strained SrIrO₃ films revealed by transport behavior," *Physical Review B*, vol. 91, p. 035 110, 2015.
- [69] F.-X Wu, J. Zhou, L. Y. Zhang, Y. B. Chen, S.-T. Zhang, Z.-B. Gu, S.-H. Yao, and Y.-F. Chen, "Metal-insulator transition in SrIrO₃ with strong spin-orbit interaction," *Journal of Physics: Condensed Matter*, vol. 25, p. 125 604, 2013.
- [70] Z. Konstantinović, J. Santiso, L. Balcells, and B. Martínez, "Strain-Driven Self-Assembled Network of Antidots in Complex Oxide Thin Films," *Small*, vol. 5, no. 2, pp. 265–271, 2009.

- [71] Z. Konstantinović, F. Sandiumenge, J. Santiso, L. Balcells, and B. Martínez, "Self-assembled pit arrays as templates for the integration of Au nanocrystals in oxide surfaces," *Nanoscale*, vol. 5, pp. 1001–1008, 2013.
- [72] H. Brune, "Epitaxial Growth of Thin Films," in *Surface and Interface Science*. John Wiley & Sons, Ltd, 2014, pp. 421–492.
- [73] J. H. Gruenewald, J. Nichols, J. Terzic, G. Cao, J. W. Brill, and S. Seo, "Compressive strain-induced metalinsulator transition in orthorhombic SrIrO₃ thin films," *Journal of Materials Science*, vol. 29, no. 21, 24912496, 2014.
- [74] D. J. Groenendijk, N. Manca, G. Mattoni, L. Kootstra, S. Gariglio, Y. Huang, E. van Heumen, and A. D. Caviglia, "Epitaxial growth and thermodynamic stability of SrIrO₃/SrTiO₃ heterostructures," *Applied Physical Letters*, vol. 109, no. 4, p. 041 906, 2016.
- [75] T. Mitsunaga, "X-ray thin-film measurement techniques II. Out-of-plane diffraction measurements," *Rigaku journal*, vol. 25, no. 1, pp. 7–12, 2009.
- [76] "Balanced electron-hole transport in spin-orbit semimetal SrIrO₃ heterostructures, author = Manca, N. and Groenendijk, D. J. and Pallecchi, I. and Autieri, C. and Tang, L. M. K. and Telesio, F. and Mattoni, G. and McCollam, A. and Picozzi, S. and Caviglia, A. D.," *Physical Review B*, vol. 97, p. 081 105, 8 2018.
- [77] R. A. Cowley and E. K. H. Salje, "The phase transition of strontium titanate," *Philosophical Transactions of the Royal Society of London. Series A: Mathematical, Physical and Engineering Sciences*, vol. 354, no. 1720, pp. 2799–2814, 1996.
- [78] L. Cao, E. Sozontov, and J. Zegenhagen, "Cubic to Tetragonal Phase Transition of SrTiO₃ under Epitaxial Stress: An X-Ray Backscattering Study," *physica status solidi (a)*, vol. 181, no. 2, pp. 387–404, 2000.
- [79] G. Shirane and Y. Yamada, "Lattice-Dynamical Study of the 110 K Phase Transition in SrTiO₃," *Physical Review*, vol. 177, pp. 858–863, 1969.
- [80] Q. Guo, S. Farokhipoor, C. Magén, F. Rivadulla, and B. Noheda, "Tunable resistivity exponents in the metallic phase of epitaxial nickelates," *Nature Communications*, vol. 11, p. 2949, 2020.

- [81] N. D. Patel, A. Mukherjee, N. Kaushal, A. Moreo, and E. Dagotto, "Non-Fermi Liquid Behavior and Continuously Tunable Resistivity Exponents in the Anderson-Hubbard Model at Finite Temperature," *Physical Review Letters*, vol. 119, p. 086 601, 2017.
- [82] G. Herranz, V. Laukhin, F. Sánchez, P. Levy, C. Ferrater, M. V. García-Cuenca, M. Varela, and J. Fontcuberta, "Effect of disorder on the temperature dependence of the resistivity of SrRuO₃," *Physical Review B*, vol. 77, p. 165 114, 2008.
- [83] D. J. Groenendijk, C. Autieri, J. Girovsky, M. C. Martinez-Velarte, N. Manca, G. Mattoni, A. M. R. V. L. Monteiro, N. Gauquelin, J. Verbeeck, A. F. Otte, M. Gabay, S. Picozzi, and A. D. Caviglia, "Spin-Orbit Semimetal SrIrO₃ in the Two-Dimensional Limit," *Physical Review Letters*, vol. 119, p. 256 403, 2017.
- [84] D. J. Groenendijk, N. Manca, J. de Bruijkere, A. M. R. V. L. Monteiro, R. Gaudenzi, H. S. J. van der Zant, and A. D. Caviglia, "Anisotropic magnetoresistance in spin-orbit semimetal SrIrO₃," *The European Physical Journal Plus*, vol. 135, p. 627, 2020.
- [85] J. Fujioka, T. Okawa, A. Yamamoto, and Y. Tokura, "Correlated Dirac semimetallic state with unusual positive magnetoresistance in strain-free perovskite SrIrO₃," *Physical Review B*, vol. 95, p. 121 102, 2017.
- [86] A. Stupakov, O. Pacherova, T. Kocourek, M. Jelinek, A. Dejneka, and M. Tyunina, "Negative magnetoresistance in epitaxial films of neodymium nickelate," *Physical Review B*, vol. 99, p. 085 111, 2019.
- [87] J. Matsuno, K. Ihara, S. Yamamura, H. Wadati, K. Ishii, V. V. Shankar, H.-Y. Kee, and H. Takagi, "Engineering a Spin-Orbital Magnetic Insulator by Tailoring Superlattices," *Physical Review Letters*, vol. 114, p. 247 209, 2015.
- [88] J. Singleton, *Band Theory and Electronic Properties of Solids*. OUP Oxford, 2001.
- [89] C. Lu, A. Quindeau, H. Deniz, D. Preziosi, D. Hesse, and M. Alexe, "Crossover of conduction mechanism in Sr₂IrO₄ epitaxial thin films," *Applied Physics Letters*, vol. 105, no. 8, p. 082 407, 2014.
- [90] C. Moreno, C. Munuera, S. Valencia, F. Kronast, X. Obradors, and C. Ocal, "Reversible Resistive Switching and Multilevel Recording in La_{0.7}Sr_{0.3}MnO₃ Thin Films for Low Cost Nonvolatile Memories," *Nano Letters*, vol. 10, no. 10, pp. 3828–3835, 2010.

- [91] B. Meunier, D. Pla, R. Rodriguez-Lamas, M. Boudard, O. Chaix-Pluchery, E. Martinez, N. Chevalier, C. Jiménez, M. Burriel, and O. Renault, "Microscopic Mechanisms of Local Interfacial Resistive Switching in LaMnO_3 ," *ACS Applied Electronic Materials*, vol. 1, no. 5, pp. 675–683, 2019.
- [92] J. Gonzalez-Rosillo, R. Ortega-Hernandez, J. Jareño Cerulla, E. Miranda, J. Suñe, X. Granados, X. Obradors, A. Palau, and T. Puig, "Volume Resistive Switching in metallic perovskite oxides driven by the Metal-Insulator Transition," *Journal of Electroceramics*, vol. 39, 185196, 2017.
- [93] M. Lanza, "A Review on Resistive Switching in High-k Dielectrics: A Nanoscale Point of View Using Conductive Atomic Force Microscope," *Materials*, vol. 7, 21552182, 2014.
- [94] M. Lanza, U. Celano, and F. Miao, "Nanoscale characterization of resistive switching using advanced conductive atomic force microscopy based setups," *Journal of Electroceramics*, vol. 39, pp. 94–108, 2017.
- [95] S. Brivio, J. Frascaroli, and M. H. Lee, "Electrical AFM for the Analysis of Resistive Switching," in *Electrical Atomic Force Microscopy for Nanoelectronics*. Springer, 2019, pp. 205–229.
- [96] M. Afifi, M. Abdel-Aziz, H. Labib, M Fadel, and E. El-Metwally, "Electrical and switching properties of amorphous films based on the Ge-Se-Tl system," *Vacuum*, vol. 61, no. 1, pp. 45–53, 2001.
- [97] M. Lin, M. Wu, C. Lin, and T. Tseng, "Effects of Vanadium Doping on Resistive Switching Characteristics and Mechanisms of SrZrO_3 -Based Memory Films," *IEEE Transactions on Electron Devices*, vol. 57, no. 8, pp. 1801–1808, 2010.
- [98] M. H. Lee, S. J. Song, K. M. Kim, G. H. Kim, J. Y. Seok, J. H. Yoon, and C. S. Hwang, "Scanning probe based observation of bipolar resistive switching NiO films," *Applied Physics Letters*, vol. 97, no. 6, p. 062909, 2010.
- [99] Y. Du, A. Kumar, H. Pan, K. Zeng, S. Wang, P. Yang, and A. T. S. Wee, "The resistive switching in TiO_2 films studied by conductive atomic force microscopy and Kelvin probe force microscopy," *AIP Advances*, vol. 3, no. 8, p. 082107, 2013.
- [100] H. S. Lee, S. G. Choi, H.-H. Park, and M. J. Rozenberg, "A new route to the Mott-Hubbard metal-insulator transition: Strong correlations effects in $\text{Pr}_{0.7}\text{Ca}_{0.3}\text{MnO}_3$," *Scientific Reports*, vol. 3, p. 1704, 2013.

- [101] Y. Chen, Y.-M. Lu, and H.-Y. Kee, "Topological crystalline metal in orthorhombic perovskite iridates," *Nature Communications*, vol. 1, p. 6593, 2015.
- [102] Z. T. Liu, M. Y. Li, Q. F. Li, J. S. Liu, W. Li, H. F. Yang, C. C. Yao Q. Fan, Z. Wan X. G. Wang, and D. W. Shen, "Direct observation of the Dirac nodes lifting in semimetallic perovskite SrIrO₃ thin films," *Scientific Reports*, vol. 6, p. 30309, 2016.
- [103] D. M. Mattox, "Physical Sputtering and Sputter Deposition (Sputtering)," in *Handbook of Physical Vapor Deposition (PVD)*, William Andrew Publishing, 2010.
- [104] M. Ohring, "Plasma and Ion Beam Processing of Thin Films," in *Materials Science of Thin Films*. Academic Press, 2002.
- [105] S. M. Rossnagel, "Glow discharge plasmas and sources for etching and deposition," in *Thin Film Processes*, Academic Press, 1991, pp. 11–77.
- [106] J. S. Logan, "R.F. diode sputtering," *Thin Solid Films*, vol. 188, no. 2, pp. 307–321, 1990.
- [107] P. R. Willmott and J. R. Huber, "Pulsed laser vaporization and deposition," *Reviews of Modern Physics*, vol. 72, pp. 315–328, 2000.
- [108] I. W. Boyd, "Thin film growth by pulsed laser deposition," *Ceramics International*, vol. 22, no. 5, pp. 429–434, 1996.
- [109] K. Inaba, "X-Ray thin-film measurement techniques I. Overview," *Rigaku journal*, vol. 24, no. 1, pp. 10–15, 2008.
- [110] S. Kobayashi, "X-Ray Thin-Film Measurement Techniques IV. In-Plane Diffraction Measurements," *Rigaku journal*, vol. 26, no. 1, pp. 3–11, 2010.
- [111] M. Birkholz, "Texture and Preferred Orientation," in *Thin Film Analysis by X-Ray Scattering*. John Wiley & Sons, Ltd, 2006, pp. 183–237.
- [112] B. Jones and M. Zimmermann, "High Resolution X-ray Diffractometry 2: Reciprocal Space Mapping," in *Bruker webinars*, ser. Good Diffraction Practice Webinar Series, 2012.
- [113] M. Yasaka, "X-ray thin-film measurement techniques V.X-ray reflectivity measurement," *Rigaku journal*, vol. 26, no. 2, pp. 1–9, 2010.
- [114] J. Moulder, J. Chastain, and R. King, *Handbook of X-ray Photoelectron Spectroscopy: A Reference Book of Standard Spectra for Identification and Interpretation of XPS Data*. Physical Electronics, 1995.

- [115] G. Greczynski and L. Hultman, "X-ray photoelectron spectroscopy: Towards reliable binding energy referencing," *Progress in Materials Science*, vol. 107, p. 100 591, 2020.
- [116] V. L. Mironov, *Fundamentals of scanning probe microscopy*. NT-MDT, 2004.
- [117] B. Voigtländer, "Intermittent Contact Mode/Tapping Mode," in *Scanning Probe Microscopy*, Springer, 2015, pp. 205–221.
- [118] Asylum, "MFP-3D Manual," Oxford Instruments, Tech. Rep., 2008.
- [119] A. S. Morris, "Measurement and Instrumentation Principles," *Measurement Science and Technology*, vol. 12, no. 10, pp. 1743–1744, 2001.
- [120] JPK, "Nanowizard AFM Handbook," JPK Instruments, Tech. Rep., 2012.
- [121] H. O. Jacobs, H. F. Knapp, and A. Stemmer, "Practical aspects of Kelvin probe force microscopy," *Review of Scientific Instruments*, vol. 70, no. 3, pp. 1756–1760, 1999.
- [122] T. Machleidt, E. Sparrer, D. Kapusi, and K.-H. Franke, "Deconvolution of Kelvin probe force microscopy measurements: methodology and application," *Measurement Science and Technology*, vol. 20, no. 8, p. 084 017, 2009.
- [123] W. Melitz, J. Shen, A. C. Kummel, and S. Lee, "Kelvin probe force microscopy and its application," *Surface Science Reports*, vol. 66, no. 1, pp. 1–27, 2011.
- [124] K. Vernon-Parry, "Scanning electron microscopy: an introduction," *III-Vs Review*, vol. 13, no. 4, pp. 40–44, 2000.
- [125] J. Goldstein, *Practical Scanning Electron Microscopy: Electron and Ion Microprobe Analysis*. Springer, 2012.
- [126] D. B. Williams and C. B. Carter, "The Transmission Electron Microscope," in *Transmission Electron Microscopy*, Springer, 2009, pp. 3–22.
- [127] D. B. Williams and C. B. Carter, "Specimen Preparation," in *Transmission Electron Microscopy*, Springer, 2009, pp. 173–193.
- [128] J. T. M. Stevenson and A. M. Gundlach, "The application of photolithography to the fabrication of microcircuits," *Journal of Physics E: Scientific Instruments*, vol. 19, no. 9, pp. 654–667, 1986.
- [129] J. Nickel, *Magnetoresistance Overview*, ser. HP Laboratories technical report. Hewlett-Packard Laboratories, 1995.

List of Publications

The publications related to the content presented in this thesis are:

- V. Fuentes, B. Vasić, Z. Konstantinović, B. Martínez, L. Balcells and A. Pomar "Resistive Switching in semimetallic SrIrO₃ thin films." *ACS Applied Electronic Materials* vol. 1, no. 9, pp. 1981-1988, 2019
- V. Fuentes, B. Vasić, Z. Konstantinović, B. Martínez, L. Balcells, A. Pomar, "Resistive switching in Strontium iridate based thin films." *Journal of Magnetism and Magnetic Materials*, vol. 501, 2020

Moreover, in the course of the thesis, additional articles of other topics were also published:

- L. Balcells, I. Stanković, Z. Konstantinović, A. Alagh, V. Fuentes, L. López-Mir, Laura and J. Oró, N. Mestres, C. García, A. Pomar and B. Martínez. "Spontaneous in-flight assembly of magnetic nanoparticles into macroscopic chains", *Nanoscale*, vol. 11, pp 14194-14202, 2019
- B. Colson, V. Fuentes, Z. Konstantinović, D. Colson, A. Forget, N. Lazarević, M. Šćepanović, Z.V. Popović, C. Frontera, L. Balcells, B. Martinez and A. Pomar. "Self-assembled line network in BiFeO₃ thin films" *Journal of Magnetism and Magnetic Materials*, vol. 509, 2020